

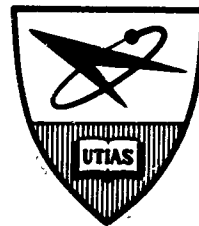
INSTITUTE  
FOR  
AEROSPACE STUDIES

UNIVERSITY OF TORONTO

AN EXPERIMENTAL DETERMINATION OF THE GLADSTONE-DALE CONSTANTS  
FOR DISSOCIATING OXYGEN

by

J. H. B. Anderson



D D C  
RECEIVED  
APR 18 1967  
RECORDED  
C

MARCH 1967

ARCHIVE COPY

UTIAS TECHNICAL NOTE NO. 105  
AFOSR 67-0336

AD650162

AN EXPERIMENTAL DETERMINATION OF THE GLADSTONE-DALE CONSTANTS  
FOR DISSOCIATING OXYGEN

by  
J. H. B. Anderson

Manuscript received June 1966

MARCH 1967

UTIAS TECHNICAL NOTE NO. 105  
AFOSR 67-0336

#### ACKNOWLEDGEMENT

I wish to thank Dr. G. N. Patterson, Director of the Institute, for the opportunity to work and study at UTIAS.

I also wish to thank Dr. I. I. Glass, who supervised this research, for his encouragement and interest in this work.

Thanks are due to Mr. J.E. Drewry and Dr. A.G. Boyer for helpful suggestions and assistance with the operation of the 4" x 7" shock tube. The assistance of Dr. L. Bernstein of Queen Mary College, London, of Dr. E. A. Brown of the Boeing Company, Seattle, and of Mr. R.F. Flagg, formerly of Avco Rad and now at the Institute, in obtaining the required normal shock data is greatly appreciated. Thanks are due also to Dr. J. H. de Leeuw and Dr. R. M. Measures, of the Institute staff, for the loan of the Kerr Cell equipment and several components which went into the exploding wire light source.

Special thanks are due to Dr. A. Levy for many fruitful discussions, and for his help in solving many of the problems which cropped up in the course of the experimental work.

The assistance and careful work of the technicians and the shop staff is appreciated.

The generous assistance of Agfa-Gevaert, West Germany; Eastman Kodak, Rochester, U.S.A.; and Ilford Ltd., London, England, in providing high-speed photographic material, is gratefully acknowledged.

The financial assistance received from the Air Force Office of Scientific Research under Grant No. AF-AFOSR-365-66 and the Canadian Defence Research Board and the National Research Council is acknowledged with thanks.

### SUMMARY

An experimental determination of the Gladstone-Dale constants for dissociating oxygen has been carried out. The result obtained for the specific refractivity of the oxygen molecule was in good agreement with available room-temperature data, indicating that the Gladstone-Dale constants do not appear to change with temperature. The result obtained for the specific refractivity of the oxygen atom was in agreement with the work of Alpher and White (Ref. 7) but the present work was considered to be more reliable in view of a much lower experimental error, and the removal of the assumption of a value for the Gladstone-Dale constant for the oxygen molecule.

A theoretical analysis was also carried out in which expressions for the index of refraction of dissociating and ionizing gases were derived. These results were used in an analysis of the formation of monochromatic and white-light interference patterns in a Mach-Zehnder interferometer.

An appendix is included giving a brief summary of as yet uncompleted experimental work to determine the Gladstone-Dale constants for ionizing argon. Another appendix gives details of an exploding wire light source, which was developed to allow the use of a Kerr cell unit to improve the time resolution of the interferograms.

## TABLE OF CONTENTS

	<u>Page</u>
NOTATION	v
1. INTRODUCTION	1
2. THEORETICAL CONSIDERATIONS	1
2.1 Index of Refraction	1
2.1.1 Introduction	1
2.1.2 Polarizability	2
2.1.3 The Telegraph Equation	3
2.1.4 Determination of the Conduction Currents	7
2.1.5 Index of Refraction and the Gladstone-Dale Constant	10
2.2 Application to Interferometry	12
2.2.1 Introduction	12
2.2.2 The Mach-Zehnder Interferometer	13
2.2.3 The Parallel Fringe Method	16
2.2.4 White Light Interference	18
3. EXPERIMENTAL RESULTS FOR OXYGEN	22
3.1 Procedure and method of Analysis	22
3.2 Experimental Results and Error Analysis	26
4. CONCLUSIONS	30
REFERENCES	31
TABLES	
FIGURES	
APPENDIX A - Calculation of White-Light Interference Patterns	
APPENDIX B - A Summary of the Experimental Work Done to Date (March 1966) on the Determination of the Gladstone-Dale Constants for Argon	
APPENDIX C - An Exploding Wire Light Source for the UTIAS 9-in. Mach-Zehnder Interferometer	

### NOTATION

$A$	amplitude of a light wave
$A_a, A_t$	constants in the Cauchy equation for index of refraction
$\vec{B}$	magnetic induction
$B_a, B_t$	constants in the Cauchy equation
$C_a, C_t$	constants in the Cauchy equation
$\vec{D}$	electric displacement
$\vec{E}$	electric field intensity
$\vec{H}$	magnetic field strength
$I$	instantaneous light intensity
$\bar{I}$	time-averaged light intensity
$K$	Gladstone-Dale constant
$K_1, K_2, \text{etc.}$	constants in the dispersion relation for the Gladstone-Dale constant
$L$	geometric width of the shock tube section
$\vec{M}$	magnetization of the medium
$N$	number density; particles per unit volume
$\vec{P}$	polarization per unit volume
$T$	temperature
$V$	volume (see Eq.6)
$X_1, X_2, X_3$	constants defined in Sec. 2.2.4
$c$	speed of light in vacuum
$d$	spacing of individual fringes
$e$	electronic charge
$i = \sqrt{-1}$	
$\vec{j}$	current density
$k^*$	complex propagation constant
$k$	real propagation constant

$k_e$	dielectric constant
$k_m$	magnetic susceptibility
$m$	particle mass
$n$	index of refraction
$n_p$	phase index of refraction
$n_g$	group index of refraction
$\vec{p}$	induced dipole moment per particle
$p_1$	initial pressure in the shock tube
$q$	charge density
$t$	time
$\vec{u}$	particle velocity (microscopic)
$\vec{v}$	flow velocity (macroscopic)
$x$	degree of ionization
$x, y, z$	space coordinates
$\alpha$	degree of dissociation polarizability
$\beta$	attenuation constant
$\gamma$	quantity defined in Appendix A (see Fig. 9b)
$\Delta$	transformed frequency
$\Delta_0, \Delta_1$ , etc	constants in transformed dispersion relation for the Gladstone-Dale constants
$\Delta'_0, \Delta'_1$ , etc	constants in the transformed Cauchy equation
$\delta$	percent error
$\epsilon$	angle of rotation of mirror 2 in interferometer (see Sec. 2.2.3)
$\epsilon_0$	permeability of free space
$\lambda$	wavelength
$\lambda_0$	wavelength in vacuum
$\mu_0$	magnetic permeability of free space
$\nu$	frequency

$\rho$	density
$\sigma$	conductivity
$\epsilon$	electric susceptibility
$\chi_m$	magnetic susceptibility
$\omega$	angular frequency

Subscripts:

1	initial conditions in test section of shock tube
2	final conditions in test section of shock tube
a	medium in which interferometer is immersed

## 1. INTRODUCTION

For the past few years, one of the continuing projects being undertaken on the UTIAS 4 in. x 7 in. Hypersonic Shock Tube has been the study of non-equilibrium corner expansion flows of dissociating and ionizing gases. The major diagnostic tool in this study has been optical interferometry, using the UTIAS 9 in. Mach-Zehnder interferometer, since such an instrument does not disturb the flow under observation. However, in order to use this method, detailed knowledge was required of the index of refraction of the gas under study and especially the relation of the index of refraction to the density, i.e., the specific refractivity, or the Gladstone-Dale constant. Experimental measurements of these quantities at the high temperatures used in the expansion studies appear to have been made in only one instance (Ref. 7). Hence the desirability of measuring the specific refractivities to check the results of Ref. 7. Also, since the expansion work involved a large range of gas temperatures, it was desired to investigate the temperature dependence, if any, of the Gladstone-Dale constants.

The gases which are being used in the expansion studies are dissociating oxygen and ionizing argon, and the theoretical part of this Technical Note is applicable to both gases. However, the experimental work reported here concerns the measurement of the Gladstone-Dale constants for dissociating oxygen only. A short summary of the work done to date on the argon case is given in Appendix B. This case will be treated separately in another UTIAS report, when the work is completed.

## 2. THEORETICAL CONSIDERATIONS

In this section, expressions for the index of refraction of dissociating and ionizing gases are derived from Maxwell's equations and from the equations of motion of a plasma. A short discussion of polarizability is included showing how the index of refraction of a neutral gas arises. The Gladstone-Dale constant is introduced and its relation to the polarizability of the gas is shown. A short discussion is given on how the polarizability and the Gladstone-Dale constant can be expected to vary with temperature.

These results are then applied to interferometry and expressions are derived giving the intensity distribution of monochromatic and white-light interference patterns.

### 2.1 Index of Refraction

#### 2.1.1 Introduction

It is well known that a light wave consists of coupled electric and magnetic fields which oscillate in mutually perpendicular directions and perpendicular to the direction of propagation. In general, the electric and magnetic fields can be represented by (Refs. 9, 10):

$$\begin{aligned}\vec{E} &= \vec{E}_0 \exp [i(kz - \omega t)] \\ \vec{B} &= \vec{B}_0 \exp [i(kz - \omega t)]\end{aligned}\tag{1}$$

where distance  $z$  is measured in the direction of propagation of the wave,  $\omega$  is the angular frequency, and  $k^*$  is the complex propagation constant, where:

$$k^* = k + i\beta \quad (2)$$

where  $k$  is the real propagation constant, defined as  $2\pi/\lambda$  ( $\lambda$  is the wavelength) and  $\beta$  is the attenuation constant. It will be shown (Sec. 2.1.3) that  $\beta$  is related to the conductivity  $\sigma$  of the medium and equals zero when  $\sigma = 0$ . Thus the electric and magnetic fields could also be given by:

$$\begin{aligned} \vec{E} &= \vec{E}_0 \exp[-\beta z] \exp[i(kz - \omega t)] \\ \vec{B} &= \vec{B}_0 \exp[-\beta z] \exp[i(kz - \omega t)] \end{aligned} \quad (3)$$

which shows the true significance of the attenuation constant.

The phase velocity,  $v_p$ , of a wave comprised of only one frequency is defined as the velocity of a point of constant phase on the wave, i.e.:

$$kz - \omega t = \text{a constant}$$

Hence:

$$k \frac{dz}{dt} = \omega$$

or:

$$\frac{dz}{dt} = v_p = \frac{\omega}{k} = \frac{2\pi\nu}{\frac{2\pi}{\lambda}} = \lambda\nu \quad (4)$$

where  $\nu$  is the frequency of the wave. In a vacuum:

$$v_p = c = 2.9979 \times 10^8 \text{ m/sec.}$$

where  $c$  is the velocity of light in a vacuum, a constant under all conditions. In a medium other than vacuum we define:

$$v_p = \frac{c}{n_p} \quad (5)$$

where  $n_p$  is the phase index of refraction, a number greater than one in most cases..

### 2.1.2 Polarizability

(It will be shown later (Sec. 2.1.4) that the interaction between the medium and the magnetic field associated with a light wave is negligible. Therefore, in all that follows, we consider only the interaction between the medium and the electric field associated with the light wave.)

If the medium through which a light wave is passing is composed of electrically neutral "hard sphere" particles, one would expect that the medium would have no effect on the light wave (except for attenuation), since there would then be no way in which the medium and the light wave could interact. This, however, is not the case. An atom, for example, is

composed of a positive nucleus surrounded by a cloud of negative electrons. If there is no electric field present, the centres of charge of the nucleus and the electron cloud coincide. If an electric field is present, the electron cloud may be displaced slightly with respect to the nucleus, since, if the electrons are attracted, the nucleus is repelled, and vice-versa. This relative motion of the electrons and nucleus constitutes an electric current which is present as long as the electric field is changing. The steady-state result, when the electric field is constant, is a dipole.

The same considerations apply to molecules. Non-polar molecules behave qualitatively like atoms, as described above. Polar molecules have built-in dipole moments, and the effect of the electric field is to rotate the molecule as well as to distort it. This rotation also produces a component of relative motion of the centres of positive and negative charge in the direction of the electric field, again constituting an electric current.

In general, a medium composed of electrically neutral particles in the presence of an electric field  $\vec{E}$  will develop a polarization field  $\vec{P}$ , where  $\vec{P}$  is defined as the induced dipole moment per unit volume.  $\vec{P}$  may be considered parallel and directly proportional to  $\vec{E}$ , an excellent approximation for the electric field associated with a light wave, and for a gas, where the interactions between particles are completely random, and where there are no preferred directions such as might exist in a crystal. We may then write:

$$\vec{P} = \frac{1}{V} \sum_i \vec{p}_i = N \alpha \vec{E} \quad (6)$$

where  $\vec{p}_i$  is the dipole moment induced in each particle, the polarizability,  $\alpha$ , is the proportionality factor between  $\vec{P}$  and  $\vec{E}$ , and  $N$  is the number density of particles. If a number of different species of particles are present, provided there are no inter-particle forces (for example, a dilute gas of electrically neutral particles) we may write:

$$\vec{P} = \sum_i N_i \alpha_i \vec{E} \quad (7)$$

where  $N_i$  and  $\alpha_i$  are the number density and polarizability respectively of the  $i$ th species.

So far, only neutral particles have been considered. In the case of charged particles, such as electrons and ions, there is of course a direct coulomb interaction between the particles and the electric field associated with the light wave. This will be considered separately (Sec. 2.1.4).

### 2.1.3 The Telegraph Equation

The relations between the refractive index, the dielectric constant, and the conductivity can be derived from the telegraph equation, which is in turn derived from Maxwell's equations. The telegraph equation is used here rather than the more usual wave equation because the conductivity of the medium must be retained in the analysis. A number of quantities must now be defined (in rationalized MKS units):

Let:

$$\vec{D} = \epsilon_0 \vec{E} + \vec{P},$$

where  $\vec{D}$  is defined as the electric displacement, and  $\epsilon_0$  is defined as the permittivity of free space, where

$$\epsilon_0 = 8.854 \times 10^{-12} \text{ farads/meter}$$

If the medium is linear and isotropic (i.e.,  $\vec{P}$  parallel to and proportional to  $\vec{E}$ ) we may write:

$$\vec{D} = \epsilon_0 (1 + \chi_e) \vec{E}$$

where  $\chi_e$  is the electric susceptibility. We may then let:

$$k_e = (1 + \chi_e)$$

where  $k_e$  is defined as the dielectric constant. It is then noted that:

$$\alpha = \epsilon_0 \chi_e,$$

where  $\alpha$  is defined as the polarizability, as mentioned above.

$$\vec{B} = \mu_0 (\vec{H} + \vec{M}),$$

where  $\vec{B}$  is defined, strictly, as the magnetic induction, and  $\vec{H}$  is defined as the magnetic field.  $\vec{M}$  is defined as the magnetic dipole moment per unit volume, or the magnetization. In this development,  $\vec{M}$  will be set equal to zero, since we are dealing with a gaseous medium where the magnetization is negligible.  $\mu_0$  is defined as the magnetic permeability of free space, where:

$$\mu_0 = 4\pi \times 10^{-7} \text{ henrys/meter.}$$

Generally, for non-ferromagnetic media, we may write:

$$\vec{B} = \mu_0 (1 + \chi_m) \vec{H}$$

where  $\chi_m$  is defined as the magnetic susceptibility. We may then write:

$$k_m = (1 + \chi_m)$$

where  $k_m$  is defined as the relative permeability. It is noted that the assumption of  $\vec{M} = 0$  is equivalent to putting  $k_m = 1$ .

It is noted that  $\vec{M}$  is analogous to  $\vec{P}$ , and that  $k_m$  is analogous to  $k_e$ . It is also noted that since  $k_m = 1$ ,  $\vec{B}$  and  $\vec{H}$  can be, and often are, both loosely referred to as the magnetic field, since they differ by only a constant factor.

We can now proceed to derive and solve the telegraph equation. Maxwell's equations are, in stationary form (Refs. 9, and 10)

$$\nabla \cdot \vec{D} = q_{\text{true}} \quad (8)$$

$$\nabla \cdot \vec{B} = 0 \quad (9)$$

$$\nabla \times \vec{E} = \frac{\partial \vec{B}}{\partial t} \quad (10)$$

$$\left. \begin{aligned} \nabla \times \vec{H} &= \vec{j}_{\text{true}} + \frac{\partial \vec{D}}{\partial t} \\ &= \vec{j}_{\text{true}} + \frac{\partial \vec{P}}{\partial t} + \epsilon_0 \frac{\partial \vec{E}}{\partial t} \\ &= \vec{j}_{\text{true}} + \epsilon_0 k_e \frac{\partial \vec{E}}{\partial t} \end{aligned} \right\} \quad (11)$$

where  $q_{\text{true}}$  is the true density of charge and  $\vec{j}_{\text{true}}$  is the true conduction current.

In general, if the medium is moving at velocity  $\vec{v}$ , a term must be added to the right side of Eq. 11 to account for the convection current, a term of the form:

$$\vec{v} (q_{\text{true}} - \nabla \cdot \vec{P})$$

This term takes this form because, in addition to the actual charge present, there is a charge due to the spatial variation of the polarization, given by:

$$\nabla \cdot \vec{P} = -q_p$$

We must also add terms to correct the polarization current in Eq. 11 for the motion of the medium. The total polarization current may then be written (Ref. 4):

$$\frac{D\vec{P}}{Dt} = \frac{\partial \vec{P}}{\partial t} + \nabla \times (\vec{P} \times \vec{v}) + \vec{v} (\nabla \cdot \vec{P})$$

The differential operator used here is a general one, and can be applied to any vector quantity in a moving medium. (See for example, Ref. 9 in connection with Faraday's Law). The last term on the right represents the current due to the spatial change in the polarization in the volume under observation. The middle term on the right represents the polarization current in the volume under consideration due to perturbations in the velocity,  $\vec{v}$ .

In general, however, the spatial derivatives are small enough that the velocity would have to be very high before the terms added to account for the moving medium become comparable to the explicit time derivatives. In addition,  $q_{\text{true}}$  is set equal to zero, i.e., there is no net charge. Thus all the additional terms involving the velocity may be neglected.

It is noted that, strictly speaking, the polarization field  $\vec{P}$  and the true current  $\vec{j}_{\text{true}}$  have components due to the interaction of the moving medium and the magnetic field associated with the light wave. How-

ever, these terms can be neglected also, as much smaller than the corresponding terms due to the electric field. (see Sec. 2.1.4).

The telegraph equation may now be derived. Noting that, as defined earlier:

$$\vec{B} = \mu_0 k_m \vec{H}$$

where  $k_m$  is set equal to one, and that Ohm's Law states that:

$$\vec{J}_{\text{true}} = \sigma \vec{E}$$

then, taking the curl of Eq. 10 and substituting from Eq. 11, we have:

$$\begin{aligned} \nabla \times (\nabla \times \vec{E}) &= \nabla \times \left( - \frac{\partial \vec{B}}{\partial t} \right) \\ &= - \frac{\partial}{\partial t} (\mu_0 \nabla \times \vec{H}) \\ &= - \mu_0 \frac{\partial}{\partial t} \left( \vec{J}_{\text{true}} + \epsilon_0 k_e \frac{\partial \vec{E}}{\partial t} \right) \\ &= - \mu_0 \frac{\partial}{\partial t} \left( \sigma \vec{E} + \epsilon_0 k_e \frac{\partial \vec{E}}{\partial t} \right) \\ &= - \mu_0 \sigma \frac{\partial \vec{E}}{\partial t} - \mu_0 \epsilon_0 k_e \frac{\partial^2 \vec{E}}{\partial t^2} \end{aligned}$$

But:

$$\nabla \times (\nabla \times \vec{E}) = \nabla (\nabla \cdot \vec{E}) - \nabla^2 \vec{E}$$

However, the charge density  $q_{\text{true}}$  has been set equal to zero, and  $\nabla \cdot \vec{E}$  is negligible in relation to the time derivatives, so that  $\nabla \cdot \vec{E}$  may be neglected, since:

$$\nabla \cdot \vec{E} = q_{\text{true}} - \nabla \cdot \vec{P}$$

Hence, when reduced to one dimension, we have:

$$\frac{\partial^2 \vec{E}}{\partial z^2} - \mu_0 \sigma \frac{\partial \vec{E}}{\partial t} - \mu_0 \epsilon_0 k_e \frac{\partial^2 \vec{E}}{\partial t^2} = 0 \quad (12)$$

which is the telegraph equation. It can be shown, that (Ref. 10)

$$\mu_0 \epsilon_0 = \frac{1}{c^2}$$

so that Eq. 12 becomes:

$$\frac{\partial^2 \vec{E}}{\partial z^2} - \mu_0 \sigma \frac{\partial \vec{E}}{\partial t} - \frac{k_e}{c^2} \frac{\partial^2 \vec{E}}{\partial t^2} = 0 \quad (13)$$

Noting that Eq. 1 is a solution of Eq. 13, we can substitute and obtain;

$$-(k^*)^2 + \frac{i \omega \sigma}{\epsilon_0 c^2} + \frac{\omega^2 k_e}{c^2} = 0 \quad (14)$$

We can then substitute for  $(k^*)^2$  from Eq. 2, separate into real and imaginary parts, and solve the resulting simultaneous equations for  $\beta$  and  $k$ . The roots are:

$$\beta^2 = -\frac{1}{2} \frac{\omega^2}{c^2} k_e + \frac{1}{2} \frac{\omega}{c} \sqrt{\frac{\omega^2}{c^2} k_e^2 + \frac{\sigma^2}{c^2 \epsilon_0^2}} \quad (15)$$

$$k^2 = +\frac{1}{2} \frac{\omega^2}{c^2} k_e + \frac{1}{2} \frac{\omega}{c} \sqrt{\frac{\omega^2}{c^2} k_e^2 + \frac{\sigma^2}{c^2 \epsilon_0^2}} \quad (16)$$

As we noted earlier,  $\beta = 0$  when  $\sigma = 0$

We also noted earlier that:

$$v_p = \frac{\omega}{k}$$

and that:

$$n_p = \frac{c}{v_p} = \frac{c k}{\omega}$$

so that:

$$n_p^2 = \frac{c^2 k^2}{\omega^2}$$

Substituting from Eq. 16, we find that:

$$n_p^2 = \frac{1}{2} k_e + \frac{1}{2} \sqrt{k_e^2 + \frac{\sigma^2}{\omega^2 \epsilon_0^2}} \quad (17)$$

#### 2.1.4 Determination of the Conduction Currents

The determination of the conduction currents due to charged particles, which we neglected earlier (Sec. 2.1.2), may be done through the equations of motion for electrons and ions. For electrons, we may write (Ref. 4):

$$N_e e(\vec{E} + \vec{v} \times \vec{B}) + N_e e(\vec{u} \times \vec{B}) - N_e m_e \nu_c \vec{u} = N_e m_e \frac{d\vec{u}}{dt} \quad (18)$$

where  $N_e$  is the number density of electrons,  $e$  is the electronic charge,  $\vec{v}$  is the velocity of the gas as a whole,  $\vec{u}$  is the velocity of individual electrons,  $m_e$  is the mass of the electron, and  $\nu_c$  is the collision frequency for an electron.

We must now show that the forces due to the magnetic field associated with the light wave may be neglected, i.e., that terms containing  $(\vec{v} \times \vec{B})$  and  $(\vec{u} \times \vec{B})$  may be dropped. We have from Eq. 10:

$$\nabla \times \vec{E} = - \frac{\partial \vec{B}}{\partial t}$$

Substituting from Eq. 1, and assuming that the light wave is a plane wave, so that all space derivatives vanish except  $\partial/\partial z$ , this equation becomes (performing the differentiation)

$$(x \text{ component}) \quad -i k^* E_y = i \omega B_x$$

$$(y \text{ component}) \quad i k^* E_x = i \omega B_y$$

so that:

$$\left| \frac{E_y}{B_x} \right| = \left| \frac{E_x}{B_y} \right| = \frac{\omega}{k^*} = v_p$$

taking the real part only. Hence, going back to Eq. 18, the ratio of the forces due to the electric and magnetic fields may be written (for  $\vec{u}$  perpendicular to  $\vec{B}$ ):

$$\frac{eE}{euB} = \frac{e v_p B}{euB} = \frac{v_p}{u} \gg 1 \quad (19)$$

Hence, the terms giving forces due to the magnetic field may be neglected.

Therefore, Eq. 18 may be rewritten:

$$N_e e \vec{E} - N_e m_e v_c \vec{u} = N_e m_e \frac{d\vec{u}}{dt} \quad (20)$$

If we now let the electric field vary as described by Eq. 1, and assume that the velocity of the charged particles is proportional to the applied electric field, Eq. 20 becomes:

$$e \vec{E} - m_e v_c \vec{u} = -i \omega m_e \vec{u}$$

and

$$\vec{u} = \vec{u}_e = - \frac{\frac{e}{m_e} \vec{E}}{i \omega - v_c} = \frac{\frac{e}{m_e} \vec{E} (v_c + i \omega)}{v_c^2 + \omega^2} = \frac{e}{m_e (v_c^2 + \omega^2)} \left( v_c \vec{E} - \frac{\partial \vec{E}}{\partial t} \right) \quad (21)$$

An equation similar to Eq. 20 can also be written for each species of ion present in the medium, and the result is given by, as in Eq. 21:

$$\vec{u}_{ion} = \frac{e}{m_{ion} [(v'_c)^2 + \omega^2]} \left( v'_c \vec{E} - \frac{\partial \vec{E}}{\partial t} \right) \quad (22)$$

where  $v'_c$ , the collision frequency for ions, will generally be different from  $v_c$ .

We can now write down expressions for all the currents that appear on the right side of Eq. 11. The conduction current due to the motion of the electrons is given by:

$$\begin{aligned}\vec{J}_e &= N_e e \vec{u}_e \\ &= \frac{N_e e^2}{m_e (\nu_c^2 + \omega^2)} \left( \nu_c \vec{E} - \frac{\partial \vec{E}}{\partial t} \right) \quad (23)\end{aligned}$$

Similarly, the ion current is given by:

$$\begin{aligned}\vec{J}_{ion} &= N_{ion} e \vec{u}_{ion} \\ &= \frac{N_{ion} e^2}{m_{ion} [(\nu'_c)^2 + \omega^2]} \left( \nu'_c \vec{E} - \frac{\partial \vec{E}}{\partial t} \right) \quad (24)\end{aligned}$$

As noted in Sec. 2.1.2, a change in polarization,  $\vec{P}$ , of the medium gives rise to a current. Hence, for the ions, we have:

$$\begin{aligned}\vec{J}_{P_{ion}} &= \frac{\partial \vec{P}_{ion}}{\partial t} \\ &= \alpha_{ion} N_{ion} \frac{\partial \vec{E}}{\partial t} \quad (25)\end{aligned}$$

and similarly for the neutral species present:

$$\begin{aligned}\vec{J}_{P_n} &= \frac{\partial \vec{P}_n}{\partial t} \\ &= \alpha_n N_n \frac{\partial \vec{E}}{\partial t} \quad (26)\end{aligned}$$

We can now sum Eqs. 23, 24, 25 and 26, and thus form the quantity that appears on the right side of Eq. 11:

$$\nabla \times \vec{H} = \vec{J}_e + \vec{J}_{ion} + (\vec{J}_{P_{ion}} + \vec{J}_{P_n}) + \epsilon_0 \frac{\partial \vec{E}}{\partial t} \quad (27)$$

However, the ion current may be neglected here as being much smaller than the electron current. Thus, Eq. 27 becomes:

$$\nabla \times \vec{H} = \frac{N_e e^2 \nu_c}{m_e (\nu_c^2 + \omega^2)} \vec{E} + (\alpha_{ion} N_{ion} + \alpha_n N_n - \frac{N_e e^2}{m_e (\nu_c^2 + \omega^2)} + \epsilon_0) \frac{\partial \vec{E}}{\partial t}$$

If we let:

$$\omega_p^2 = \frac{N_e e^2}{\epsilon_0 m_e}$$

where  $\omega_p$  is the plasma frequency, and substitute, we obtain:

$$\nabla \times \vec{H} = \epsilon_0 \left[ \frac{\nu_c \frac{\omega_p^2}{\omega^2}}{\left(1 + \frac{\nu_c^2}{\omega^2}\right)} \right] \vec{E} + \epsilon_0 \left[ 1 + \frac{1}{\epsilon_0} \sum \alpha_i N_i - \frac{\frac{\omega_p^2}{\omega^2}}{1 + \frac{\nu_c^2}{\omega^2}} \right] \frac{\partial \vec{E}}{\partial t} \quad (28)$$

where the contributions to the polarization current have been summed in one term. If we compare Eq. 28 with Eq. 11 written in the form:

$$\nabla \times \vec{H} = \sigma \vec{E} + \epsilon_0 k_e \frac{\partial \vec{E}}{\partial t}$$

then we may put:

$$\sigma = \frac{\epsilon_0 \nu_c \frac{\omega_p^2}{\omega^2}}{\left(1 + \frac{\nu_c^2}{\omega^2}\right)} \quad (29)$$

$$k_e = 1 + \frac{1}{\epsilon_0} \sum \alpha_i N_i - \frac{\frac{\omega_p^2}{\omega^2}}{1 + \frac{\nu_c^2}{\omega^2}} \quad (30)$$

#### 2.1.5 Index of Refraction and the Gladstone-Dale Constant

Earlier it was shown that (Sec. 2.1.3):

$$n_p^2 = \frac{1}{2} k_e + \frac{1}{2} \sqrt{k_e^2 + \frac{\sigma^2}{\omega^2 \epsilon_0^2}} \quad (17)$$

On substituting from Eqs. 29 and 30 for  $\sigma$  and  $k_e$ , and assuming  $\nu_c \ll \omega$ , Eq. 17 becomes, on simplifying:

$$n_p^2 = \left( 1 + \frac{1}{\epsilon_0} \sum \alpha_i N_i - \frac{\omega_p^2}{\omega^2} \right) \quad (31)$$

and then, using the binomial expansion, we obtain to a first but very good approximation:

$$n_p = 1 + \frac{1}{2\epsilon_0} \sum \alpha_i N_i - \frac{1}{2} \frac{\omega_p^2}{\omega^2} \quad (32)$$

The number density may be written as:

$$N_i = \frac{\rho_i}{m_i}$$

so that Eq. 32, becomes:

$$n_p - 1 = \frac{1}{2\epsilon_0} \sum_i \alpha_i \frac{\rho_i}{m_i} - \frac{1}{2} \frac{\omega_p^2}{\omega^2} \quad (33)$$

or:

$$n_p - 1 = \sum_i K_i \rho_i - \frac{1}{2} \frac{\omega_p^2}{\omega^2} \quad (34)$$

Equation 34 is the Gladstone-Dale equation, and:

$$K_i = \frac{1}{2\epsilon_0} \frac{\alpha_i}{m_i} \quad (35)$$

is the Gladstone-Dale constant, or the specific refractivity of the  $i$ th species.

The last term in Eqs. 33 and 34 may be written:

$$\frac{1}{2} \frac{\omega_p^2}{\omega^2} = \frac{N_e e^2}{8\pi^2 v^2 m_e \epsilon_0} = \frac{N_e e^2 \lambda^2}{8\pi^2 c^2 m_e \epsilon_0}$$

which is a function of the number density of electrons and the wavelength. Numerically:

$$\frac{1}{2} \frac{\omega_p^2}{\omega^2} = 4.46 \times 10^{-16} N_e \lambda^2 = 40.08 \frac{N_e}{v^2}$$

where  $N_e$  is in particles per cubic meter,  $\lambda$  is in meters, and  $v$  is in  $\text{sec}^{-1}$ .

It is noted in Eq. 34 that an increase in the densities  $\rho_i$  produces an increase in the index of refraction while an increase in the value of  $\omega_p^2$ , i.e., of the electron number density, produces a decrease in the index of refraction and, if  $\omega_p^2$  is large enough, the index of refraction may become less than one, i.e., the velocity of the light becomes higher than in a vacuum. This, however, does not imply signalling at speeds greater than the speed of light, because, in order to transmit information, the wave must be modulated which immediately introduces other frequencies. The combined wave travels according to the group index of refraction, which will be introduced later, rather than the phase index of refraction.

It is seen from Eq. 35 that the Gladstone-Dale constant for a given species is a function only of the molecular weight and the polarizability. Since the molecular weight can be considered constant for the species in question, it follows that any changes in the value of the Gladstone-Dale constant will enter as variations in the polarizability of the species. Therefore something should be said at this point about the temperature dependence of the polarizability.

It is noted from the discussion of polarization given in Sec. 2.1.2 that the model proposed for atoms and non-polar molecules is electrically symmetrical in all directions when no electric field is present, i.e., its electrical "appearance" is independent of the orientation

taken up by the particle in the course of its random thermal motion. Hence, when an electric field is applied to the medium, the polarization of the particle must be independent of the particle's orientation relative to the applied electric field. The polarization process takes place extremely quickly, and if the impressed field is that of a light wave, then the polarization varies with the frequency of light. Hence, changes in the orientation of the particle will have no effect, since these changes occur at a frequency much lower than that of the impressed electric field. Therefore, if the polarization of the particle is independent of the particle's orientation, and is insensitive to changes in that orientation, then the polarization can be said to be independent of temperature, which is a measure of the (relatively) low frequency at which changes in orientation take place (e.g.,  $10^{10}$  collisions per second, compared to  $10^{15}$  sec $^{-1}$ , the approximate frequency of light).

The case of polar molecules, however, is different. Here, it is recalled, the molecules have built-in dipole moments and the orientation of these dipole moments is thus a function of the thermal motion of the particles, when no electric field is present. When an electric field is applied, it tends to orientate the dipoles in the direction of the field, but this orientation is opposed by the thermal motion of the particles. It is seen that the degree of orientation of the dipoles in a given electric field is a function of how strong are the thermal restoring forces, i.e., of the temperature.

The latter case of the polar molecule was included in order to present a complete picture, for, in the present work, the only molecule included is oxygen,  $O_2$ , which is non-polar, since both "ends" of the molecule are identical. Therefore, the conclusion based on the arguments presented here is that the polarizations, and thus the Gladstone-Dale constants, of the species being studied in this work should not change with temperature. This conclusion is however based on rather simple classical arguments; it is possible that a quantum-mechanical treatment might yield a different conclusion, but this is beyond the scope of this thesis. A detailed discussion of polarization and inter-molecular forces is given in Ref. 8. However, much of the treatment in Ref. 8 concerns liquids, and many of the effects discussed are negligible in the case of a gas.

## 2.2 Application to Interferometry

### 2.2.1 Introduction

Earlier, we denoted the amplitude of the electric and magnetic fields associated with a light wave by:

$$\vec{E} = \vec{E}_0 \exp [i (k^*z - \omega t)]$$

$$\vec{B} = \vec{B}_0 \exp [i (k^*z - \omega t)]$$

where  $k^* = k + i\beta$ ,  $k = \frac{2\pi}{\lambda}$  and  $\omega = 2\pi\nu$

If the medium being considered is a gas, then the conductivity,  $\sigma$ , is small (e.g.,  $10^{-5}$  mhos/m). Therefore, we can assume that there is

no attenuation of the light wave, i.e., that  $\beta = 0$  and  $e^{-\beta z} = 1$ , at least for the distances involved in interferometry. Therefore we may write:

$$\vec{E} = \vec{E}_0 \exp \left[ 2\pi i \left( \frac{z}{\lambda} - vt \right) \right]$$

Up to now, it has been convenient to work with the exponential form in expressing the variation of the quantities associated with a light wave. However for the purposes of this section it is convenient to work with the amplitude of the light wave, which is related to the electric field and can be described by the same function. It is also convenient to use only the real part of the exponential function and write:

$$A = A_0 \cos 2\pi \left( vt - \frac{z}{\lambda} \right)$$

The imaginary part of the exponential could also be used for this purpose; the only difference would be that the cosine is everywhere replaced by sine.

### 2.2.2 The Mach-Zehnder Interferometer

Figure 7 shows the geometrical and optical layout of a Mach-Zehnder interferometer. A more detailed description of the UTIAS 9" interferometer is given in Ref. 3, but a brief summary of the principles involved is included here. Light from the source is formed into a parallel beam of sufficient area and directed to splitter 1, where it is divided into two parts by amplitude division. Part of the original beam is directed to mirror 1 and from there it is passed through the test section to splitter 2. The remaining part of the beam passes from splitter 1 through the compensating chamber, an optical replica of the test section, to mirror 2 and then to splitter 2. At splitter 2, the two parts of the original beam are recombined. Part of the reconstructed beam passes through various lenses and mirrors to the photographic plate, ground-glass screen, or other detector. The remaining part passes out of the system, and is not used, although it could be if convenient.

Let us now assume that conditions inside the test section and inside the compensating chamber are identical, and that the optical path lengths of the test section and compensating chamber beams are equal. This does not necessarily mean that the geometrical path lengths are equal (although they usually are, in practice), but it does mean that the transit times of the two beams, from separation at splitter 1 to recombination at splitter 2, are equal. We also assume that the plates of the interferometer are exactly parallel and perfectly flat, so that the path length at one point in the field of view is the same as at any other point. Under these conditions, the test-section beam and the compensating chamber beam, which were formed from the same beam at splitter 1, will arrive at splitter 2 exactly in phase, and the resultant amplitude will be the same as that of the original beam.

If a change now occurs in the test section conditions, the optical path length seen by the test section beam will also change. This is caused by a change in the velocity of light in the test section, i.e., the wavelength changes (since the frequency is fixed), and these changes show up as a change in the index of refraction. Thus, an optical path difference between the test section and compensating chamber beams is introduced, given

by, in cycles:

$$\frac{L}{\lambda_2} - \frac{L}{\lambda_1}$$

where  $L$  is the geometric width of the test section, and subscripts 1 and 2 denote initial and final conditions in the test section, respectively. In terms of the indices of refraction, this becomes (dropping the subscript  $p$  denoting phase index of refraction)

$$\frac{L}{\lambda_0} (n_2 - n_1)$$

where  $\lambda_0$  is the wavelength in vacuum.

The resultant amplitude seen at the photographic plate is then simply the sum of the amplitudes of the test section and compensating chamber beams, taking into account the phase difference introduced. Here, since we are observing in a fixed position relative to the source and interferometer, we can neglect the  $z$  dependence of the amplitude. It is noted that introducing a path difference has the same effect as adding a phase constant to the test-section beam. Thus:

$$\begin{aligned} A &= \frac{1}{2} A_0 \cos(2\pi \nu t) + \frac{1}{2} A_0 \cos 2\pi \left( \nu t + \frac{L}{\lambda_2} - \frac{L}{\lambda_1} \right) \\ &= A_0 \cos \left( 2\pi \nu t + \frac{\pi L}{\lambda_2} - \frac{\pi L}{\lambda_1} \right) \cos \pi \left( \frac{L}{\lambda_1} - \frac{L}{\lambda_2} \right) \\ &= A_0 \cos \left( 2\pi \nu t + \frac{\pi L}{\lambda_2} - \frac{\pi L}{\lambda_1} \right) \cos \frac{\pi L}{\lambda_0} (n_1 - n_2) \\ &= A_0 \cos \left( 2\pi \nu t + \frac{\pi L}{\lambda_2} - \frac{\pi L}{\lambda_1} \right) \cos \frac{\pi L}{\lambda_0} (n_2 - n_1) \quad (36) \end{aligned}$$

This was obtained using standard trigonometric relations. No account has been taken of the light lost at the second splitter, since this alters the result only by a constant factor.

However, the quantity actually detected by the photographic plate is the intensity of the light, which is given by the square of the amplitude. Furthermore, it is noted that the time variation of the amplitude is at frequency  $\nu$ , which is far too rapid for the human eye or any other sensor to detect. Rather, the sensor sees a time average of the intensity. Therefore:

$$I = A^2 = A_0^2 \cos^2 \left( 2\pi \nu t + \frac{\pi L}{\lambda_2} - \frac{\pi L}{\lambda_1} \right) \cos^2 \frac{\pi L}{\lambda_0} (n_2 - n_1)$$

and

$$\begin{aligned}\bar{I} &= \frac{1}{T} \int_0^T I \, dt = \frac{1}{T} \left[ A_0^2 \cos^2 \frac{\pi L}{\lambda_0} (n_2 - n_1) \right] \int_0^T \cos^2 \left( 2\pi \nu t + \frac{\pi L}{\lambda_2} - \frac{\pi L}{\lambda_1} \right) dt \\ &= \frac{1}{2T} \left[ A_0^2 \cos^2 \frac{\pi L}{\lambda_0} (n_2 - n_1) \right] \left\{ \int_0^T \cos \left( 4\pi \nu t + \frac{2\pi L}{\lambda_2} - \frac{2\pi L}{\lambda_1} \right) dt + \int_0^T dt \right\} \\ &= \frac{1}{2T} \left[ A_0^2 \cos^2 \frac{\pi L}{\lambda_0} (n_2 - n_1) \right] \left\{ \frac{1}{4\pi \nu} \left[ \sin \left( 4\pi \nu t + \frac{2\pi L}{\lambda_2} - \frac{2\pi L}{\lambda_1} \right) \right]_0^T + T \right\}\end{aligned}$$

and taking the limit as  $T$  becomes very large compared to  $\frac{1}{\nu}$ , we obtain:

$$\bar{I} = \frac{A_0^2}{2} \cos^2 \frac{\pi L}{\lambda_0} (n_2 - n_1) \quad (37)$$

Thus the only variation in intensity which can be detected is that due to the change in conditions in the test section. Since we specified that the path length was the same throughout the field of view initially, we see that the intensity will vary in the same way throughout the field, provided that  $n_2$  is uniform throughout the test section. When the argument of the cosine equals an even multiple of  $\pi/2$ , the intensity is a maximum; when the argument equals an odd multiple of  $\pi/2$ , the intensity is zero, and no light is transmitted.

Generally, however, conditions will not change uniformly throughout the test-section; rather,  $n_2$  will vary from one part of the field to another and  $\pi L/\lambda_0 (n_2 - n_1)$  will assume various values. When  $n_2$  varies smoothly (which it does, except through flow discontinuities),  $\pi L/\lambda_0 (n_2 - n_1)$  will also change smoothly, increasing (or decreasing) in value, passing through odd and even multiples of  $\pi/2$ . The result is a set of interference fringes: the contours where  $\pi L/\lambda_0 (n_2 - n_1)$  is an even multiple of  $\pi/2$  show up as bright lines, and the contours where  $\pi L/\lambda_0 (n_2 - n_1)$  is an odd multiple of  $\pi/2$  show up as dark lines, with a continuous variation in brightness between the bright and dark lines. The change in  $n_2$  between adjacent bright (or dark) fringes is given by:

$$\frac{\pi L}{\lambda_0} [(n_2 + \Delta n) - n_1] = \frac{\pi L}{\lambda_0} [n_2 - n_1] + \pi$$

or:

$$\Delta n = \frac{\lambda_0}{L}$$

Therefore, if the index of refraction is known on a given fringe, the index of refraction on any other fringe can be determined.

### 2.2.3 The Parallel Fringe Method

Up to now, it was assumed that the plates of the interferometer were all parallel. We now modify the system by introducing in one of the beams of the interferometer an optical path difference which changes uniformly across the field of view. This is done in the compensating chamber beam (Ref. 3) by rotating mirror 2 through a small angle  $\epsilon$ . The optical path difference thus introduced is (in cycles):

$$\frac{2\epsilon y}{\lambda_a}$$

where  $y$  is measured perpendicular both to the axis of rotation of the mirror and to the direction of propagation of the beam, and where subscript "a" indicates the medium in which the interferometer is immersed, generally air.

It is seen that the effect of this alteration is the same as if the index of refraction in the test section had been made to vary uniformly across the field of view, and the result is straight, uniform fringes. Mathematically, proceeding as before, the resultant amplitude at any point in the field is given by:

$$\begin{aligned} A &= \frac{1}{2} A_0 \cos 2\pi \left( \nu t + \frac{2\epsilon y}{\lambda_a} \right) + \frac{1}{2} A_0 \cos 2\pi \left( \nu t + \frac{L}{\lambda_2} - \frac{L}{\lambda_1} \right) \\ &= A_0 \cos \left( 2\pi \nu t + \frac{\pi L}{\lambda_2} - \frac{\pi L}{\lambda_1} + \frac{2\pi \epsilon y}{\lambda_a} \right) \cos \left( \frac{\pi L}{\lambda_1} - \frac{\pi L}{\lambda_2} + \frac{2\pi \epsilon y}{\lambda_a} \right) \\ &= A_0 \cos \left( 2\pi \nu t + \frac{\pi L}{\lambda_2} - \frac{\pi L}{\lambda_1} + \frac{2\pi \epsilon y}{\lambda_a} \right) \cos \frac{\pi L}{\lambda_0} \left( n_2 - n_1 - \frac{2\epsilon y n_a}{L} \right) \end{aligned} \quad (38)$$

Therefore:

$$I = A_0^2 \cos^2 \left( 2\pi \nu t + \frac{\pi L}{\lambda_2} - \frac{\pi L}{\lambda_1} + \frac{2\pi \epsilon y}{\lambda_a} \right) \cos^2 \frac{\pi L}{\lambda_0} \left( n_2 - n_1 - \frac{2\epsilon y n_a}{L} \right)$$

Here, as in the case of Eq. 36, the time variation of the intensity is at frequency  $\nu$ , and is therefore far too rapid to be detected. Therefore, taking the time average, as before:

$$\bar{I} = \frac{1}{T} \int_0^T I dt = \frac{1}{T} \left[ A_0^2 \cos^2 \frac{\pi L}{\lambda_0} \left( n_2 - n_1 - \frac{2\epsilon y n_a}{L} \right) \right] \int_0^T \cos^2 \left( 2\pi \nu t + \frac{\pi L}{\lambda_2} - \frac{\pi L}{\lambda_1} + \frac{2\pi \epsilon y}{\lambda_a} \right) dt$$

which, on simplifying and taking the limit as  $T$  becomes very large compared to  $1/\nu$ , becomes:

$$I = \frac{A_0^2}{2} \cos^2 \frac{\pi L}{\lambda_0} \left( n_2 - n_1 - \frac{2\epsilon y n_a}{L} \right) \quad (39)$$

This expression is similar to that obtained earlier in Eq. 37 for the infinite fringe method, but now the intensity is also a function

of position  $y$ . When conditions in the test section are constant, i.e.,  $(n_2 - n_1)$  is constant over the field of view, the intensity is governed by changes in the term:

$$\frac{2\epsilon y n_a}{L}$$

and the spacing of the fringes is given by:

$$\frac{\pi L}{\lambda_0} \frac{2\epsilon y n_a}{L} + \pi = \frac{\pi L}{\lambda_0} \frac{2\epsilon(y+d)n_a}{L}$$

or:

$$d = \frac{\lambda_0}{2\epsilon n_a}$$

Generally, however, test section flow conditions will not be uniform and thus the fringes generally will not be straight. Referring to Fig. 8, suppose that two points in the field of view  $P(x_P, y_P)$  and  $Q(x_Q, y_Q)$  are on the same fringe, i.e., that:

$$\frac{\pi L}{\lambda_0} \left( n_2 - n_1 - \frac{2\epsilon y n_a}{L} \right)$$

is a constant. Then:

$$\frac{\pi L}{\lambda_0} \left( n_P - n_1 - \frac{2\epsilon y_P n_a}{L} \right) = \frac{\pi L}{\lambda_0} \left( n_Q - n_1 - \frac{2\epsilon y_Q n_a}{L} \right)$$

or

$$\frac{L}{\lambda_0} (n_P - n_Q) = \frac{L}{\lambda_0} \frac{2\epsilon n_a}{L} (y_P - y_Q) = \frac{1}{d} (y_P - y_Q) \quad (40)$$

Equation 40 is basic to the use of the Mach-Zehnder interferometer: it relates the  $y$ -deflection of the fringes, in terms of fringe spacing, to the change in index of refraction. Since  $\lambda_0$  and  $L$  are known in a given situation and the fringe spacing can be measured, one can then determine the index of refraction over the entire field of view, provided that the index of refraction is known at one point.

If we now introduce the Gladstone-Dale equation, Eq. 34, one can write:

$$n_P - n_Q = \sum_i K_i (\rho_{iP} - \rho_{iQ}) - \frac{1}{2\omega^2} \left[ (\omega_P)_P^2 - (\omega_P)_Q^2 \right]$$

which relates the change in index of refraction to the changes in the partial densities and in the electron number density. If this was substituted into Eq. 40, it is noted that as many equations as there are unknowns would be required to solve for all the mass densities plus the electron number density. If we assume, however, that only one species is present other than electrons, we may write:

$$\frac{1}{d} (y_P - y_Q) = \frac{LK}{\lambda_0} (\rho_P - \rho_Q) - \frac{L}{2\lambda_0 \omega^2} \left[ (\omega_P)_P^2 - (\omega_P)_Q^2 \right] \quad (41)$$

Therefore, having two equations of this form, one could determine the mass density and electron density at any point in the field of view, provided that these quantities were known at one point in the field.

The effect of the electrons is particularly noted. If  $\rho_P > \rho_Q$  for constant  $\omega_P$ , then  $y_P > y_Q$ . But if  $(\rho_P - \rho_Q)$  is held constant and  $[(\omega_P)_P^2 - (\omega_P)_Q^2]$  is allowed to increase, then  $(y_P - y_Q)$  will decrease. So that, if an increase in density produces a positive fringe shift, an increase in electron density will produce a negative fringe shift.

#### 2.2.4 White Light Interference

So far, only interference between monochromatic light beams has been considered. We must now consider interference between beams of "white light", i.e., light containing a range of wavelengths. This change introduces several complications such as dispersive effects, which arise because the index of refraction of a medium is generally a function of wavelength.

It is also impossible to consider interference between beams of white light in the same way as we considered monochromatic interference - as an amplitude phenomenon. Rather, the intensity distribution in a white-light interference pattern must be considered as the superposition of the intensity distributions from an infinite number of monochromatic interferograms at wavelengths within the wavelength range of the white light. This arises from the fact that nothing can be said about the phase differences between the various wavelengths emitted by the source.

For a monochromatic interferogram, the source of light may be considered as the set of oscillators (atoms or molecules) in the source which emit at the particular wavelength in question. Each one of these oscillators emits for only a short time (but still several orders of magnitude longer than  $1/\nu$ ) so that the set of oscillators changes frequently. However, for a given set of oscillators, the light emitted can be said to have a certain phase which is the resultant of the phases of all the individual oscillators; this phase remains constant for the given set of oscillators, since all the oscillators within the set emit at the same frequency. Similarly, if one considers the set of oscillators emitting at a second frequency, the emitted light from these oscillators can also be assigned a resultant phase. But since the frequencies of the light emitted by these two sets of oscillators are different, the phase difference between the two frequencies is always changing. Likewise for all the other wavelengths emitted by the source.

However, as stated above, the set of oscillators emitting at a particular wavelength exists for only a short time; when the set of oscillators changes, the resultant phase undergoes unpredictable changes also. Thus in addition to the variation in phase difference due to the fact that the frequencies are different, there are also random changes in

phase difference due to the changing sets of oscillators, so that it is impossible to predict the changes in phase difference mathematically. Therefore, one cannot consider interference between beams of light of different wavelengths as an amplitude phenomenon, because to do so requires knowledge of the phase difference which is not available. The best that can be done is to consider the energy, or intensity, distribution produced by interference at a given wavelength, about which something can be said, and then integrate over the frequency spectrum to find the resultant intensity distribution.

Some authors have not considered these points when integrating over the frequency spectrum to find the resultant interference pattern. Attempts have been made to work with the amplitude, and in attempting to define the phase differences, the tacit assumptions have been made that, (1), the sets of oscillators which produce each frequency remain the same, so that no random changes in phase occur, and, (2), that the phase differences between all the frequencies are zero at time  $t = 0$ . This produces the not unexpected result that the intensity over the field of view of the interferometer decreases with time, and with distance away from the zero-order fringe, which is not the case. The intensity in the field of view is constant in time, and, while the peak intensity does decrease with distance away from the zero-order fringe, the average intensity is the same over the field of view.

In view of these considerations, a convenient starting point from which to calculate the intensity distribution in a white-light interference pattern is the intensity distribution for a monochromatic interference pattern given by Eq. 39:

$$\bar{I} = \frac{A_0^2}{2} \cos^2 \frac{\pi L}{\lambda_0} \left( n_2 - n_1 - \frac{2\epsilon y n_a}{L} \right) \quad (39)$$

Introducing the Gladstone-Dale equation (Eq. 34) and assuming only one species present other than electrons, Eq. 39 becomes:

$$\bar{I} = \frac{A_0^2}{2} \frac{L}{\lambda_0} \left[ K(\rho_2 - \rho_1) - \frac{1}{2\omega^2} \left( (\omega_p)_2^2 - (\omega_p)_1^2 \right) - \frac{2\epsilon y n_a}{L} \right]$$

or:

$$\bar{I} = \frac{A_0^2}{2} \cos^2 \left[ \frac{\pi L \nu K}{c} (\rho_2 - \rho_1) - \frac{L}{8\pi \nu c} (\omega_p)_2^2 - \frac{2\pi \epsilon y \nu n_a}{c} \right] \quad (42)$$

where  $(\omega_p)_1^2$  has been set equal to zero to correspond to the usual physical situation of no electrons present in the initial state,  $\nu/c$  has been substituted for  $1/\lambda_0$  and  $4\pi\nu^2$  has been substituted for  $\omega^2$ .

We must now determine the spectral intensity distribution of the light. Referring to Fig. 9a, we set:

$$I_0 = \frac{A_0^2}{2} \quad \text{for } \nu_1 < \nu < \nu_2$$

$$I_0 = 0 \text{ for } \nu < \nu_1 \text{ and } \nu > \nu_2$$

The intensity distribution in the white-light interference pattern is then given by:

$$\int_{\nu_1}^{\nu_2} \bar{I} d\nu = \frac{A_0^2}{2} \int_{\nu_1}^{\nu_2} \cos^2 \left[ \frac{\pi L \nu K}{c} (\rho_2 - \rho_1) - \frac{L}{8\pi \nu c} (\omega_p)^2 - \frac{2\pi \epsilon \nu n_a}{c} \right] d\nu \quad (43)$$

We must now introduce frequency dependent expressions for the indices of refraction and the Gladstone-Dale constant. This can be done through the Cauchy relation (Ref. 14):

$$n - 1 = A + B\nu^2 + C\nu^4 + \dots$$

$$K = K_0 + K_2\nu^2 + K_4\nu^4 + \dots$$

Having thus accounted for the frequency dependence of the indices of refraction and the Gladstone-Dale constant, Eq. 43 can be integrated, and the details are given in Appendix A. The result is:

$$\bar{I} = \frac{A_0^2}{4} \left\{ 1 + \frac{\sin \{ [X_1(\rho_2 - \rho_1)(\Delta_0 + \Delta_1) - X_2\nu(1 + \Delta'_0 + \Delta'_1) + X_3] (\nu_2 - \nu_1) \}}{[X_1(\rho_2 - \rho_1)(\Delta_0 + \Delta_1) - X_2\nu(1 + \Delta'_0 + \Delta'_1) + X_3] (\nu_2 - \nu_1)} \right. \\ \left. \times \cos \{ 2 [X_1(\rho_2 - \rho_1) \Delta_0 - X_2\nu(1 + \Delta'_0) - X_3] \nu \} \right\} \quad (44)$$

$$\text{where: } \nu = \frac{\nu_2 + \nu_1}{2}$$

$$X_1 = \frac{\pi L}{c} ; X_2 = \frac{2\pi \epsilon}{c} ; X_3 = \frac{Le^2 N_e}{8\pi \epsilon_0 m_e \nu^2}$$

and where, as shown in Appendix A:

- $(1 + \Delta'_0)$  corresponds to the phase index of refraction of the air in which the interferometer is immersed.
- $(1 + \Delta'_0 + \Delta'_1)$  corresponds to the group index of refraction of the air in which the interferometer is immersed
- $\Delta_0$  is the Gladstone-Dale constant of the gas in the test section, which is analogous to the phase index of refraction, of the gas, and
- $(\Delta_0 + \Delta_1)$  is the Gladstone-Dale constant of the gas in the test section, which is analogous to the group index of refraction of the gas.

Equation 44 shows that a white-light interference pattern consists of a background intensity,  $A_0^2/4$ , on which is superimposed a sinusoidal variation governed by frequency  $\nu$ , which is in turn modulated by a

sine wave governed by frequency  $(\nu_2 - \nu_1)$ . It is also noted that as  $(\rho_2 - \rho_1)$  varies from zero, the position of the zero-order fringe (i.e., the value of  $y$  for which the argument of the cosine is zero), and the position of the maximum of the modulating function, or envelope, (i.e., the value of  $y$  for which the argument of the sine is zero) vary from zero also. However, the values of  $y$  which result in the arguments of the sine and cosine being equal to zero are different, except when  $X_3$  (i.e., the electron number density) and  $(\rho_2 - \rho_1)$  equal zero. It is noted too that the contrast of the fringes, in addition to being controlled by the sine function, decreases as distance from the position of the maximum of the envelope increases. These effects, and others described below, are demonstrated in the numerical calculations included in Appendix A.

Of particular interest is the contribution of the electrons; in the cosine factor this term is negative, while in the sine factor this term is positive. This indicates, as noted in connection with Eq. 41, that the electrons produce a negative shift of individual fringes, but a positive shift of the envelope of the intensity distribution. It is also noted that the effect of the electrons is frequency dependent, since  $X_3$  contains a factor  $(\bar{\nu})^{-2}$ . Therefore, the effect of the electrons will be less at shorter wavelengths, toward the violet end of the spectrum, and greater at longer wavelengths, toward the red end of the spectrum.

It is noted too that Eq. 44 produces the correct results in the limits as  $(\nu_2 - \nu_1) \rightarrow \infty$  and as  $(\nu_2 - \nu_1) \rightarrow 0$ . As  $(\nu_2 - \nu_1) \rightarrow 0$ , the range of wavelengths becomes more and more narrow until, in the limit, only one wavelength,  $\bar{\nu}$ , remains, and the white-light interferogram becomes a monochromatic interferogram. In Eq. 44, as  $(\nu_2 - \nu_1) \rightarrow 0$ , the argument of the sine approaches zero for all values of  $(\rho_2 - \rho_1)$ ,  $y$ , and  $N_e$ , and since:

$$\lim_{x \rightarrow 0} \frac{\sin x}{x} = 1 \text{ and } \frac{1}{2} (1 + \cos 2x) = \cos^2 x \quad (45)$$

it is seen that Eq. 44 degenerates to Eq. 39, after allowance is made for the changes in notation.

As  $(\nu_2 - \nu_1) \rightarrow \infty$ , it is seen that the coefficient of the cosine factor approaches zero, since:

$$\lim_{x \rightarrow \infty} \frac{\sin x}{x} = 0$$

and the intensity becomes equal to  $A_0^2/4$  everywhere except at the position of the maximum of the envelope. At this point the argument of the sine is zero, regardless of the value of  $(\nu_2 - \nu_1)$ , and the former limit given in Eq. 45 holds. Thus, at the position of the maximum of the envelope, the maximum intensity possible is  $A_0^2/2$ , subject to modulation by the cosine factor, and only one fringe remains.

Most important however is the form of the indices of refraction which appear in Eq. 44. Assuming for the moment that no electrons are present, (the effect of electrons was considered earlier) it is noted that the shift of individual fringes with frequency  $\bar{\nu}$  is controlled by  $\Delta_0$  and  $(1 + \Delta'_0)$ , while the shift of the envelope with frequency  $(\nu_2 - \nu_1)$  is controlled by  $(\Delta_0 - \Delta_1)$  and  $(1 + \Delta'_0 + \Delta'_1)$ . Thus, as mentioned earlier, the

envelope will be shifted by a different amount than will be individual fringes for a given change in  $(\rho_2 - \rho_1)$ . This effect is known as "rollover" (Ref. 5), and the reason for its occurrence is shown in Appendix A.

### 3. EXPERIMENTAL RESULTS FOR OXYGEN

#### 1) Procedure and Method of Analysis

The basic method which was used to determine the Gladstone-Dale constants has been outlined in Appendix B of Ref. 1. This involved passing a strong shock wave through the gas under study and measuring the index of refraction of the hot dissociating gas behind the shock wave. This could be done in the UTIAS 4" x 7" Shock Tube, using the 9" Mach-Zehnder interferometer to measure the index of refraction. A convenient reference index of refraction was that of the cold gas ahead of the shock wave, for which all the parameters of state were known, while the change in the index of refraction between the shocked and unshocked gas could be determined from an instantaneous interferogram of the shock wave as it passed through the field of the interferometer.

As noted above, all the required parameters of the gas ahead of the shock wave were known. Also, the Gladstone-Dale constants at various wavelengths for various gases have been determined from room-temperature conditions, and were available in Ref. 6. For the shock-heated gas, the required state parameters could not be determined directly. Consequently, values of the density ratio across the shock wave, had to be determined from the initial conditions, using normal shock calculations. Using this data, it was then possible to determine the Gladstone-Dale constants for the hot gas from the refractive index measurements.

For the case of oxygen, the contribution of the electrons produced by the shock wave, to the total refractivity of the gas, can be neglected ( $\omega_p^2 / 2\omega^2 \approx 10^{-16}$ ), so that the Gladstone-Dale equation (Eq. 34) for the shocked gas becomes:

$$n_2 - 1 = \sum_i K_i \rho_i$$

or

$$n_2 - 1 = \rho_2 [K_M (1 - \alpha_2) + K_A \alpha_2] \quad (45)$$

where  $\rho_2$  is the total density of the shocked gas,  $\alpha_2$  is the degree of dissociation, i.e., the fraction of the oxygen molecules that are split up into their component atoms,  $K_M$  is the Gladstone-Dale constant for the oxygen molecule, and  $K_A$  is the Gladstone-Dale constant for the oxygen atom.

Similarly, for the cold gas ahead of the shock wave, Eq. 34 becomes:

$$n_1 - 1 = \rho_1 K_{O_2} \quad (46)$$

where  $K_{O_2}$  is the Gladstone-Dale constant of the oxygen molecule at room temperature, as given in Ref. 6. On the basis of the arguments present in Sec. 2.1.5,  $K_{O_2}$  would be expected to be equal to  $K_M$ , in spite of the vastly

different temperatures involved in the two determinations. However, one of the objectives of this experimental work is to check this point, and therefore, for the sake of generality, no assumption is made regarding the value of  $K_M$ .

The relation between the non-dimensional fringe shift and the change in index of refraction is given by (Eq. 40):

$$\frac{L}{\lambda_0} (n_P - n_Q) = \frac{L}{\lambda_0} \frac{2\epsilon n_a}{L} (y_P - y_Q) = \frac{1}{d} (y_P - y_Q) = S_{QP} \quad (40)$$

If  $n_Q$  represents the initial state 1 ahead of the shock wave on the interferogram, and  $n_P$  represents the final state 2 behind the shock wave, one can substitute from Eqs. 45 and 46 for  $n_P$  and  $n_Q$  respectively and obtain:

$$\frac{L}{\lambda_0} \rho_2 \left[ K_M (1 - \alpha_2) + K_A \alpha_2 \right] - \frac{L}{\lambda_0} \rho_1 K_{O_2} = S_{12}$$

or

$$K_M \left[ \frac{L}{\lambda_0} \rho_2 (1 - \alpha_2) \right] + K_A \left[ \frac{L}{\lambda_0} \rho_2 \alpha_2 \right] = S_{12} + \rho_1 \frac{L}{\lambda_1} K_{O_2} \quad (47)$$

Equation 47 contains two unknowns, so that one determination of  $S_{12}$  would not provide enough information. A minimum of two equations of this form are required to determine both  $K_M$  and  $K_A$ , i.e., two independent runs in the shock tube are required.

This procedure of using two simultaneous equations to determine  $K_M$  and  $K_A$  was that suggested in Appendix B of Ref. 1. However, it had to be discarded since it was found that the values obtained for  $K_M$  and  $K_A$  were extremely sensitive to small errors in the measurement of the fringe shifts. An alternative procedure was that used in Ref. 7, where  $K_M$  was arbitrarily set equal to  $K_{O_2}$ , thus eliminating one unknown. This allowed  $K_A$  to be determined from only one measurement of fringe shift, and the error in  $K_A$  resulting from an error in  $S_{12}$  was much reduced. However, while on the basis of the classical arguments presented earlier, there is some justification for setting  $K_M$  equal to  $K_{O_2}$ , until this equality is actually proved to be so, the value obtained for  $K_A$  is still open to question, since it is influenced by the choice of the value of  $K_M$ .

Obviously, it would be desirable to remove this assumption, and so a new procedure\* was developed. It was better in that it removed the assumption of a value for  $K_M$ , and allowed a large number of determinations of  $S_{12}$  to be used to obtain one pair of values for  $K_M$  and  $K_A$ . This method is outlined below.

---

\* The author is indebted to Dr. A. Levy for the original suggestion leading to the development of this method.

Equation 47 can be written in the form:

$$\frac{L}{\lambda_0} \rho_2 \left[ K_M (1 - \alpha_2) + K_A \alpha_2 \right] = S_{12} + \rho_1 \frac{L}{\lambda_0} K_{O_2} \quad (48)$$

or:

$$\frac{L}{\lambda_0} \rho_2 [K'] = S_{12} + \rho_1 \frac{L}{\lambda_0} K_{O_2}$$

where:

$$K' = K_M (1 - \alpha_2) + K_A \alpha_2 \quad (48a)$$

It is seen that  $K'$  is the specific refractivity of the mixture of  $O_2$  and  $O$ , and the value of  $K'$  changes depending on the value of  $\alpha_2$ . In particular, at  $\alpha_2 = 0$ ,  $K'$  becomes equal to  $K_M$ , and at  $\alpha_2 = 1$ ,  $K'$  becomes equal to  $K_A$ . Also, if Eq. 48a is written in the form:

$$K' = K_M + \alpha_2 (K_A - K_M) \quad (48b)$$

it is seen that the value of  $K'$  varies linearly with  $\alpha_2$ , since  $K_A$  and  $K_M$  are constants for the gas under study. Thus, if  $K'$  is plotted versus  $\alpha_2$ , and a straight line is drawn through the points, it is seen that the intercept at  $\alpha_2 = 0$  gives a value of  $K_M$  and the intercept at  $\alpha_2 = 1$  gives a value of  $K_A$ . The value of this procedure is that there is no limit to the number of points  $K'$  versus  $\alpha_2$  that can be used, i.e., the number of runs in the shock tube, since each run produces one point of  $K'$  versus  $\alpha_2$ , and every additional point or run reduces the uncertainty in the slope and intercepts of the line drawn through the points.

The criteria for choosing running conditions in the shock tube can be obtained with the aid of Eq. 48. Solving for  $K'$  in Eq. 48, one obtains:

$$K' = \frac{S_{12}}{\frac{L}{\lambda_0} \rho_2} + \frac{\rho_1}{\rho_2} K_{O_2}$$

and if one assumes that  $\rho_1$ ,  $L$ ,  $\lambda_0$ , and  $K_{O_2}$  are known exactly, one can write:

$$\Delta K' = \frac{\Delta S_{12}}{\frac{L}{\lambda_0} \rho_2} + \left( \frac{S_{12}}{\frac{L}{\lambda_0}} + \rho_1 K_{O_2} \right) \frac{\Delta \rho_2}{\rho_2^2} \quad (49)$$

where  $\Delta K'$ ,  $\Delta S_{12}$ , and  $\Delta \rho_2$  are the errors in these quantities, and where  $\Delta K'$  is the sum of the errors in the terms involving  $\Delta S_{12}$  and  $\Delta \rho_2$ . Thus it is seen that the error in  $K'$  may be reduced by raising the density of the shocked gas,  $\rho_2$ . Also, since it is the intercepts at  $\alpha_2 = 0$  and  $\alpha_2 = 1$  that are wanted, it is desirable to obtain points with  $\alpha_2$  as low as possible and also with  $\alpha_2$  as high as possible. Obviously, the limits on the choice of running conditions are set by the structural strength of the shock tube. In addition, it was desired to keep the temperature of the shocked gas within the range of approximately 3300°K to 4400°K, which was roughly the temperature range involved in the oxygen expansion studies (Ref. 1) which the present work supports. The change with temperature of the Gladstone-Dale

constants would then be shown by the difference between  $K_{O_2}$ , the room-temperature value for the oxygen molecule, and  $K_M$ , the value obtained in the present work at the elevated temperature. Also, any variation of the Gladstone-Dale constants with temperature within the range chosen for this work would show up as scatter in the points  $K'$  vs  $\alpha_2$ , and the scatter would show some sort of trend with temperature.

The best way to fit a straight line to the values of  $K'$  vs  $\alpha_2$  is to use a least squares analysis; however, the procedure is not as straight forward as usual in this case. Normally, in minimizing the sum of the squares of the deviations, one assumes that the variances of all the points are equal. This would be unrealistic in the present case, since the variances are in fact not equal, as indicated by the estimated error (See Table 3). Consequently, a quantity  $p$  is calculated for each point such that  $p$  is proportional to the inverse of the estimated percent error of the point. Thus, instead of one point at each location, one assumes  $p^2$  points, where  $p^2$  is not necessarily an integer. The equations giving the slope ( $K_A - K_M$ ) and the intercept  $K_M$  at  $\alpha_2 = 0$  then become (see Eq. 48b)

$$\begin{aligned} (K_A - K_M) \sum p^2 \alpha^2 - \sum p^2 \alpha K' + K_M \sum p^2 \alpha &= 0 \\ (K_A - K_M) \sum p^2 \alpha - \sum p^2 K' + K_M \sum p^2 &= 0 \end{aligned} \quad (50)$$

These equations could also be solved for  $K_A$  and  $K_M$  explicitly.

A measure of the percent error at the intercepts can be obtained from:

$$\delta = \delta' \left[ \frac{1}{\sum p^2} + \frac{(\alpha - \overline{p^2 \alpha})^2}{\sum [p^2 (\alpha - \overline{p^2 \alpha})^2]} \right]^{\frac{1}{2}} \quad (51)$$

$$\text{where: } \overline{p^2 \alpha} = \frac{\sum p^2 \alpha}{\sum p^2}$$

where  $\delta$  is the percent error of the point at abscissa  $\alpha$  and  $\delta'$  is the percent error of the point (possibly hypothetical) for which the quantity  $p$  is equal to one. The expression in Eq. 51 was originally derived (Ref. 15) for standard deviation, but it is assumed here that the percent error is proportional to the standard deviation and that they remain proportional throughout the calculations.

(Equations 50 and 51 are actually adaptations of expressions derived for the case of equal variance in all the points. However, once the method for weighting the points has been decided, the forms shown in Eqs. 50 and 51 follow immediately. The particular method of weighting used here was decided upon so that the results obtained for  $\delta$  using Eq. 51 would be independent of the actual numerical magnitude of  $p$ , the only requirement being that  $p$  be proportional to the inverse of the estimated percent error, as detailed earlier. The condition that  $\sum p^2$  must be equal to the number of points is required for the test of significance which is applied in Sec. 3.2 to determine whether the difference between the results for  $K_M$  and  $K_A$  is significant in view of the experimental error (See Ref. 15). The result of this test is influenced by the magnitude of  $\sum p^2$  and, since in the original equal-variance version of this test the quantity corresponding to  $\sum p^2$  was the number of experimental points, it was decided to set  $\sum p^2$  equal to the number of points).

### 3.2 Experimental Results and Error Analysis

A summary of the runs in the UTIAS 4" x 7" Shock Tube used for the determination of the Gladstone-Dale constants for dissociating oxygen is shown in Table 1. Twelve runs were taken: shock Mach numbers varied between 8.86 and 16.64, while initial pressure varied from 3.99 mm Hg to 54.0 mm Hg. It is also noted that the initial temperature did not vary more than one degree Kelvin from 300°K.

As mentioned before, the state parameters of the gas behind the shock wave had to be determined from normal shock calculations, and it was plain that any results obtained for the Gladstone-Dale constants would be only as accurate as the calculations used. Fortunately, suitable normal shock data was obtainable from Ref. 13. This data was calculated for  $T_1$  of 300°K, which was in line with the actual  $T_1$  in the shock tube. From this data, values of the degree of dissociation of the shock-heated gas, the density ratio across the shock wave, and the equilibrium temperature of the hot gas were obtained for each run.

Of major importance too was the accuracy with which measurements of fringe shift on the interferograms could be made. Prints made from typical interferograms are shown in Figs. 1, 2, and 3. Since the fringes were discontinuous across the shock wave, use had to be made of a white-light interferogram, taken at the same time as the monochromatic interferogram, in order to trace the zero-order fringe across the shock front. This was possible because, as shown in Figs. 1 and 2, only a few fringes on either side of the zero-order fringe are visible on a white light interferogram. However, the phenomenon of "rollover", which becomes important when there are large density changes, meant that great care had to be exercised when using the white-light fringes to identify the zero-order fringe (See Sec. 2.2.4 and Appendix A).

In addition, care had to be exercised when measuring the fringe-shift since the shock front was so badly blurred on the earlier interferograms such as in Fig. 1. These interferograms were taken with a magnesium spark source in the interferometer, which limited the time resolution on the interferograms to about two microseconds. Consequently, account had to be taken of the curvature of the fringes between the two points of measurement in front of and behind the shock wave, since these points were far apart due to the apparent thickness of the shock front. Later interferograms were taken with the exploding wire light source and a Kerr Cell (See Appendix C) which improved the time resolution by a factor of 10. The difference in sharpness of the shock front is readily apparent in the interferograms shown in Fig. 3.

Another difficulty which had to be contended with is apparent in Fig. 1b. This was the so-called "phasing" of the white-light fringes, in which the fringe envelope of the white-light fringes moved with respect to individual fringes as one followed the fringes from one side of the interferogram to the other. This phasing was very similar to rollover except that it was a function of the optics of the interferometer, not of a density change, since phasing was present on the no-flow as well as the flow interferograms. As a result, determination of the position of the zero-order fringe from an estimate of the rollover on the white-light interferograms was a very difficult matter. Eventually, the problem was overcome by

taking a series of densitometer traces across the white-light fringe pattern at various positions on both the flow and no-flow interferograms. Since the phasing was present on both the flow and no-flow interferograms, while the rollover was present only on the flow interferograms, it was possible to separate the "rollover" from the "phasing" using the densitometer traces, and thus identify the zero-order fringe.

No explanation for this phasing could be advanced. Eventually it disappeared and was replaced by another effect which is apparent in Fig. 2. Here, the spacing of the fringes varied across the white-light pattern, and the fringe envelope was not symmetrical about its maximum. Although the interferograms shown in Fig. 2 were taken with the exploding wire source and Kerr Cell, the disappearance of the phasing and the appearance of the asymmetric white-light fringe pattern did not correspond to the introduction of the exploding wire light source; this change was apparent in other work done with the magnesium spark source before the exploding wire light source was introduced. Again, no explanation could be advanced for this effect.

However, the disappearance of the phasing made it possible to determine the amount of rollover by inspection since it was no longer complicated by other effects, and thus identification of the zero-order fringe became relatively simple. This was fortunate, because these particular interferograms were taken with the exploding wire source, and grain problems resulting from the use of extremely high-speed film (See Appendix C), along with the fact that so many fringes were visible in the white-light pattern, made densitometer traces taken on these interferograms rather hard to interpret.

After the position of the zero-order fringe had been determined on both sides of the shock wave for the white-light interferograms, the dimensional fringe shift was determined using a travelling microscope. This measurement was then transferred to the monochromatic interferogram and accurate measurements of the dimensional fringe shift and of the fringe spacing were made, from which the non-dimensional fringe shift,  $S_{12}$ , was determined. It was found that the dimensional fringe shifts on the white-light and monochromatic interferograms were never quite the same. This caused some difficulty at first until it was realized that, unless the wavelength of the monochromatic interferogram and the wavelength corresponding to the spacing of individual fringes on the white-light interferogram were the same, dispersive effects would result in the dimensional fringe shifts being slightly different. In addition, the monochromatic and white-light interferograms were taken with different camera backs, so that the magnifications were likely to be slightly different, due to small differences in focussing. It was also found to be of some importance to identify the zero-order fringes. This was necessary because it was found that the monochromatic fringe spacing tended to change slightly across the field, possibly due to imperfections in the interferometer optics, together with small vibrations transferred to the interferometer from the building. This change in fringe spacing was not important in itself, but it meant that, unless one transferred to dimensional fringe shift on the white-light interferograms to the corresponding fringes on the monochromatic interferograms, the dimensional white-light fringe shift would not correspond to actual fringes on the monochromatic interferograms, leading to possible errors.

When all factors were taken into account, it was judged that the error in the fringe shift measurements was about 0.1 fringe. Measurements on the earlier interferograms taken with the magnesium spark source could be repeated to better than 0.1 fringe, but it was felt that allowance had to be made for systematic errors arising from the blurring of the shock front. For the interferograms taken with the exploding wire source and the Kerr Cell, it was judged that systematic errors were much reduced due to the enhanced crispness of the fringes and the better definition of the shock front. However, due to variations in film and in processing, some of the interferograms were not of the best quality, and overall accuracy of better than 0.1 fringe could not be claimed.

Having determined the fringe shifts, it was then possible to calculate values of  $K'$  and the details of these calculations are shown in Table 2. The values of the parameters which entered into the calculations are also shown. In particular, the initial density,  $\rho_1$ , was calculated from the pressure and the temperature using the perfect gas law, a good approximation at the low temperatures and pressures involved. The values of  $K'$  were then plotted as shown in Fig. 4.

Before a least squares analysis could be carried out to find the best straight line through the points, an estimate had to be made of the error to be expected in  $K'$ . How these errors enter is shown in Eq. 49. As mentioned above, the error in  $S_{12}$  was estimated as 0.1 fringe. A further error entered in due to uncertainties in the measurement of shock speed, and the effects of this are shown in Table 3, where estimates have been made of the resultant errors in  $\alpha_2$  and  $\rho_2/\rho_1$ . Fortunately,  $\alpha_2$  does not enter into the calculation of  $K'$ , but it does determine the position of the  $K'$  vs  $\alpha_2$  plot used to calculate the intercepts. However it is seen from Fig. 4 that the error in  $\alpha_2$ , ranging from .004 to .015 is small compared to the error in  $K'$  itself.

It is seen, however, that the errors in  $K'$  resulting from errors in  $\rho_2/\rho_1$  are comparable to the errors resulting from uncertainties in  $S_{12}$  and points up the necessity of accurately determining shock speed. The details of these calculations are shown in Table 3.

It was determined that errors in  $K'$  and  $\alpha_2$  arising from uncertainties in the initial pressure could be neglected. The uncertainty in  $p_1$  was  $\pm .05$  mm Hg.

Having then determined the total error in  $K'$ , which ranged from .80% to 2.78%, a least squares analysis was carried out using Eqs. 50, and the result of the calculation is shown in Fig. 4. It is noted that the deviations of the points from the line agree very well with the errors calculated on the basis of estimated error in fringe shift and shock speed measurements. The actual deviations of the points  $K'$  from the line are listed in Table 3 for comparison with the estimated errors.

Finally, the errors in the intercepts were determined using Eq. 51, leading to the final results:

$$K_M = 1.93 \times 10^{-4} \frac{\text{m}^3}{\text{kg}} \pm 1\%$$

$$K_A = 2.04 \times 10^{-4} \frac{\text{m}^3}{\text{kg}} \pm 2\%$$

The value here obtained for  $K_M$  can be compared to  $1.902 \times 10^{-4}$  m<sup>3</sup>/kg, the value of the Gladstone-Dale constant for oxygen at room temperature as given in Ref. 6. It is noted that the value given in Ref. 6 falls only just outside the experimental error in the present result. This agreement was considered to be quite good, considering the radically different methods used to obtain the two values. This agreement would also tend to confirm the conclusion reached in Sec. 2.1.5 that the Gladstone-Dale constants for oxygen do not change with temperature. Greater certainty in this respect will have to await new developments leading to reduction in the errors in  $S_{12}$  and  $\rho_2/\rho_1$ .

The value obtained for  $K_A$  can be compared to  $1.8 \times 10^{-4}$  m<sup>3</sup>/kg  $\pm$  12% as obtained in Ref. 7. However, the work of Ref. 7 was carried out using a smaller shock tube and much lower densities than were used in the present work, so that the experimental error was much higher than in the present work. Also, as mentioned earlier, the result of Ref. 7 for  $K_A$  assumed that  $K_M$  was equal to  $K_{O_2}$ , thereby casting doubt on the reliability of the value obtained for  $K_A$ . In view of the present work, however, it would appear that the assumption of  $K_M$  equal to  $K_{O_2}$  was valid, so that the present result for  $K_A$  and that of Ref. 7 can be considered on roughly equal footing. It is then noted that, when the experimental errors are taken into account, the two results are in agreement. The result of the present work however is considered more reliable in view of the much lower experimental error.

It was noted that the present work indicated that the Gladstone-Dale constant for the atom was greater than that for the molecule, rather than smaller as indicated by the result of Ref. 7. As a further check on this, a statistical test was applied to the graph shown in Fig. 4 to determine whether the slope of  $K'$  vs  $\alpha_2$  was significant in view of the scatter of the points and the experimental error in each point (see Ref. 15). The hypothesis tested was that the slope  $K'$  versus  $\alpha_2$  was zero, and it was found that, at 5% significance level, the slope of the line  $K'$  versus  $\alpha_2$  was significant\*, indicating that  $K_A$  was indeed greater than  $K_M$ .

As a further check on the validity of the results, two tests were applied to ascertain that there were indeed no temperature effects and no density effects. These effects (if any) were ignored in the analysis used to obtain  $K_M$  and  $K_A$ , but if they were present, their effect would show up as scatter in the points, and the scatter would be correlated in some way with the temperature and/or density. Therefore, the deviation of each point from the mean line in Fig. 4 has been plotted against temperature  $T_2$  in Fig. 5, and against density in Fig. 6. The scatter appears to be completely random in both cases, indicating that temperature and density effects are not present.

---

\* This means that, if the slope were indeed zero, and the twelve runs were repeated an infinite number of times, the slope of the line  $K'$  versus  $\alpha_2$  would assume many different values, averaging to zero. The statistical test arrives at two extreme values for the slope such that 95% of all the values obtained for the slope would fall within the range defined by the two extremes. In the present case, the actual value of the slope falls outside this range, and the conclusion is reached that the slope is significant, i.e., that the slope is different from zero.

#### 4. CONCLUSIONS

An experimental determination of the Gladstone-Dale constants for molecular and atomic oxygen was carried out using the UTIAS 4" x 7" Hypersonic Shock Tube. The values obtained were  $1.93 \times 10^{-4} \text{ m}^3/\text{kg} \pm 1\%$  for molecular oxygen, and  $2.04 \times 10^{-4} \text{ m}^3/\text{kg} \pm 2\%$  for atomic oxygen.

The result obtained for the Gladstone-Dale constant of the oxygen molecule was in good agreement with the accepted room temperature value (Ref. 6) of  $1.902 \times 10^{-4} \text{ m}^3/\text{kg}$ . This appeared to confirm the conclusion, based on classical arguments, that the Gladstone-Dale constants for oxygen do not change with temperature.

The value previously obtained by Alpher and White (Ref. 7) for the Gladstone-Dale constant of the oxygen atom was  $1.8 \times 10^{-4} \text{ m}^3/\text{kg} \pm 12\%$ . However, the work of Ref. 7 involved the assumption of a value for the specific refractivity of the oxygen molecule. This condition was removed in the present work, so that the value here obtained for the specific refractivity was free of any assumptions. In addition, the experimental error in the present work was much lower than in Ref. 7.

A number of tests were carried out to test the validity of the results obtained. A statistical test was carried out to determine whether the difference in the results obtained for the specific refractivities of the molecule and atom was significant in view of the experimental error in the points; the result showed that the refractivities were indeed different. Tests applied to determine whether there was any temperature or density effects in the results showed that these effects were absent.

In addition to the experimental work, a theoretical analysis was carried out in which expressions for the index of refraction of dissociating and ionizing gases were derived from Maxwell's equations and the equations of motion for a plasma. The role of the Gladstone-Dale constant was shown along with its relation to the polarizability of molecules and atoms. A further analysis was then done to show the application of the indices of refraction to interferometry and to show analytically how monochromatic and white-light interference patterns are formed.

### REFERENCES

1. Glass, I.I.  
Kawada, H. Prandtl-Meyer Flow of Dissociated and Ionized Gases. UTIAS Report No. 85 (June 1962).
2. Boyer, A.G. Design, Instrumentation, and Performance of the UTIAS 4" x 7" Hypersonic Shock Tube. UTIAS Report No. 99 (May 1965).
3. Hall, J.G. The Design and Performance of a 9" Plate Mach-Zehnder Interferometer, UTIAS Report No. 27 (March 1954).
4. Wong, H.  
Bershader, D. Interferometric Study of Thermal Equilibrium of a Shock-Heated Plasma. Stanford University, Quarterly Technical Summary Report on Direct Energy Conversion Systems, Supplement 2 (April 1964).
5. Curtis, C.W. Use of White Light in the Measurement of Gas Density by Optical Interferometry. Lehigh University Technical Report No. 9 (February 1958).
6. Edelman, G.M.  
Bright, M.H. The Specific Refractivity of Gases for Various Wavelengths of Light. Massachusetts Institute of Technology Gas Turbine Laboratory Report No. 6 (1948).
7. Alpher, R.A.  
White, D.R. Optical Refractivity of High-Temperature Gases: 1, Effects Resulting from Dissociation of Diatomic Gases; 2, Effects Resulting from Ionization of Monatomic Gases. Physics of Fluids 2, 2, p. 153 (1959).
8. Debye, D. Polar Molecules. The Chemical Catalog Co. Inc., 1929 (Dover Publications, 1961).
9. Corson, D.R.  
Lorrain, P. Introduction to Electromagnetic Fields and Waves. W.H. Freeman and Company, 1962.
10. Whitmer, R.M. Electromagnetics. Prentice-Hall Incorporated, 1962.
- 11a) Arave, R.J.  
Huseby, O.A.  
Mahugh, R.A.  
Brown, E.A. Aerothermodynamic Properties of High Temperature Argon. The Boeing Company, Document No. D2-11238 (1962).
- 11b) Arave, R.J.  
Brown, E.A. Thermodynamic and Normal Shock Properties of Inert Gases in Ionization Equilibrium. The Boeing Document D2-22291 for Argon only.
- 12a) Bernstein, L. Tabulated Solutions of Equilibrium Gas Properties Behind the Incident and Reflected Normal Shock Wave in a Shock Tube: I, Nitrogen; II, Oxygen. ARC CP No. 626 (1963).

- 12b Bernstein, L. Private Communication (Extension of above tables for case of Incident Shock in Oxygen only).
- 13 Private Communication. Avco Corporation, Research and Advanced Development Division.
- 14 Jenkins, F.A. Fundamentals of Optics. McGraw-Hill, London  
White, H.E. (1951).
- 15 Li, J.C.R. Introduction to Statistical Interference,  
Edwards Brothers, Inc., Ann Arbor, Michigan  
(1957).
- 16 Private Communication. Stanford University,  
Plasma Physics Group.

TABLE 1

Summary of Runs in the UTIAS 4" x 7" Shock Tube Used to Determine the Gladstone-Dale Constants

Run	$M_s$	$P_1$	$T_1$	$\alpha_2$	$\rho_2/\rho_1$	$T_2$
114	13.48	8.05 mm Hg	299.6°K	.343	13.41	3935°K
115	12.46	17.4 "	300.4 "	.256	12.21	3925 "
116	11.61	24.2 "	299.8 "	.195	11.34	3835 "
117	11.99	15.0 "	299.4 "	.226	11.90	3810 "
118	16.64	3.99 "	299.3 "	.630	15.58	4295 "
119	15.12	9.94 "	300.0 "	.473	14.27	4265 "
120	9.57	38.0 "	299.1 "	.0793	9.27	3460 "
121	10.19	12.6 "	300.1 "	.122	10.27	3440 "
197	8.86	54.0 "	300.9 "	.0496	8.44	3310 "
198	13.20	21.5 "	299.3 "	.304	12.63	4110 "
200	15.75	7.50 "	300.6 "	.534	14.77	4300 "
201	15.64	7.50 "	299.9 "	.524	14.72	4280 "

TABLE 2  
Calculation of K'

Run	$\rho_1$	$\rho_2$	$S_{12}$	$K'$
114	$1.378 \times 10^{-2} \text{ kg/m}^3$	$.1848 \text{ kg/m}^3$	6.50	$1.945 \times 10^{-4} \text{ m}^3/\text{kg}$
115	2.971 " "	.3628 "	13.00	1.993 " "
116	4.140 " "	.4695 "	16.50	1.970 " "
117	2.570 " "	.3058 "	10.88	1.984 " "
118	.6838 " "	.1065 "	3.78	1.942 " "
119	1.699 " "	.2424 "	8.70	1.974 " "
120	6.516 " "	.6040 "	20.20	1.920 " "
121	2.153 " "	.2211 "	7.53	1.931 " "
197	9.205 " "	.7769 "	26.00	1.942 " "
198	3.648 " "	.4653 "	16.40	1.958 " "
200	1.280 " "	.1891 "	6.83	1.981 " "
201	1.283 " "	.1889 "	6.94	2.013 " "

TABLE 3

Error in Values of K'

Run	Error in $M_s$		Error in $\alpha_2$	Error in $\rho_2/\rho_1$
	absolute	percent		
114	$\pm .10$	$\pm .73$	$\pm .008$	$\pm .069$
115	.08	.68	.006	.065
116	.07	.63	.004	.061
117	.08	.65	.006	.067
118	.15	.90	.015	.047
119	.12	.82	.011	.060
120	.05	.52	.002	.048
121	.06	.55	.003	.062
197	.04	.48	.002	.039
198	.09	.71	.007	.059
200	.13	.85	.012	.059
201	.13	.85	.012	.059

TABLE 3 (con'd)

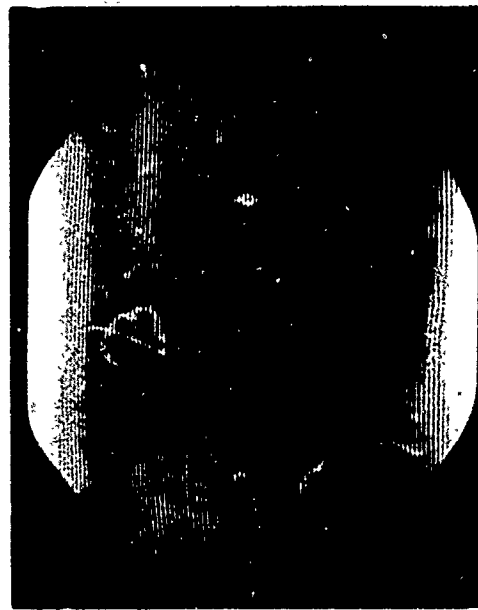
Run	$\Delta K'$	$\Delta K'/K'$	observed $\Delta K'$ (from Fig. 4)
114	$\pm 3.78 \times 10^{-6} \text{ m}^3/\text{kg}$	1.94%	$2.50 \times 10^{-6} \text{ m}^3/\text{kg}$
115	2.47 " "	1.24%	3.20 " "
116	2.15 " "	1.09%	1.52 " "
117	2.79 " "	1.41%	2.60 " "
118	5.40 " "	2.78%	5.74 " "
119	2.95 " "	1.49%	0.93 " "
120	1.84 " "	.958%	2.29 " "
121	3.49 " "	1.81%	1.63 " "
197	1.56 " "	.803%	.21 " "
198	2.02 " "	1.03%	.80 " "
200	3.50 " "	1.77%	.85 " "
201	3.52 " "	1.75%	2.45 " "



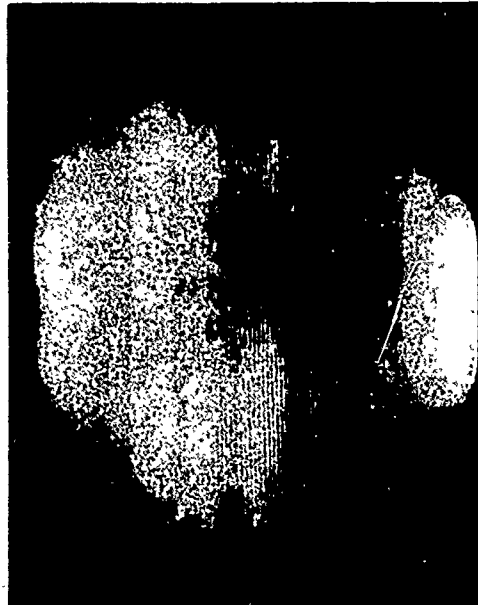
a) No Flow - Monochromatic



b) No Flow - White Light



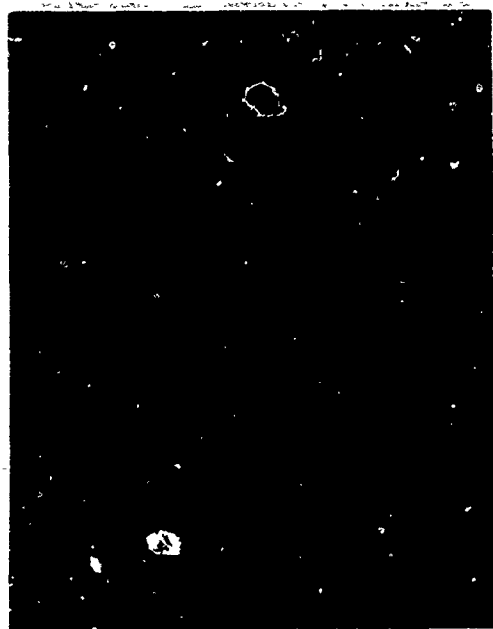
c) Flow - Monochromatic



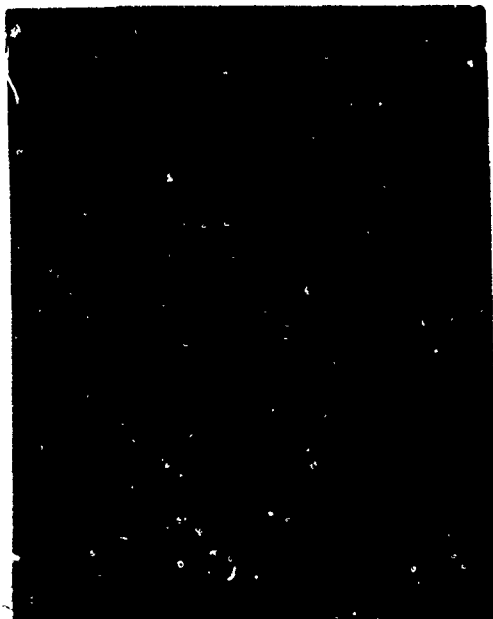
d) Flow - White Light

FIG. 1 - TYPICAL INTERFEROGRAMS TAKEN WITH MAGNESIUM SPARK LIGHT SOURCE - SHOWN APPROXIMATELY 3/4 ACTUAL SIZE

(Run 119:  $M_S = 15.12$ ,  $P_1 = 9.94$  mm.Hg. Oxygen)



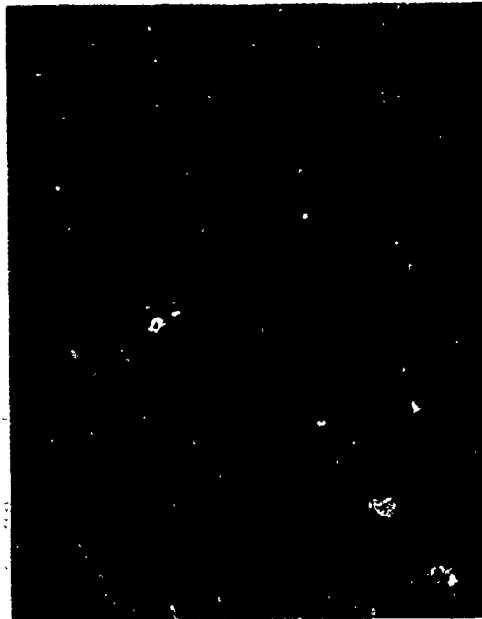
a) No Flow - Monochromatic



b) No Flow - White Light

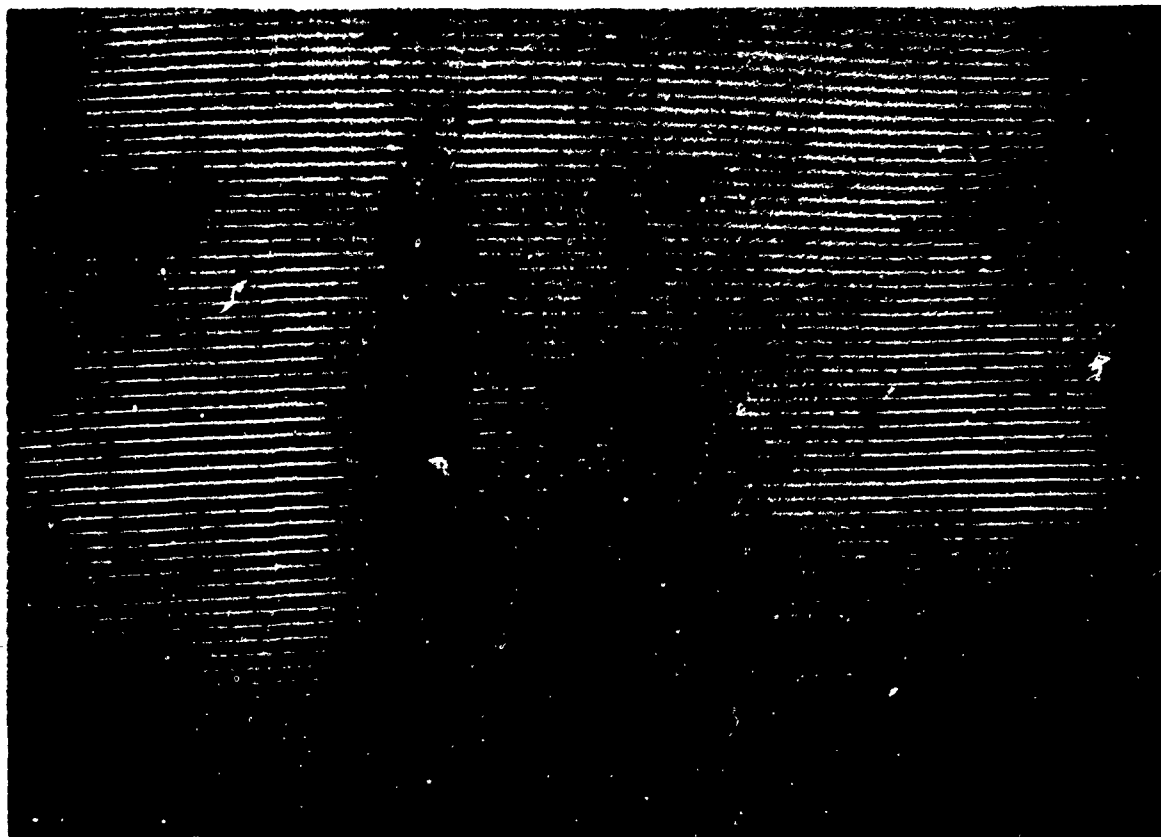


c) Flow - Monochromatic

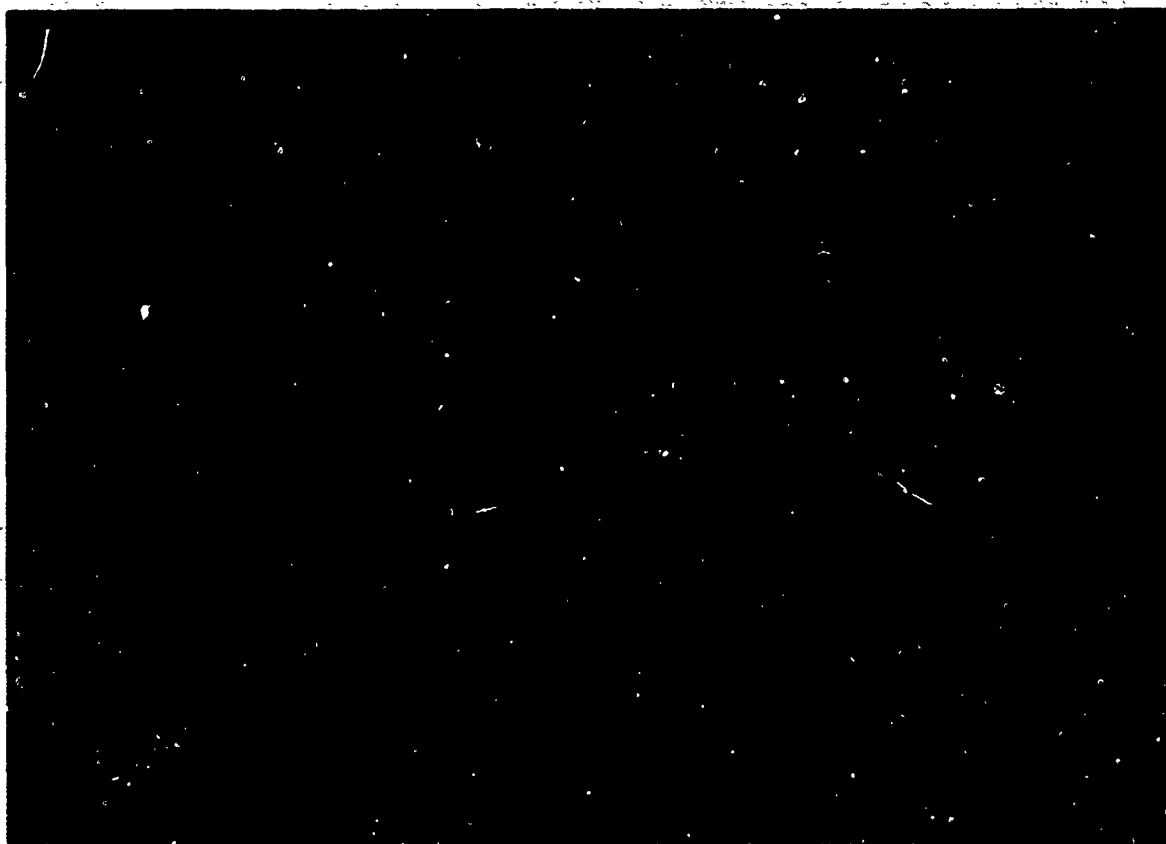


d) Flow - White Light

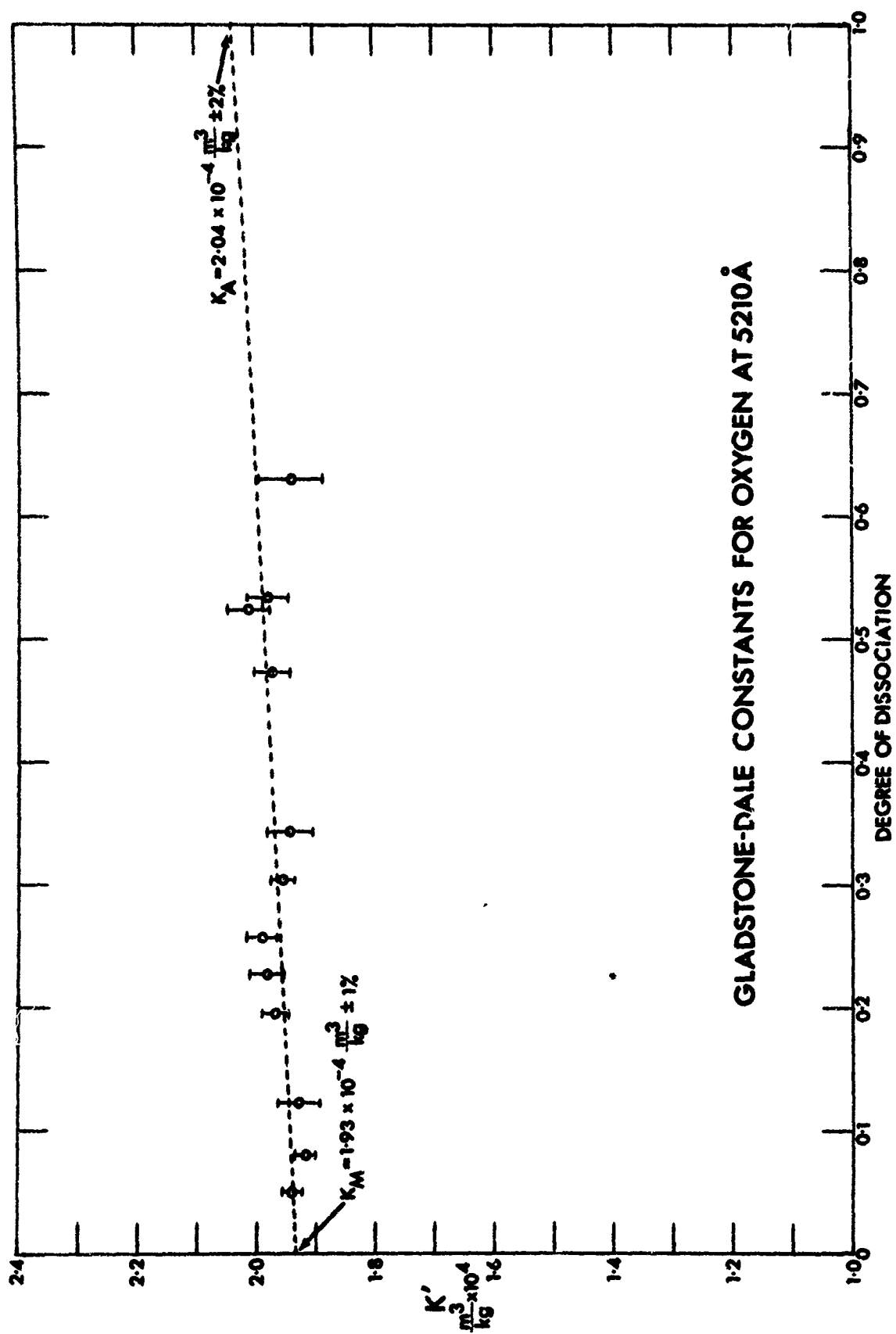
FIG. 2 - TYPICAL INTERFEROGRAMS TAKEN WITH EXPLODING WIRE LIGHT SOURCE - SHOWN APPROXIMATELY 1-1/2 TIMES ACTUAL SIZE  
(Run 200:  $M_S = 15.75$ ,  $P_1 = 7.50$  mm. Hg. Oxygen)



**FIG. 3a - ENLARGEMENT OF MONOCHROMATIC FLOW INTERFEROGRAM  
SHOWN IN FIG. 1 (Approximately twice full size)**



**FIG. 3b - ENLARGEMENT OF MONOCHROMATIC FLOW INTERFEROGRAM  
SHOWN IN FIG. 2 (Approximately four times full size)**



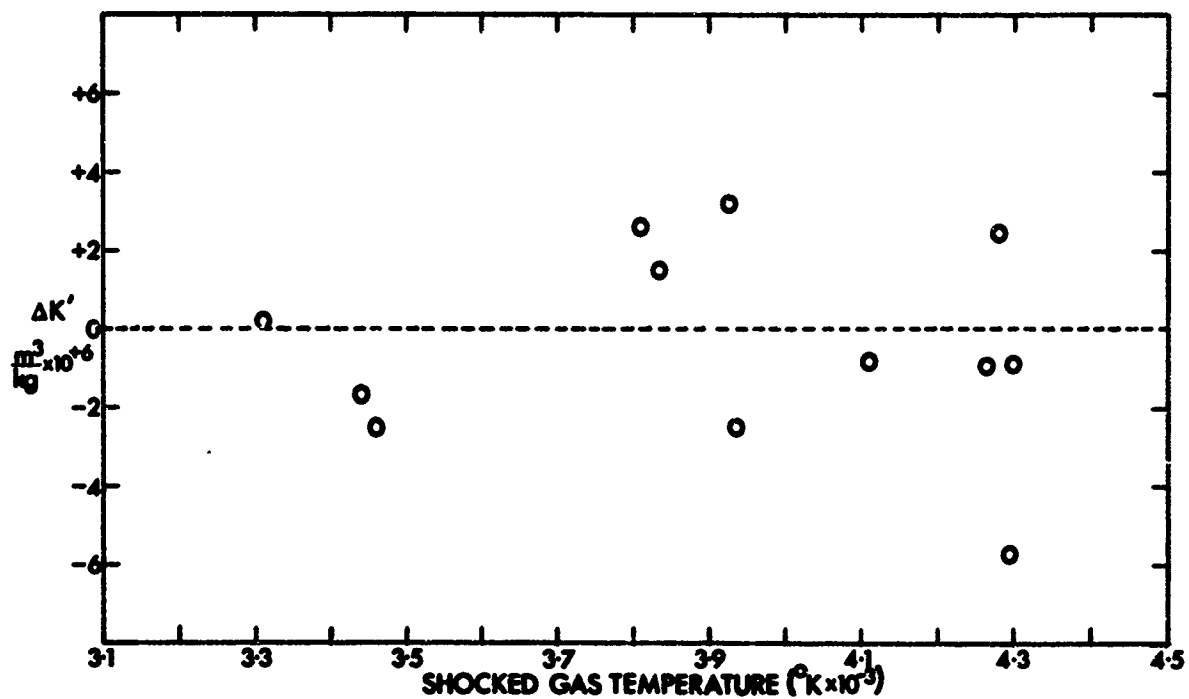


FIG. 5 - VARIATION OF SCATTER IN FIG. 4 WITH SHOCKED GAS TEMPERATURE

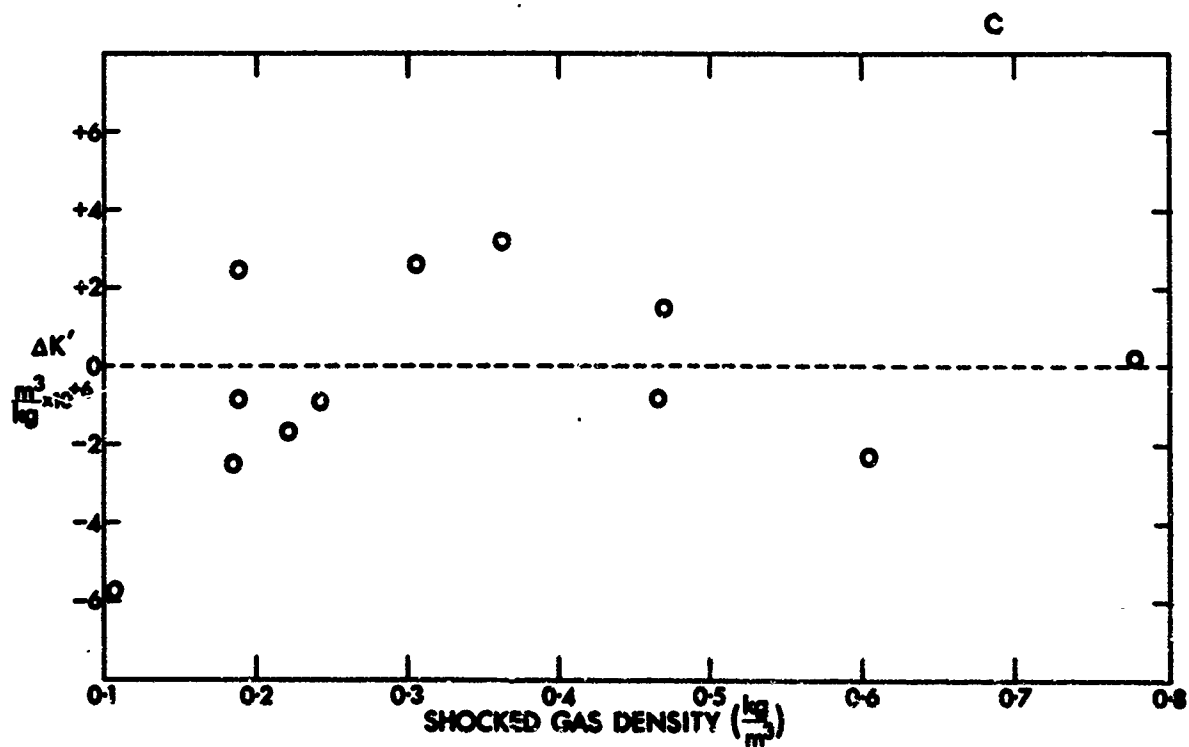


FIG. 6 - VARIATION OF SCATTER IN FIG. 4 WITH SHOCKED GAS DENSITY



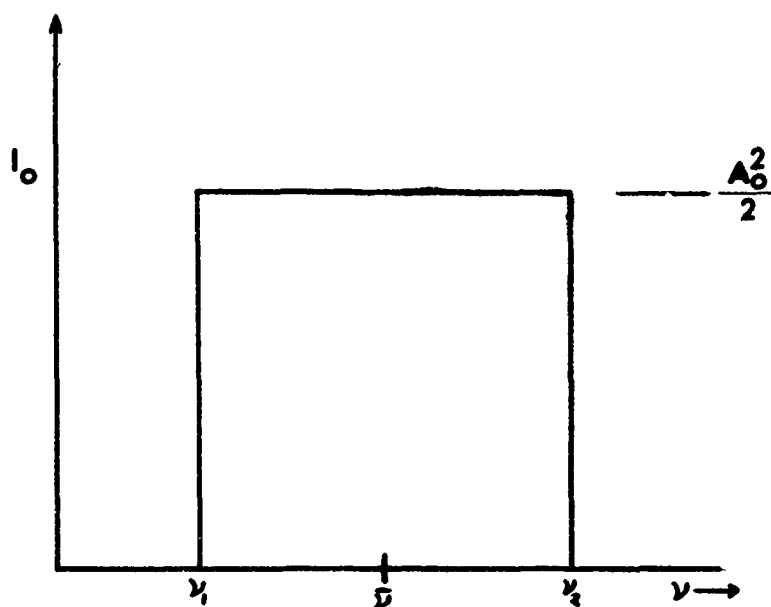


FIG. 9a - SYMMETRIC SPECTRAL INTENSITY DISTRIBUTION

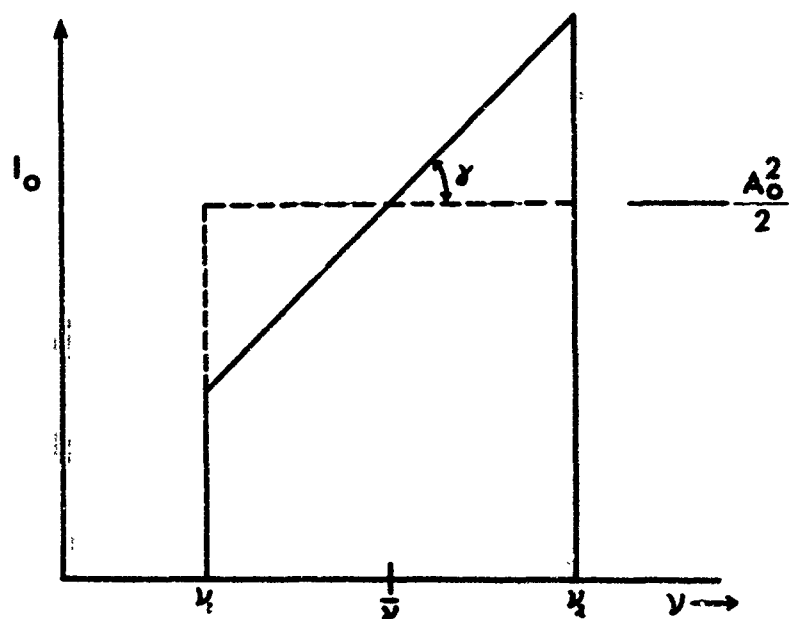


FIG. 9b - ASYMMETRIC SPECTRAL INTENSITY DISTRIBUTION

## APPENDIX A

### Calculation of White-Light Interference Patterns

In this appendix, details of the integration of Eq. 43 leading to Eq. 44 will be given. In addition, the integration will be carried out for the case of an intensity distribution which is weighted toward one end of the frequency spectrum, rather than the symmetrical distribution assumed in Eq. 44. Details will be given of numerical calculations carried out to illustrate the effects noted in the calculations.

The intensity distribution in a white-light interference pattern is given basically by Eq. 43:

$$\int_{\nu_1}^{\nu_2} \bar{I} d\nu = \frac{A_0^2}{2} \int_{\nu_1}^{\nu_2} \cos^2 \left[ \frac{\pi L \nu K}{c} (\rho_2 - \rho_1) - \frac{\nu}{8\pi c} (\omega_p)_2^2 - \frac{2\pi \epsilon \nu n_a}{c} \right] d\nu \quad (43)$$

For simplicity, we substitute:

$$X_1 = \frac{\pi L}{c} ; \quad X_2 = \frac{2\pi \epsilon}{c}$$

As noted in Sec. 2.2.4., the Cauchy relation is introduced in order to provide frequency-dependent expressions for the indices of refraction and the Gladstone-Dale constant. Therefore we write:

$$n_a - 1 = A_a + B_a \nu^2 + C_a \nu^4 + \dots$$

$$K = K_0 + K_2 \nu^2 + K_4 \nu^4 + \dots$$

At this point, it is convenient and instructive to introduce a change of variable. Therefore, let (Ref. 5):

$$\Delta = \nu - \bar{\nu}$$

where:

$$\bar{\nu} = \frac{\nu_2 + \nu_1}{2}$$

Therefore:

$$\nu = \bar{\nu} + \Delta = \bar{\nu} \left( 1 + \frac{\Delta}{\bar{\nu}} \right) ; \quad d\nu = d\Delta$$

When:

$$\nu = \nu_2 ; \quad \Delta = \nu_2 - \bar{\nu} = \frac{\nu_2 - \nu_1}{2}$$

$$\nu = \nu_1 ; \quad \Delta = \nu_1 - \bar{\nu} = -\frac{\nu_2 - \nu_1}{2}$$

We must also rewrite the power series describing the indices of refraction in terms of the new variable. It can be shown that (Ref. 5):

$$\begin{aligned}
n_a &= 1 + A_a + B_a v^2 + C_a v^4 + \dots \\
&= 1 + \Delta'_0 + \Delta'_1 \left(\frac{\Delta}{v}\right) + \Delta'_2 \left(\frac{\Delta}{v}\right)^2 + \Delta'_3 \left(\frac{\Delta}{v}\right)^3 + \dots
\end{aligned}$$

where:

$$\begin{aligned}
\Delta'_0 &= A_a + B_a v^2 + C_a v^4 + D_a v^6 + \dots \\
\Delta'_1 &= 2 B_a v^2 + 4 C_a v^4 + 6 D_a v^6 + \dots \\
\Delta'_2 &= B_a v^2 + 6 C_a v^4 + 15 D_a v^6 + \dots \\
\Delta'_3 &= 4 C_a v^4 + 20 D_a v^6 + \dots
\end{aligned}
\tag{A.1}$$

etc.

Similarly:

$$\begin{aligned}
K &= K_0 + K_2 v^2 + K_4 v^4 + \dots \\
&= \Delta_0 + \Delta_1 \left(\frac{\Delta}{v}\right) + \Delta_2 \left(\frac{\Delta}{v}\right)^2 + \Delta_3 \left(\frac{\Delta}{v}\right)^3 + \dots
\end{aligned}$$

where:

$$\begin{aligned}
\Delta_0 &= K_0 + K_2 v^2 + K_4 v^4 + K_6 v^6 + \dots \\
\Delta_1 &= 2 K_2 v^2 + 4 K_4 v^4 + 6 K_6 v^6 + \dots \\
\Delta_2 &= K_2 v^2 + 6 K_4 v^4 + 15 K_6 v^6 + \dots \\
\Delta_3 &= 4 K_4 v^4 + 20 K_6 v^6 + \dots
\end{aligned}
\tag{A.2}$$

etc.

Likewise, the term in Eq. 43 which gives the contribution of the electrons must be rewritten:

$$\begin{aligned}
\frac{L(\omega_p)_2^2}{8\pi v c} &= \frac{L(\omega_p)_2^2}{8\pi c v} \left(1 + \frac{\Delta}{v}\right)^{-1} \\
&= \frac{L(\omega_p)_2^2}{8\pi c v} \left(1 - \frac{\Delta}{v} + \left(\frac{\Delta}{v}\right)^2 - \dots\right) \\
&= X_3 v \left(1 - \frac{\Delta}{v} + \left(\frac{\Delta}{v}\right)^2 - \dots\right)
\end{aligned}
\tag{A.3}$$

where:

$$X_3 = \frac{L(\omega_p)_2^2}{8\pi c v^2} = \frac{L e^2 N_e}{8\pi c v^2 \epsilon_0 m_e}$$

Therefore, Eq. 43 becomes finally:

$$\int_{-\frac{v_2-v_1}{2}}^{+\frac{v_2-v_1}{2}} \bar{I} d\Delta = \frac{A_0^2}{2} \int_{-\frac{v_2-v_1}{2}}^{+\frac{v_2-v_1}{2}} \cos^2 \left\{ X_1 \bar{v}(\rho_2-\rho_1) \left( \Delta_0 + \Delta_1 \left( \frac{\Delta}{\bar{v}} \right) + \dots \right) \left( 1 + \frac{\Delta}{\bar{v}} \right) \right. \\ \left. - X_2 \bar{v} y (1 + \Delta'_0 + \Delta'_1 \left( \frac{\Delta}{\bar{v}} \right) + \dots) \left( 1 + \frac{\Delta}{\bar{v}} \right) \right. \\ \left. - X_3 \bar{v} \left( 1 - \frac{\Delta}{\bar{v}} + \left( \frac{\Delta}{\bar{v}} \right)^2 + \dots \right) \right\} d\Delta$$

Dropping all terms of second and higher order, we obtain:

$$\int_{-\frac{v_2-v_1}{2}}^{+\frac{v_2-v_1}{2}} \bar{I} d\Delta = \frac{A_0^2}{2} \int_{-\frac{v_2-v_1}{2}}^{+\frac{v_2-v_1}{2}} \cos^2 \left\{ X_1 \bar{v}(\rho_2-\rho_1) \left[ \Delta_0 + (\Delta_0 + \Delta_1) \frac{\Delta}{\bar{v}} \right] \right. \\ \left. - X_2 \bar{v} y \left[ 1 + \Delta'_0 + (1 + \Delta'_0 + \Delta'_1) \frac{\Delta}{\bar{v}} \right] - X_3 \bar{v} \left( 1 - \frac{\Delta}{\bar{v}} \right) \right\} d\Delta \quad (A.4)$$

This expression is of the form:

$$\int \cos^2(M + Nx) dx = \frac{1}{2} \int \cos 2(M + Nx) dx + \frac{1}{2} \int dx \\ = \frac{1}{4N} \sin 2(M + Nx) + \frac{x}{2}$$

Thus, Eq. A.4 becomes

$$\bar{I}(v_2-v_1) = \frac{A_0^2}{2} \frac{1}{4} \frac{1}{[X_1(\rho_2-\rho_1)(\Delta_0+\Delta_1) - X_2 y (1+\Delta'_0+\Delta'_1) + X_3]} \left[ \sin \left\{ 2X_1(\rho_2-\rho_1) \left[ \Delta_0 \bar{v} \right. \right. \right. \\ \left. \left. + (\Delta_0+\Delta_1) \left( \frac{v_2-v_1}{2} \right) \right] - 2X_2 y \left[ \bar{v} + \Delta'_0 \bar{v} + (1+\Delta'_0+\Delta'_1) \left( \frac{v_2-v_1}{2} \right) \right] - 2X_3 \bar{v} + 2X_3 \left( \frac{v_2-v_1}{2} \right) \right\} \right. \\ \left. - \sin \left\{ 2X_1(\rho_2-\rho_1) \left[ \Delta_0 \bar{v} - (\Delta_0+\Delta_1) \left( \frac{v_2-v_1}{2} \right) \right] - 2X_2 y \left[ \bar{v} + \Delta'_0 \bar{v} - (1+\Delta'_0+\Delta'_1) \left( \frac{v_2-v_1}{2} \right) \right] \right. \right. \\ \left. \left. - 2X_3 \bar{v} - 2X_3 \left( \frac{v_2-v_1}{2} \right) \right\} \right] + \frac{A_0^2}{4} (v_2-v_1) \quad (A.5)$$

or

$$\bar{I}(v_2-v_1) = \frac{A_0^2}{4} (v_2-v_1) \left\{ 1 + \frac{\sin \{ [X_1(\rho_2-\rho_1)(\Delta_0+\Delta_1) - X_2 y (1+\Delta'_0+\Delta'_1) + X_3] (v_2-v_1) \}}{[X_1(\rho_2-\rho_1)(\Delta_0+\Delta_1) - X_2 y (1+\Delta'_0+\Delta'_1) + X_3] (v_2-v_1)} \right. \\ \left. \times \cos \{ 2 [X_1(\rho_2-\rho_1) \Delta_0 - X_2 y (1 + \Delta'_0) - X_3] \bar{v} \} \right\} \quad (A.6)$$

where Eq. A.6 is the same as Eq. 44 in Sec. 2.2.4.

As noted in Sec. 2.2.4, the phenomenon of "rollover" occurs because the argument of the sine contains factors  $(\Delta_0+\Delta_1)$  and  $(1 + \Delta'_0 + \Delta'_1)$ , while the

corresponding factors in the argument of the cosine are  $\Delta_0$  and  $(1 + \Delta'_0)$ . It is noted, however, that the effect is caused not so much by the fact that  $\Delta_0 \neq \Delta_0 + \Delta_1$ , and  $(1 + \Delta'_0) \neq (1 + \Delta'_0 + \Delta'_1)$ , but by the fact that:

$$\frac{\Delta_0}{\Delta_0 + \Delta_1} \neq \frac{1 + \Delta'_0}{1 + \Delta'_0 + \Delta'_1} \quad (\text{A.7})$$

where it has been assumed, as before, that the electron number density, i.e.,  $N_3$ , is zero.

To show the significance of these quantities, the group index of refraction,  $n_g$ , must be introduced, where:

$$n_g = \frac{c}{v_g}$$

and

$$v_g = \frac{d\omega}{dk} = \left( \frac{dk}{d\omega} \right)^{-1} \quad (\text{A.8})$$

by definition. Noting that:

$$k = \frac{2\pi}{\lambda} = \frac{2\pi\nu}{v_p}; \quad dk = 2\pi d\left(\frac{\nu}{v_p}\right); \quad \omega = 2\pi\nu; \quad d\omega = 2\pi d\nu$$

Eq. A.8 becomes:

$$\begin{aligned} v_g &= \left[ \frac{2\pi}{2\pi} \frac{d\left(\frac{\nu}{v_p}\right)}{d\nu} \right]^{-1} \\ &= \left[ \frac{1}{v_p} - \frac{\nu}{v_p^2} \left( \frac{dv_p}{d\nu} \right) \right]^{-1} \\ &= v_p \left[ 1 - \frac{\nu}{v_p} \left( \frac{dv_p}{d\nu} \right) \right]^{-1} \end{aligned}$$

Now:

$$v_p = \frac{c}{n_p}; \quad dv_p = - \frac{c}{n_p^2} dn_p$$

so that:

$$\begin{aligned} n_g &= \frac{c}{v_g} \\ &= \frac{c}{v_p} \left[ 1 - \frac{\nu}{v_p} \left( \frac{dv_p}{d\nu} \right) \right]^{-1} = n_p - \frac{c\nu}{v_p^2} \frac{dv_p}{d\nu} \\ &= n_p + \nu \frac{dn_p}{d\nu} \end{aligned} \quad (\text{A.9})$$

and at frequency  $\bar{\nu}$ :

$$n_g = n_p + \bar{\nu} \frac{dn_p}{d\bar{\nu}} \quad (\text{A.9a})$$

It

Now, from the Cauchy relation:

$$n_{pa} = 1 + A_a + B_a \bar{v}^2 + C_a \bar{v}^4 + \dots \quad (A.10)$$

(A.7)

one obtains by differentiation:

$$\frac{d n_{pa}}{d \bar{v}} = 2 B_a \bar{v} + 4 C_a \bar{v}^3$$

of

so that by substituting in Eq. A.9a, one obtains:

$$\begin{aligned} n_{ga} &= 1 + A_a + B_a \bar{v}^2 + C_a \bar{v}^4 + \dots + 2B_a \bar{v}^2 + 4 C_a \bar{v}^4 \\ &= 1 + A_a + 3B_a \bar{v}^2 + 5 C_a \bar{v}^4 + \dots \end{aligned} \quad (A.11)$$

(A.8)

Going back to Eq. A.1, it is seen that:

$$1 + \Delta'_0 = 1 + A_a + B_a \bar{v}^2 + C_a \bar{v}^4 + \dots$$

and

$$1 + \Delta'_0 + \Delta'_1 = 1 + A_a + 3B_a \bar{v}^2 + 5 C_a \bar{v}^4 + \dots$$

Thus, it is seen that to use  $(1 + \Delta'_0)$  is to use the phase index of refraction, and to use  $(1 + \Delta'_0 + \Delta'_1)$  is to use the group index of refraction.

To obtain, the significance of  $\Delta_0$  and  $(\Delta_0 + \Delta_1)$ , one must go back to the definition of the Gladstone-Dale constant. Again neglecting the electrons, we obtain:

$$K = \frac{n-1}{\rho_0}$$

where  $\rho_0$  is the density at which  $n$  is measured. Thus we may write:

$$K = K_0 + K_2 \bar{v}^2 + K_4 \bar{v}^4 + \dots = \frac{1}{\rho_0} (A_t + B_t \bar{v}^2 + C_t \bar{v}^4 + \dots)$$

so that:

$$K_0 = \frac{A_t}{\rho_0}$$

$$K_2 = \frac{B_t}{\rho_0}$$

$$K_4 = \frac{C_t}{\rho_0}$$

etc.

(A.9)

and going back to Eq. A.2, it is seen that:

(A.9a)

$$\begin{aligned} \Delta_0 &= K_0 + K_2 \bar{v}^2 + K_4 \bar{v}^4 + \dots \\ &= \frac{A_t}{\rho_0} + \frac{B_t}{\rho_0} \bar{v}^2 + \frac{C_t}{\rho_0} \bar{v}^4 + \dots = \frac{n_{pt} - 1}{\rho_0} \end{aligned}$$

and:

$$\begin{aligned}\Delta_0 + \Delta_1 &= K_0 + 3 K_2 \bar{\nu}^2 + 5 K_4 \bar{\nu}^4 + \dots \\ &= \frac{A_t}{\rho_0} + 3 \frac{B_t}{\rho_0} \bar{\nu}^2 + 5 \frac{C_t}{\rho_0} \bar{\nu}^4 + \dots = \frac{n_{gt} - 1}{\rho_0}\end{aligned}$$

Therefore, it is seen that to use  $\Delta_0$  is to use the Gladstone-Dale constant based on phase index of refraction, and to use  $(\Delta_0 + \Delta_1)$ , is to use the Gladstone-Dale constant based on group index of refraction. Thus, substituting in Eq. A.7, it is found that:

$$\begin{aligned}\frac{\frac{A_t}{\rho_0} + \frac{B_t}{\rho_0} \bar{\nu}^2 + \frac{C_t}{\rho_0} \bar{\nu}^4 + \dots}{\frac{A_t}{\rho_0} + 3 \frac{B_t}{\rho_0} \bar{\nu}^2 + 5 \frac{C_t}{\rho_0} \bar{\nu}^4 + \dots} &\neq \frac{1 + A_a + B_a \bar{\nu}^2 + C_a \bar{\nu}^4 + \dots}{1 + A_a + 3B_a \bar{\nu}^2 + 5 C_a \bar{\nu}^4 + \dots} \\ 1 - \frac{2B_t \bar{\nu}^2 + 4 C_t \bar{\nu}^4 + \dots}{A_t + 3B_t \bar{\nu}^2 + 5 C_t \bar{\nu}^4 + \dots} &\neq 1 - \frac{2 B_a \bar{\nu}^2 + 4 C_a \bar{\nu}^4 + \dots}{1 + A_a + 3B_a \bar{\nu}^2 + 5 C_a \bar{\nu}^4 + \dots}\end{aligned}$$

or:

$$\begin{aligned}A_t + B_t \bar{\nu}^2 + C_t \bar{\nu}^4 + \dots + 2 B_t \bar{\nu}^2 + 4 C_t \bar{\nu}^4 + \dots \\ \neq 1 + A_a + B_a \bar{\nu}^2 + C_a \bar{\nu}^4 + \dots + 2 B_a \bar{\nu}^2 + 4 C_a \bar{\nu}^4 + \dots\end{aligned}$$

where we have assumed, for the purpose of illustration, that

$$A_a = A_t; \quad B_a = B_t; \quad C_a = C_t; \text{ etc.}$$

Thus it can now be seen why rollover occurs; it is because  $(1 + \Delta'_0)$  is of the form  $n_p$ , a number of order one, and  $\Delta_0$  is of the form  $(n_p - 1)$ . To both these quantities is added an amount  $\Delta_1$  (or  $\Delta'_1$ ) which is a number of approximately the same order as  $\Delta_0$  or  $\Delta'_0$ , and  $\Delta_1$  forms a much greater part of  $(\Delta_0 + \Delta_1)$  than  $\Delta'_1$  forms of  $(1 + \Delta'_0 + \Delta'_1)$  so that the ratio  $\Delta_0 / (\Delta_0 + \Delta_1)$  is much less than the ratio  $1 + \Delta'_0 / (1 + \Delta'_0 + \Delta'_1)$ . Thus, in effect, rollover occurs because the Gladstone-Dale constant and the index of refraction are different quantities, varying in different ways with frequency. However, rollover is still basically a dispersive effect, since, there was no dispersion,  $\Delta_1$  and  $\Delta'_1$  would be identically zero.

Using the data in Ref. 6 for the index of refraction of air and the Gladstone-Dale constants for oxygen, one finds that, on fitting a Cauchy relation:

$$\begin{aligned}K_{O_2} &= (1.843 \times 10^{-4} + 1.773 \times 10^{-35} \nu^2) \frac{m^3}{kg} \\ n_{p,air} &= 1 + 1.795 \times 10^{-5} + 1.215 \times 10^{-36} \nu^2\end{aligned}$$

Then, on calculating the quantities in Eq. A.6, one finds that, at 5200 Å

$$\begin{aligned}\Delta_0 &= 1.902 \times 10^{-4} \frac{m^3}{kg} \\ \Delta_1 &= .1174 \times 10^{-4} \frac{m^3}{kg}\end{aligned}$$

$$\Delta'_0 = 1.835 \times 10^{-5}$$

$$\Delta'_1 = .0804 \times 10^{-5}$$

Thus it is seen that  $\Delta'_1$  can be neglected in relation to  $(1 + \Delta'_0)$ , since  $\Delta'_1$  is of the order of  $10^{-6}$ , while  $(1 + \Delta'_0)$  is of order unity. However, it is seen that  $\Delta_1$  is definitely not negligible with respect to  $\Delta_0$ , and this then leads to rollover, as described above.

It is instructive, on the basis of the above data, to calculate the fringe shift required for a rollover of one fringe to occur, i.e., for the maximum of the fringe envelope to move with respect to the zero-order fringe by an amount equal to the spacing of individual fringes, so that the maximum of the fringe envelope coincides with the first-order fringe, rather than the zero-order fringe.

Let  $y$  now be the monochromatic fringe shift at which a rollover of one occurs. Since a particular fringe is characterized by a particular value of the argument of the cosine in Eq. A.6, we may write, for the zero-order fringe in particular:

$$2 [X_1(\rho_2 - \rho_1) \Delta_0 - X_2 y (1 + \Delta'_0)] \bar{v} = 0 \quad (A.12)$$

where we have neglected electrons. Substituting for  $X_1$  and  $X_2$ , and putting:

$$\frac{\bar{v}}{c} = \frac{1}{\lambda_0}$$

we obtain

$$\frac{\pi L}{\lambda_0} (\rho_2 - \rho_1) \Delta_0 - \frac{2\pi \epsilon y}{\lambda} (1 + \Delta'_0) = 0 \quad (A.13)$$

Earlier it was found that  $(1 + \Delta'_0)$  was equivalent to the phase index of refraction  $n_{pa}$ . Also from Sec. 2.2.3, it was found that the spacing of individual fringes is given by:

$$d = \frac{\lambda_0}{2\epsilon n_{pa}}$$

Thus, Eq. A.13 becomes:

$$\frac{L}{\lambda_0} (\rho_2 - \rho_1) \Delta_0 - \frac{y}{d} = 0 \quad (A.14)$$

A similar procedure can be carried out with the argument of the sine in Eq. A.6, which gives the position of the fringe envelope. However, since a rollover of one fringe has occurred, the position of the maximum of the envelope is at position  $(y + d)$ . Therefore:

$$[X_1(\rho_2 - \rho_1)(\Delta_0 + \Delta_1) - X_2(y + d)(1 + \Delta'_0)] (v_2 - v_1) = 0$$

where  $\Delta'_1$  has been neglected, in line with the order analysis carried out above. Proceeding as before, one obtains:

$$\frac{L}{\lambda_0} (\rho_2 - \rho_1)(\Delta_0 + \Delta_1) - \frac{y+d}{d} = 0 \quad (A.15)$$

Then, on eliminating  $\frac{L}{\lambda_0} (\rho_2 - \rho_1)$  between Eqs. A.14 and A.15, one obtains:

$$\left(\frac{y+d}{d}\right)\Delta_0 = \frac{y}{d} (\Delta_0 + \Delta_1)$$

whence:

$$\frac{y}{d} = \frac{\Delta_0}{\Delta_1} \quad (A.16)$$

Thus, using the data given earlier for  $\Delta_0$  and  $\Delta_1$ , it is found that, in oxygen, a rollover of one fringe occurs when the monochromatic fringe shift is about sixteen fringes. This agrees very well with experimentally observed rollover in the oxygen work.

If a similar determination of  $\Delta_0$  and  $\Delta_1$  is carried out for argon, one finds that a rollover of one fringe occurs when the monochromatic fringe shift is about 23 fringes.

## A.2 White Light Interference with an Asymmetric Intensity Distribution

So far we have considered only an intensity distribution which is symmetric about  $\nabla$ . We now investigate the effect of an asymmetric distribution of intensity, i.e., an intensity distribution with wavelength which is weighted toward one end of the wavelength range, which is the more usual state of affairs. The intensity distribution in a beam of white light, as seen by the detector, is a function of many parameters: the spectral content of the source light, the transmissions and reflectivities of the interferometer optics, the transmissions and reflectivities of all the other mirrors and lenses in the system, as well as the spectral response of the detector itself, used to record the interference pattern. Thus, a symmetric intensity distribution, such as was considered above, would be rare.

Thus, referring to Fig. 9b, we assume an intensity distribution with wavelength of the form:

$$I_0 = \frac{A_0^2}{2} \left[ 1 + \frac{\gamma \Delta}{\nu_2 - \nu_1} \right] \quad \text{for } -\frac{\nu_2 - \nu_1}{2} < \Delta < +\frac{\nu_2 - \nu_1}{2}$$

$$I_0 = 0 \quad \text{for } \Delta < -\frac{\nu_2 - \nu_1}{2} \quad \text{and} \quad \Delta > +\frac{\nu_2 - \nu_1}{2}$$

In this expression, it is noted that  $\gamma$  is a parameter which denotes the degree of asymmetry of the intensity distribution, and  $\Delta$  is the quantity introduced earlier which varies with frequency.  $\tan^{-1} \gamma$  is, in effect, the slope of the top of the intensity with frequency distribution and it is seen that when  $\gamma = 0$ , this intensity distribution degenerates to the symmetric distribution considered earlier.

The expression for the intensity distribution in the white-light interferogram then becomes, as in Eq. A.4:

$$\begin{aligned}
\int_{-\frac{v_2-v_1}{2}}^{+\frac{v_2-v_1}{2}} \bar{I} \, d\Delta = & \frac{A_0^2}{2} \int_{-\frac{v_2-v_1}{2}}^{+\frac{v_2-v_1}{2}} \cos^2 \left\{ X_1 \bar{v}(\rho_2-\rho_1) \left[ \Delta_0 + (\Delta_0+\Delta_1)\frac{\Delta}{\bar{v}} \right] \right. \\
& \left. - X_2 \bar{v}_y \left[ 1 + \Delta'_0 + (1 + \Delta'_0 + \Delta'_1)\frac{\Delta}{\bar{v}} \right] - X_3 \bar{v} \left( 1 - \frac{\Delta}{\bar{v}} \right) \right\} d\Delta \\
+ \frac{A_0^2}{2} \frac{\gamma}{v_2-v_1} \int_{-\frac{v_2-v_1}{2}}^{+\frac{v_2-v_1}{2}} \Delta \cos^2 & \left\{ X_1 \bar{v}(\rho_2-\rho_1) \left[ \Delta_0 + (\Delta_0+\Delta_1)\frac{\Delta}{\bar{v}} \right] \right. \\
& \left. - X_2 \bar{v}_y \left[ 1 + \Delta'_0 + (1 + \Delta'_0 + \Delta'_1)\frac{\Delta}{\bar{v}} \right] - X_3 \bar{v} \left( 1 - \frac{\Delta}{\bar{v}} \right) \right\} d\Delta
\end{aligned} \tag{A.17}$$

The result of the first integration is identical to that obtained before for the symmetric intensity distribution, and the result is given in Eq. A.6. The second integral is of the form:

$$\begin{aligned}
\int x \cos^2 (M + Nx) \, dx = & \frac{1}{4N} \left[ x \sin 2 (M + Nx) \right] \\
& + \frac{1}{8N^2} \left[ \cos 2 (M + Nx) \right] + \frac{x^2}{4}
\end{aligned}$$

Therefore, the second integral becomes:

$$\begin{aligned}
& \frac{A_0^2}{2} \frac{\gamma}{v_2-v_1} \frac{1}{4} \frac{1}{X_1(\rho_2-\rho_1)(\Delta_0+\Delta_1) - X_2 y(1+\Delta'_0+\Delta'_1) + X_3} \left[ \frac{v_2-v_1}{2} \sin \left\{ 2X_1(\rho_2-\rho_1) \right. \right. \\
& \cdot \left[ \Delta_0 \bar{v} + (\Delta_0+\Delta_1) \left( \frac{v_2-v_1}{2} \right) \right] - 2X_2 y \left[ \bar{v} + \Delta'_0 \bar{v} + (1+\Delta'_0+\Delta'_1) \left( \frac{v_2-v_1}{2} \right) \right] - 2X_3 \bar{v} + 2X_3 \left( \frac{v_2-v_1}{2} \right) \right\} \\
& + \frac{v_2-v_1}{2} \sin \left\{ 2X_1(\rho_2-\rho_1) \left[ \Delta_0 \bar{v} - (\Delta_0+\Delta_1) \left( \frac{v_2-v_1}{2} \right) \right] - 2X_2 y \left[ \bar{v} + \Delta'_0 \bar{v} - (1+\Delta'_0+\Delta'_1) \left( \frac{v_2-v_1}{2} \right) \right] \right. \\
& \left. \left. - 2X_3 \bar{v} - 2X_3 \left( \frac{v_2-v_1}{2} \right) \right] \right\} \\
& + \frac{A_0^2}{2} \frac{\gamma}{v_2-v_1} \frac{1}{8} \left( \frac{1}{X_1(\rho_2-\rho_1)(\Delta_0+\Delta_1) - X_2 y(1+\Delta'_0+\Delta'_1) + X_3} \right)^2 \left[ \cos \left\{ 2X_1(\rho_2-\rho_1) \left[ \Delta_0 \bar{v} \right. \right. \right. \\
& + (\Delta_0+\Delta_1) \left( \frac{v_2-v_1}{2} \right) \right] - 2X_2 y \left[ \bar{v} + \Delta'_0 \bar{v} + (1+\Delta'_0+\Delta'_1) \left( \frac{v_2-v_1}{2} \right) \right] - 2X_3 \bar{v} + 2X_3 \left( \frac{v_2-v_1}{2} \right) \right\} \\
& - \cos \left\{ 2X_1(\rho_2-\rho_1) \left[ \Delta_0 \bar{v} - (\Delta_0+\Delta_1) \left( \frac{v_2-v_1}{2} \right) \right] - 2X_2 y \left[ \bar{v} + \Delta'_0 \bar{v} - (1+\Delta'_0+\Delta'_1) \left( \frac{v_2-v_1}{2} \right) \right] \right. \\
& \left. \left. - 2X_3 \bar{v} - 2X_3 \left( \frac{v_2-v_1}{2} \right) \right] \right\} + \frac{A_0^2}{2} \frac{\gamma}{v_2-v_1} \cdot \frac{1}{4} \left[ \left( \frac{v_2-v_1}{2} \right)^2 - \left( -\frac{v_2-v_1}{2} \right)^2 \right]
\end{aligned}$$

$$\begin{aligned}
&= \frac{A_0^2}{2} \frac{\gamma}{v_2 - v_1} \cdot \frac{1}{2} \cdot \frac{v_2 - v_1}{2} \cdot \frac{\cos\{[X_1(\rho_2 - \rho_1)(\Delta_0 + \Delta_1) - X_2y(1 + \Delta'_0 + \Delta'_1) + X_3](v_2 - v_1)\}}{X_1(\rho_2 - \rho_1)(\Delta_0 + \Delta_1) - X_2y(1 + \Delta'_0 + \Delta'_1) + X_3} \\
&\quad \times \sin\{2[X_1(\rho_2 - \rho_1)\Delta_0 - X_2y(1 + \Delta'_0) - X_3]\bar{v}\} \\
&- \frac{A_0^2}{2} \cdot \frac{\gamma}{v_2 - v_1} \cdot \frac{1}{4} \frac{\sin\{[X_1(\rho_2 - \rho_1)(\Delta_0 + \Delta_1) - X_2y(1 + \Delta'_0 + \Delta'_1) + X_3](v_2 - v_1)\}}{[X_1(\rho_2 - \rho_1)(\Delta_0 + \Delta_1) - X_2y(1 + \Delta'_0 + \Delta'_1) + X_3]^2} \\
&\quad \times \sin\{2[X_1(\rho_2 - \rho_1)\Delta_0 - X_2y(1 + \Delta'_0) - X_3]\bar{v}\}
\end{aligned} \tag{A.18}$$

Thus, the complete expression for the intensity distribution in a white light interference pattern is the sum of Eqs. A.6 and A.18, which is

$$\begin{aligned}
\bar{I}(v_2 - v_1) &= \frac{A_0^2}{4} (v_2 - v_1) \left[ 1 + \frac{\sin\{[X_1(\rho_2 - \rho_1)(\Delta_0 + \Delta_1) - X_2y(1 + \Delta'_0 + \Delta'_1) + X_3](v_2 - v_1)\}}{X_1(\rho_2 - \rho_1)(\Delta_0 + \Delta_1) - X_2y(1 + \Delta'_0 + \Delta'_1) + X_3} (v_2 - v_1) \right. \\
&\quad \times \cos\{2[X_1(\rho_2 - \rho_1)\Delta_0 - X_2y(1 + \Delta'_0) - X_3]\bar{v}\} \Big] \\
&+ \frac{A_0^2}{4} \frac{\gamma}{2} (v_2 - v_1) \left[ \frac{\cos\{[X_1(\rho_2 - \rho_1)(\Delta_0 + \Delta_1) - X_2y(1 + \Delta'_0 + \Delta'_1) + X_3](v_2 - v_1)\}}{[X_1(\rho_2 - \rho_1)(\Delta_0 + \Delta_1) - X_2y(1 + \Delta'_0 + \Delta'_1) + X_3](v_2 - v_1)} \right. \\
&\quad \left. - \frac{\sin\{[X_1(\rho_2 - \rho_1)(\Delta_0 + \Delta_1) - X_2y(1 + \Delta'_0 + \Delta'_1) + X_3](v_2 - v_1)\}}{[X_1(\rho_2 - \rho_1)(\Delta_0 + \Delta_1) - X_2y(1 + \Delta'_0 + \Delta'_1) + X_3]^2 (v_2 - v_1)^2} \right] \sin\{2[X_1(\rho_2 - \rho_1)\Delta_0 \\
&\quad - X_2y(1 + \Delta'_0) - X_3]\bar{v}\}
\end{aligned} \tag{A.19}$$

Interpretation of Eq. A.19 is very difficult to do by inspection, since two terms are involved which vary in different ways with wavelength. However, it is noted that Eq. A.19 reduces to Eq. A.6 when  $\gamma = 0$ .

### A.3 Numerical Calculations

To illustrate rollover, the effect of electrons, and the effect of an asymmetric spectral intensity distribution, Eqs. A.6 and A.19 were programmed for the University of Toronto IBM 7094 computer, and white-light interference patterns were calculated for several different cases to illustrate the effects mentioned above. The conditions in the final state in the test-section were assumed to be those produced by a Mach 12.0 shock wave travelling into argon at an initial pressure of 21.0 mm Hg. This produced a density change  $(\rho_2 - \rho_1)$  of about .175 kg/m<sup>3</sup> and gave rise to about 3.3% ionization, i.e., an electron number density of approximately  $3.3 \times 10^{23}/\text{m}^3$ . All the cases were calculated using available room-temperature data for the Gladstone-Dale constants, and it was assumed that the Gladstone-Dale constant for the argon ion was equal to that for the argon atom. This was done partly for simplicity (since these examples were illustrative only) and partly because the dispersion relation for the refractive index of the ion (i.e., the variation of  $K_{A+}$  with  $\nu$ ) was unknown.

The light from the source which produced the interference pattern was taken to have a range of wavelengths from about 4400 Å to 5700 Å, with a mean wavelength,  $\bar{\lambda}$ , of 4960 Å. For the case of  $\gamma = 0$ , the intensity  $I_0$  (see Fig. 9a) was evenly distributed within the above range; for the case of the asymmetric spectral intensity distribution,  $\gamma$  was set equal to +1.0 (see Fig. 9b), so that the intensity,  $I_0$ , at  $\nu_1$ , was  $A_0^2/4$ , and at  $\nu_2$ ,  $I_0$  was  $3A_0^2/4$ , so that the distribution was weighted toward high frequencies, or short wavelengths.

We consider first plots of Eq. A.6, i.e.,  $\gamma = 0$ , so that a spectral intensity distribution which is symmetrical about  $\bar{\nu}$  is being considered.

Figure A.1a shows the intensity distribution of a white-light interferogram with test section and compensating chamber conditions exactly equal, i.e.,  $(\rho_2 - \rho_1) = 0$  and  $X_3 = 0$ . It is noted that the pattern is symmetric about the position of the zero-order fringe, which, in this case, falls at  $y = 0$ , as shown. Of particular note is the phase inversion which occurs between the central fringe group and the subsidiary fringe groups on either side. This is shown in Fig. A.1a, where the order of the fringes has been noted. It is seen that the position of the 4th, 5th, 6th and 7th order fringes fall on minima in the subsidiary fringe groups rather than on maxima. Thus, if one wished to measure fringe spacing using a fringe in the central fringe group and a fringe in the subsidiary fringe group, one would have to measure from a maximum in the central group to a minimum in the subsidiary group, or vice-versa, in order to measure over an integral number of fringes. It would also appear that to measure fringe spacing using two fringes one on either side of the same fringe group, e.g., fringes of order +3 and -3 in Fig. A.1a, would lead to small errors, since the maxima of these fringes do not fall exactly at the positions expected on the basis of the fringe spacing,  $d$ , based on  $\bar{\nu}$ . This effect is due to the modulating influence of the envelope. A better procedure would be to measure from a fringe near the centre of one fringe group to a fringe near the center of an adjacent group taking into account the phase inversion mentioned above. This, of course, assumes that the subsidiary fringe groups are visible, which may not always be the case.

Figure A.2a shows the effect on the white-light interference pattern of a density change in the test section, but assumes that no electrons have been produced. Also shown for reference is the intensity distribution on the white-light interferogram without the density change, i.e., Fig. A.1a. It is seen that the density change causes both the individual fringes and the fringe envelope to be shifted in the direction of positive  $y$ , but the envelope is shifted further than the individual fringes, as shown by the new positions of the zero-order fringe and the maximum of the fringe envelope. This is the "rollover" effect discussed earlier in Sec. 2.2.4, and is caused by the fact that the shift of individual fringes and the shift of the envelope are controlled by different indices of refraction. It is also noted that, if the density change were large enough, it is possible for the fringe envelope to be shifted sufficiently far with respect to the zero-order fringe that the first order fringe might be mistaken for the zero-order fringe. This is the danger that is always present when using white-light fringes to trace individual fringes through a density discontinuity: that the fringe which appears near the maximum of the fringe envelope on one side of the discontinuity may not be of the same order as the fringe which appears in the corresponding position near the maximum of the fringe envelope on the other side.

Figure A.3a shows a purely hypothetical case in shock tube work: here, electrons have been introduced, but no density change has occurred. Again, Fig. A.1a, which gives the interference pattern before the changes took place, is shown for reference. It is seen from the new positions of the zero-order fringe and of the maximum of the fringe envelope that individual fringes have been shifted in the direction of negative  $y$  while the fringe envelope has been shifted a similar amount toward positive  $y$ . It would also appear from this example that the maximum of the fringe envelope coincides with the maximum of one of the fringes; in general, however, this will not be true, and the maximum of the fringe envelope would not always coincide with the maximum of a fringe.

Finally, Fig. A.4a, shows the effect of a density change and an electron population appearing at the same time. It is seen that the effect of rollover, which was illustrated in Fig. A.2a, and the effect of the electrons, which was illustrated in Fig. A.3a, add together to produce the effect shown in Fig. A.4a. For example, it is seen that the distance between the positions of the zero-order fringe and the maximum of the fringe envelope in Fig. A.4a is simply the sum of the separations of these two positions shown in Fig. A.2a and Fig. A.3a. Also, the shift of the maximum of the fringe envelope in Fig. A.4a is the sum of the shifts illustrated in Fig. A.2a and Fig. A.3a. The same is true for the shift of the zero-order fringe.

Figure A.2a is typical of the intensity distribution in an interferogram of the gas behind a shock wave in oxygen, where there is a density change and dissociation, but where the effect of electrons can be neglected. Figure A.4a is typical of the intensity distribution in an interferogram of the gas behind a shock wave in argon; in this case ionization occurs giving rise to an electron population, and so producing the wide divergence between the position of the maximum of the fringe envelope and the position of the zero-order fringe. In all the above figures, the phase inversion between successive fringe groups, mentioned in connection with Fig. A.1a, is apparent.

Figures A.1a, A.2a, A.3a, and A.4a are plots of actual intensity. However, the darkening, or the density, on a photographic plate is proportional to the log of the intensity, and this quantity is plotted in Figs. A.1b, A.2b, and A.3b, and A.4b corresponding to the situations shown in their companion figures. By way of comparison, a typical densitometer trace across a white-light fringe pattern is shown in Fig. A.5, and it is seen that the resemblance in character between the actual density distribution and the calculated distribution is quite good. It is noted that the minima are much more sensitive indicators of the presence of electrons and of rollover than are the maxima, so that it is often more reliable to work with the minima when attempting to estimate to what extent these effects have caused the position of the maximum of the fringe envelope and position of the zero-order fringe to separate.

We now turn to Eq. A.19 where provision was made for an asymmetric spectral intensity distribution, as shown in Fig. 9b. As mentioned earlier, for the calculations  $\gamma$  was taken to be +1.0. Only three cases were plotted, Figs. A.6, A.7, and A.8, corresponding in all ways except for the value of  $\gamma$  with Figs. A.1a, A.2a, and A.4a. It is apparent that Eq. A.19 is not a good way of expressing the intensity distribution in the white-light interferogram, since, as shown in Fig. A.6, the spacing of the fringes no longer corresponds to  $\bar{\nu}$ , but to some frequency greater than  $\bar{\nu}$ . If  $\gamma$  had been chosen to be -1.0, for example, the spacing would have corresponded to a frequency less than  $\bar{\nu}$ . Plainly therefore, Eq. A.19 is only approximately correct, since all the indices of refraction in the equation are expressed in terms of  $\bar{\nu}$ , which is no longer the frequency governing the spacing of individual fringes.

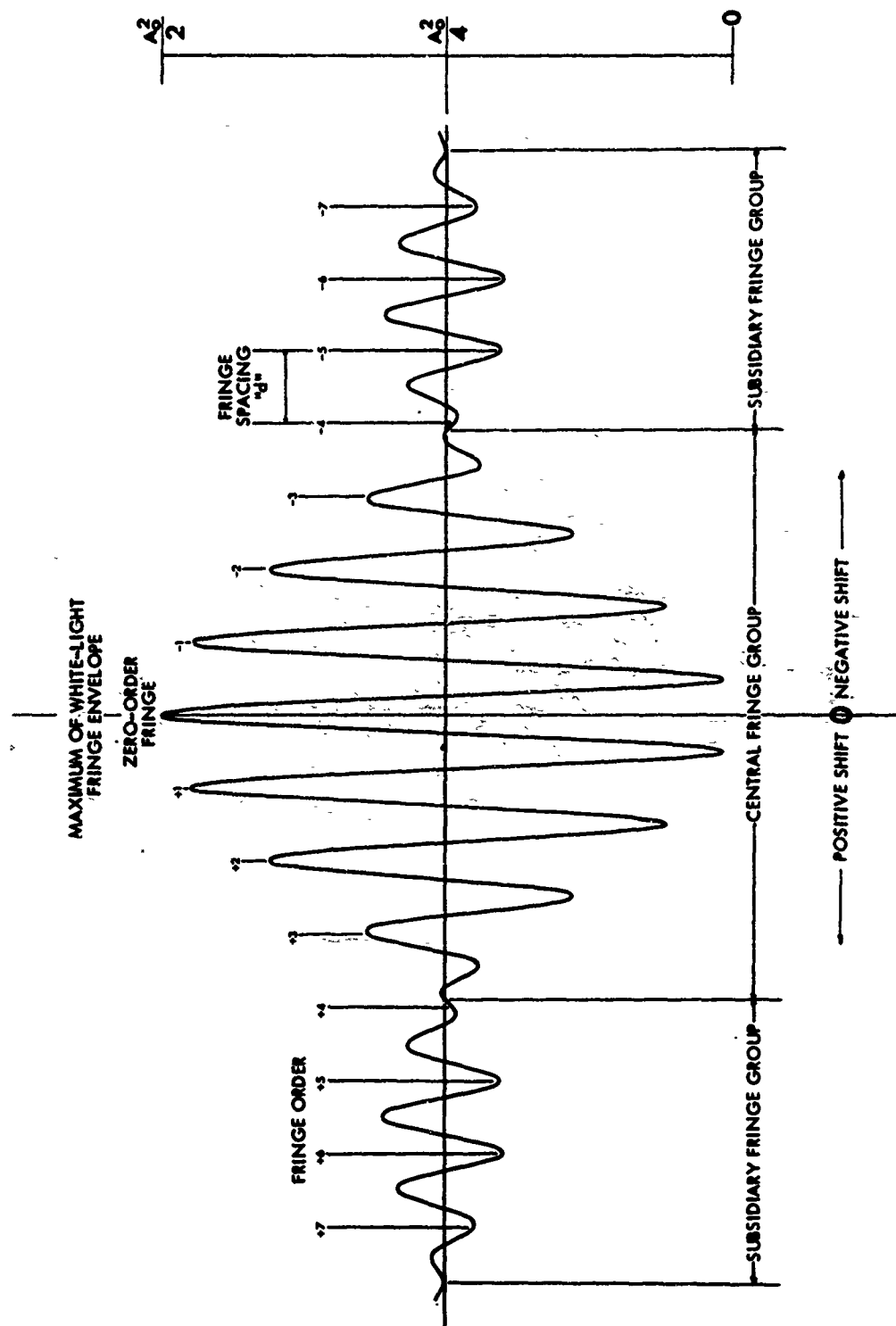


FIG. A1a - DISTRIBUTION OF INTENSITY IN A WHITE-LIGHT INTERFEROGRAM WITH TEST SECTION AND COMPENSATING CHAMBER CONDITIONS IDENTICAL

(Symmetric spectral intensity distribution;  $\bar{\lambda} = 4960\text{\AA}$ )

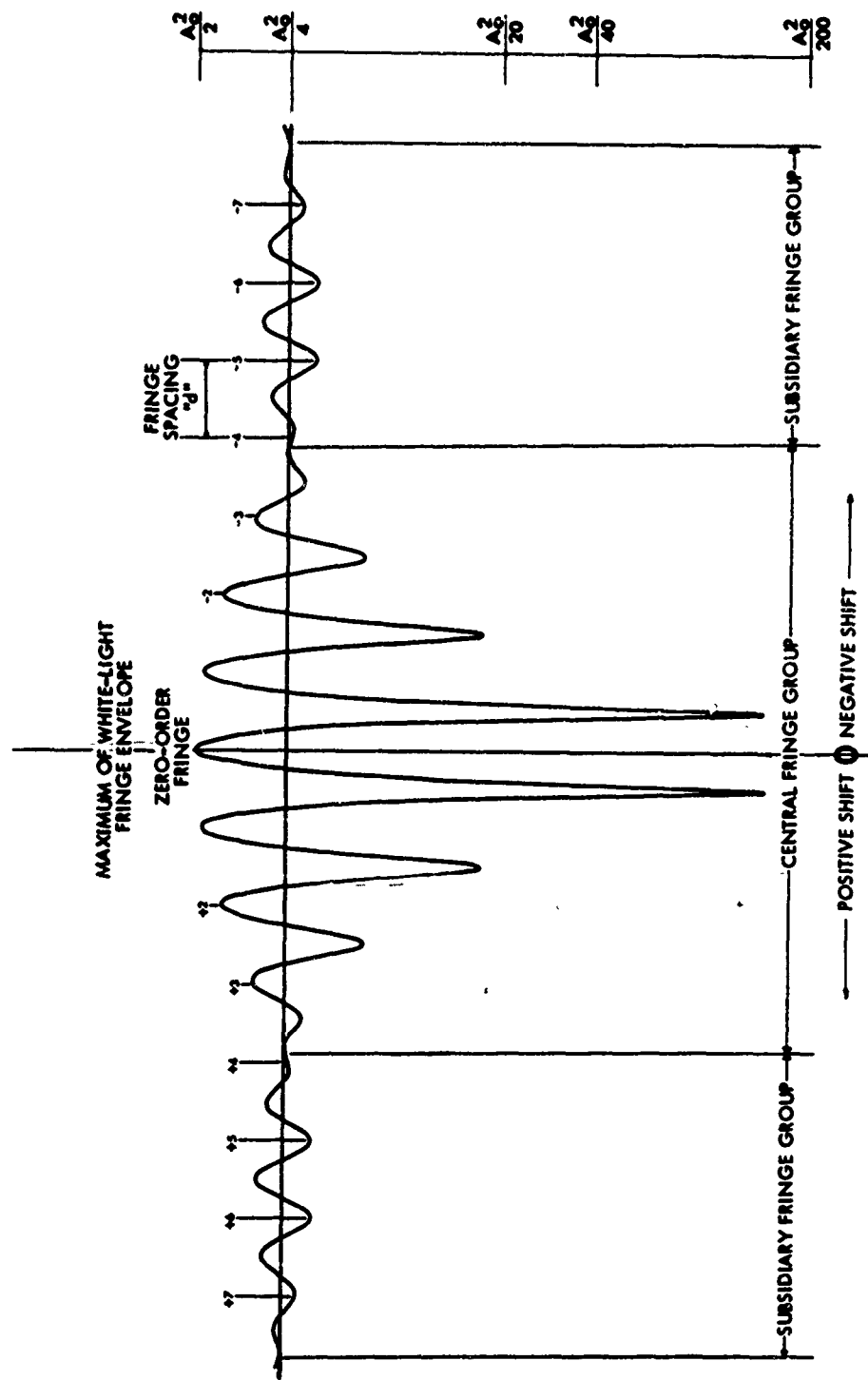


FIG. A1b - DISTRIBUTION OF LOG INTENSITY IN A WHITE-LIGHT INTERFEROGRAM WITH TEST SECTION AND COMPENSATING CHAMBER CONDITIONS IDENTICAL

(Symmetric spectral intensity distribution;  $\lambda = 4960\text{\AA}$ )

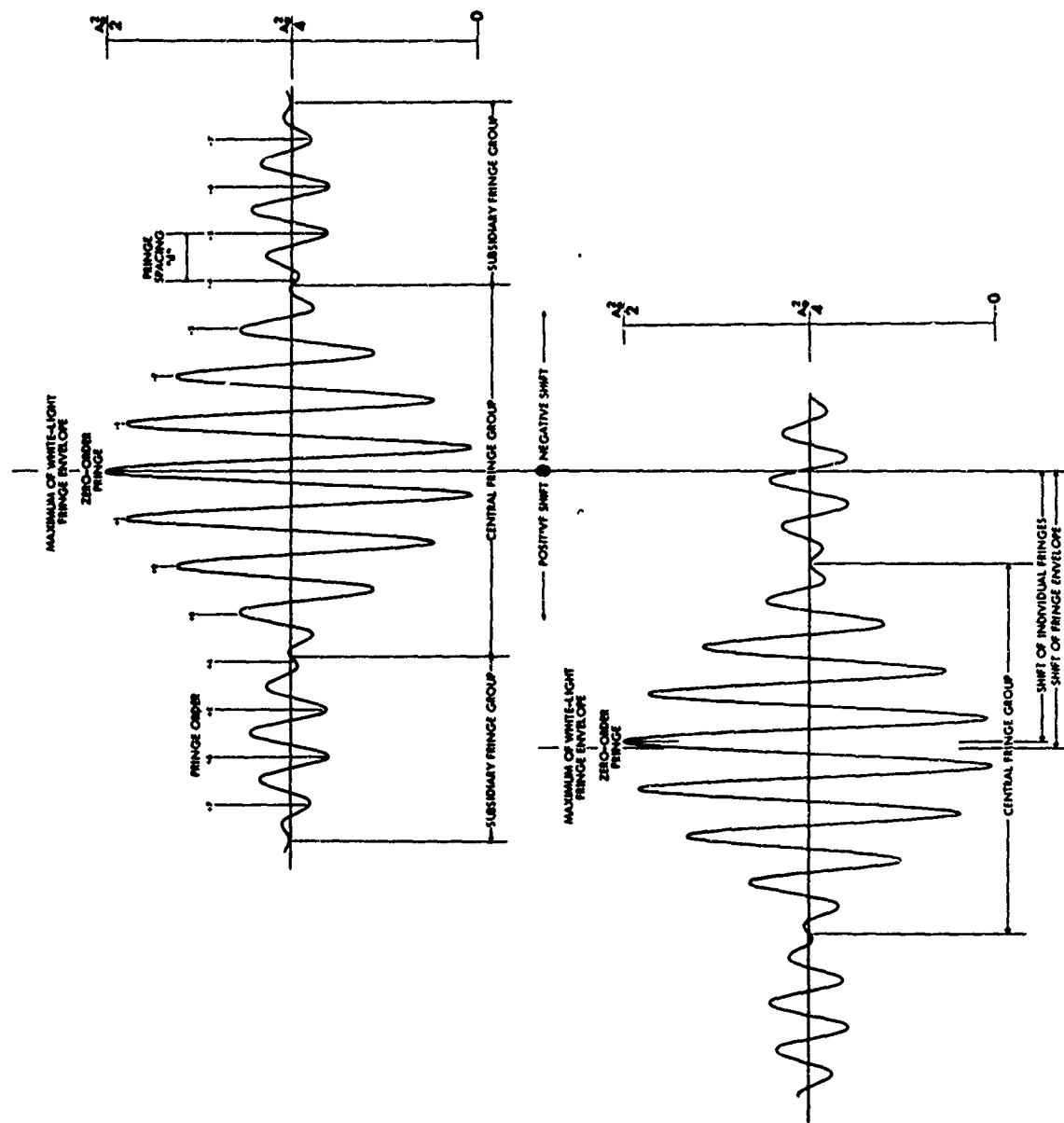


FIG. A2a - DISTRIBUTION OF INTENSITY IN A WHITE-LIGHT INTERFEROGRAM SHOWING EFFECT OF A DENSITY CHANGE

(Symmetric spectral intensity distribution;  $\bar{\lambda} = 4960\text{\AA}$ )



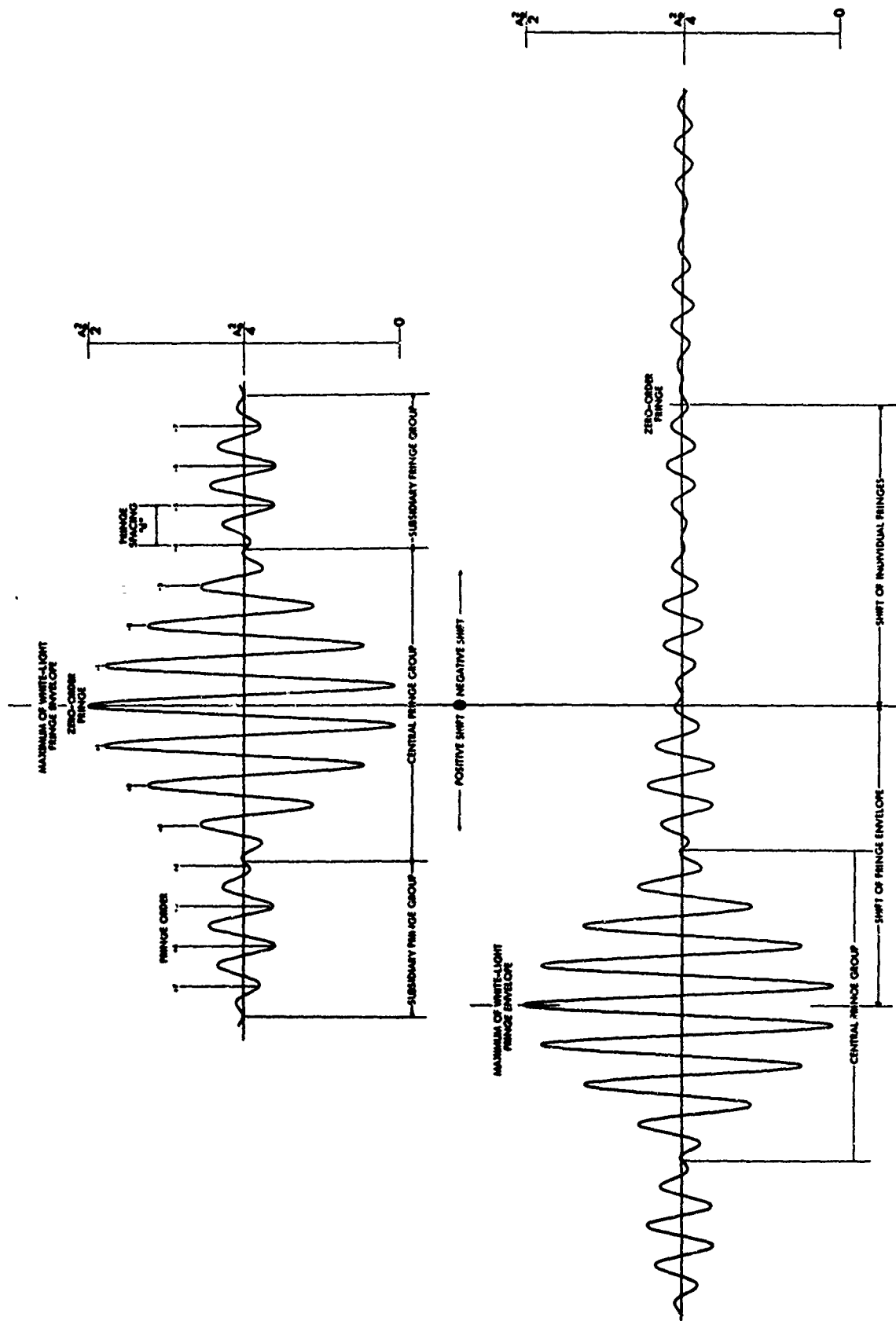


FIG. A3a - DISTRIBUTION OF INTENSITY IN A WHITE LIGHT INTERFEROGRAM SHOWING EFFECT OF AN ELECTRON POPULATION

(Symmetric spectral intensity distribution;  $\bar{\lambda} = 4960\text{\AA}$ )

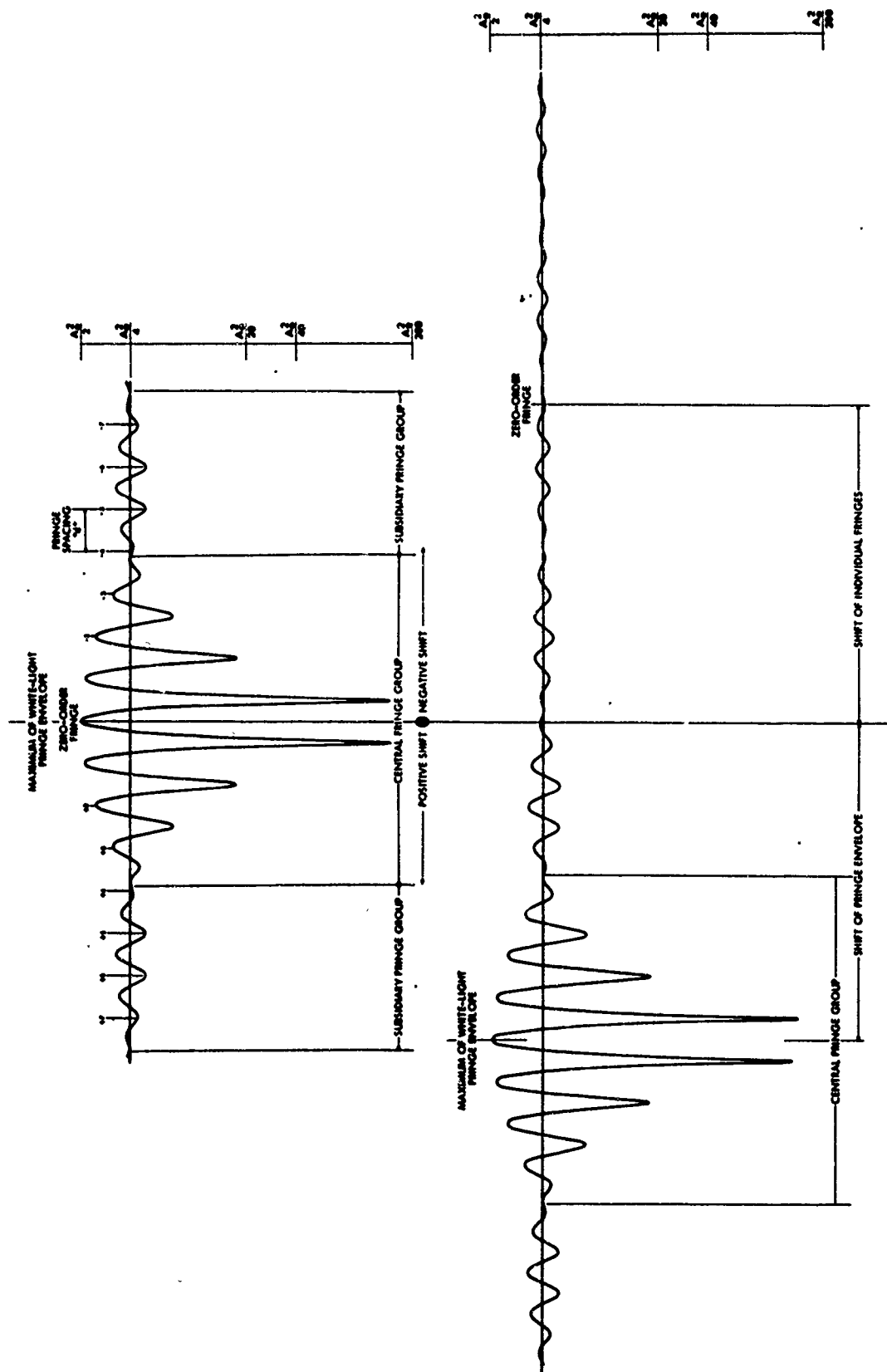
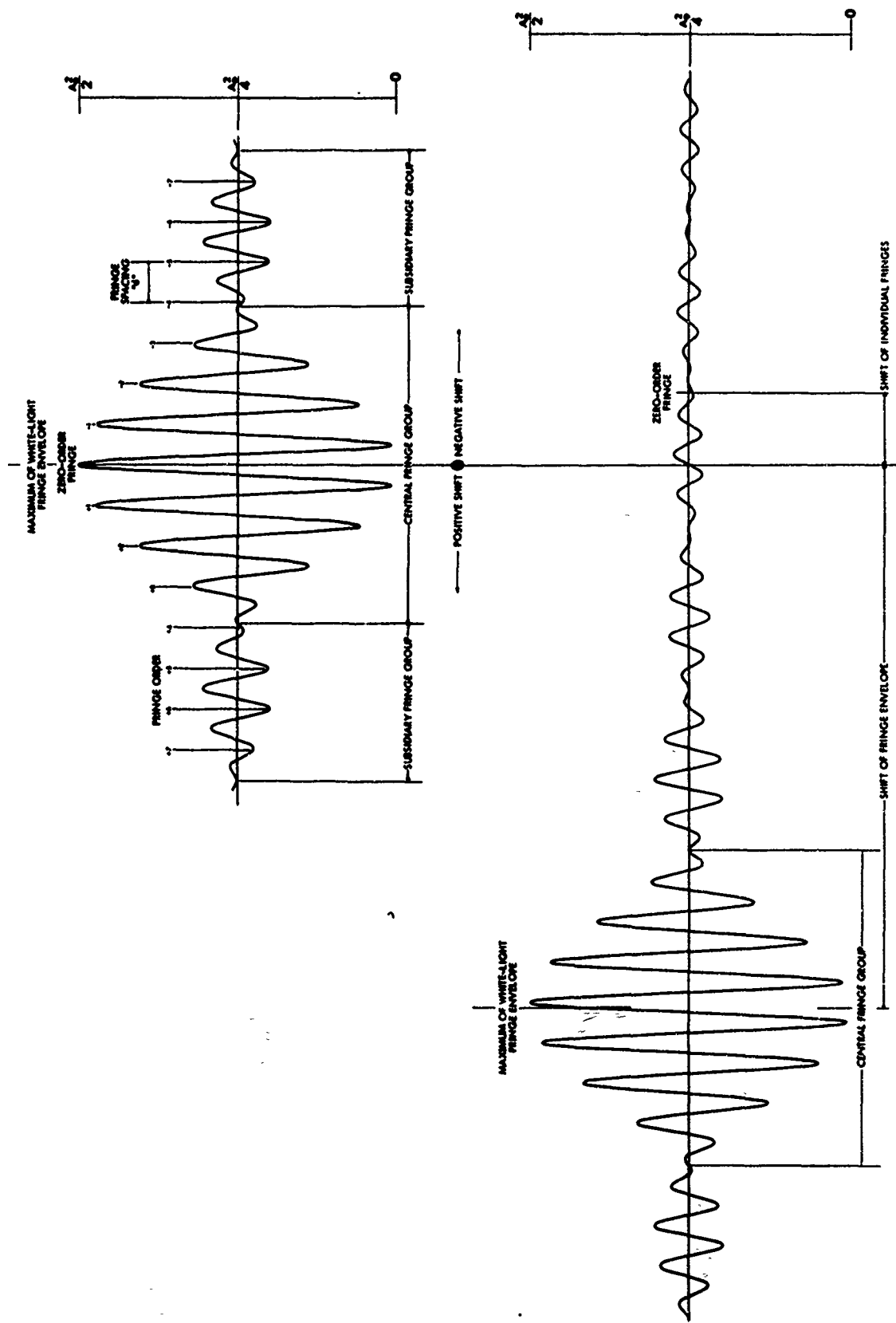


FIG. A3b - DISTRIBUTION OF LOG INTENSITY IN A WHITE-LIGHT INTERFEROGRAM SHOWING EFFECT OF AN ELECTRON POPULATION

(Symmetric spectral intensity distribution;  $\lambda = 4860\text{\AA}$ )



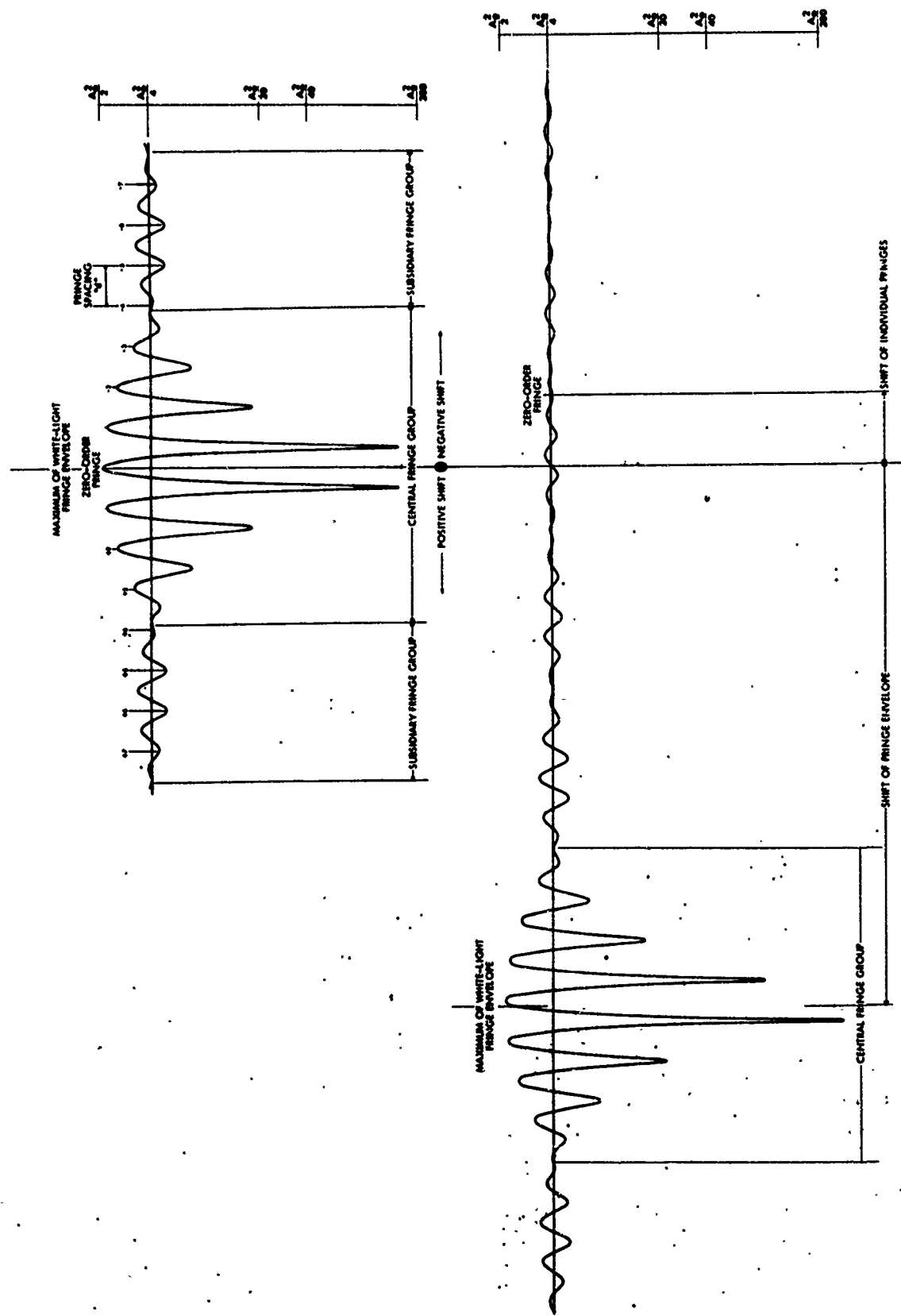


FIG. A4b - DISTRIBUTION OF LOG INTENSITY IN A WHITE-LIGHT INTERFEROGRAM SHOWING EFFECT OF AN ELECTRON POPULATION AND A DENSITY CHANGE APPEARING TOGETHER

(Symmetric spectral intensity distribution;  $\lambda = 4960\text{\AA}$ )



**FIG. A5 - TYPICAL DENSITOMETER TRACE ACROSS A WHITE-LIGHT FRINGE  
PATTERN AS RECORDED ON A PHOTOGRAPHIC PLATE**

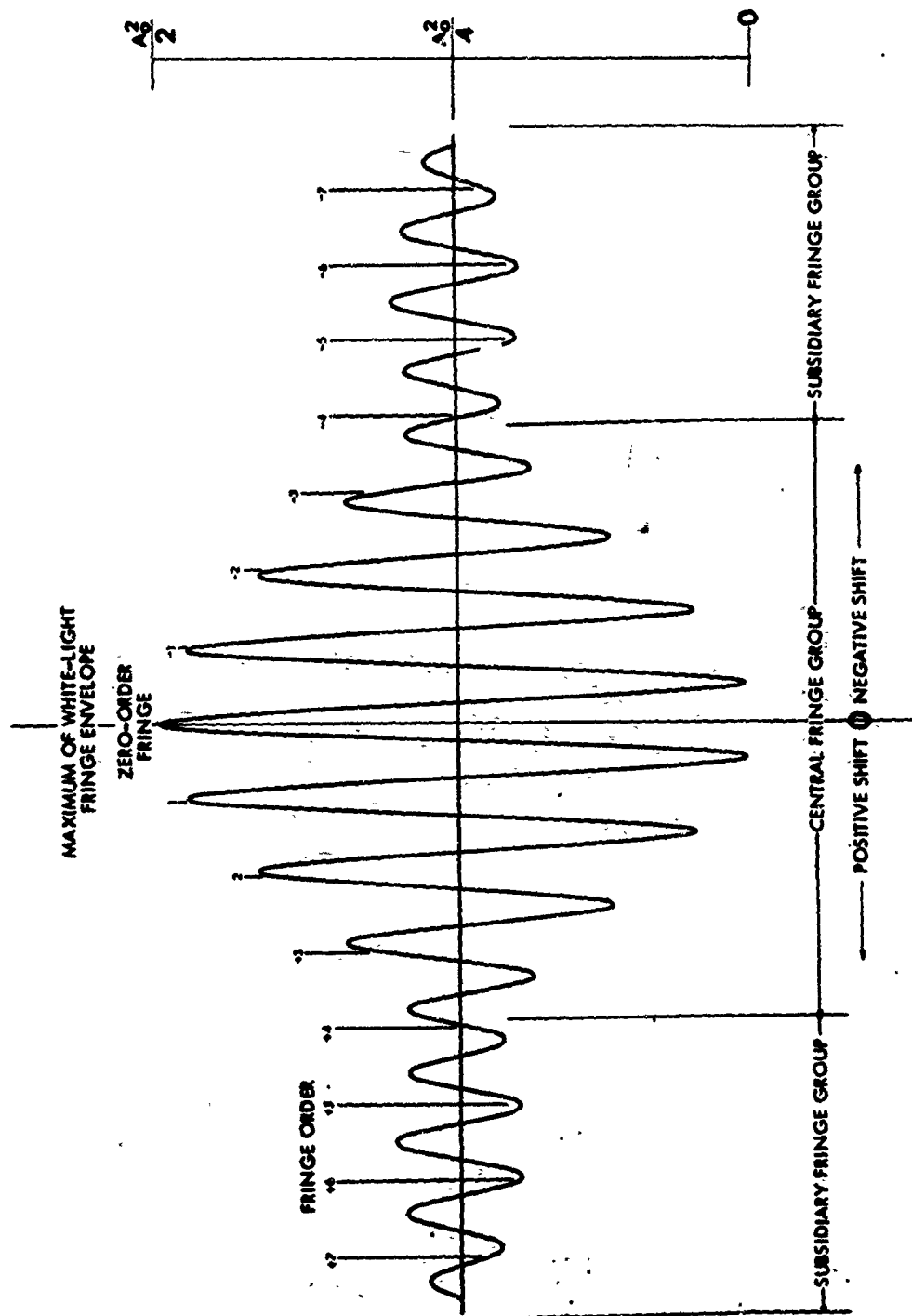


FIG. A6 - DISTRIBUTION OF INTENSITY IN A WHITE-LIGHT INTERFEROGRAM WITH TEST SECTION AND COMPENSATING CHAMBER CONDITIONS IDENTICAL - ASYMMETRIC SPECTRAL INTENSITY DISTRIBUTION

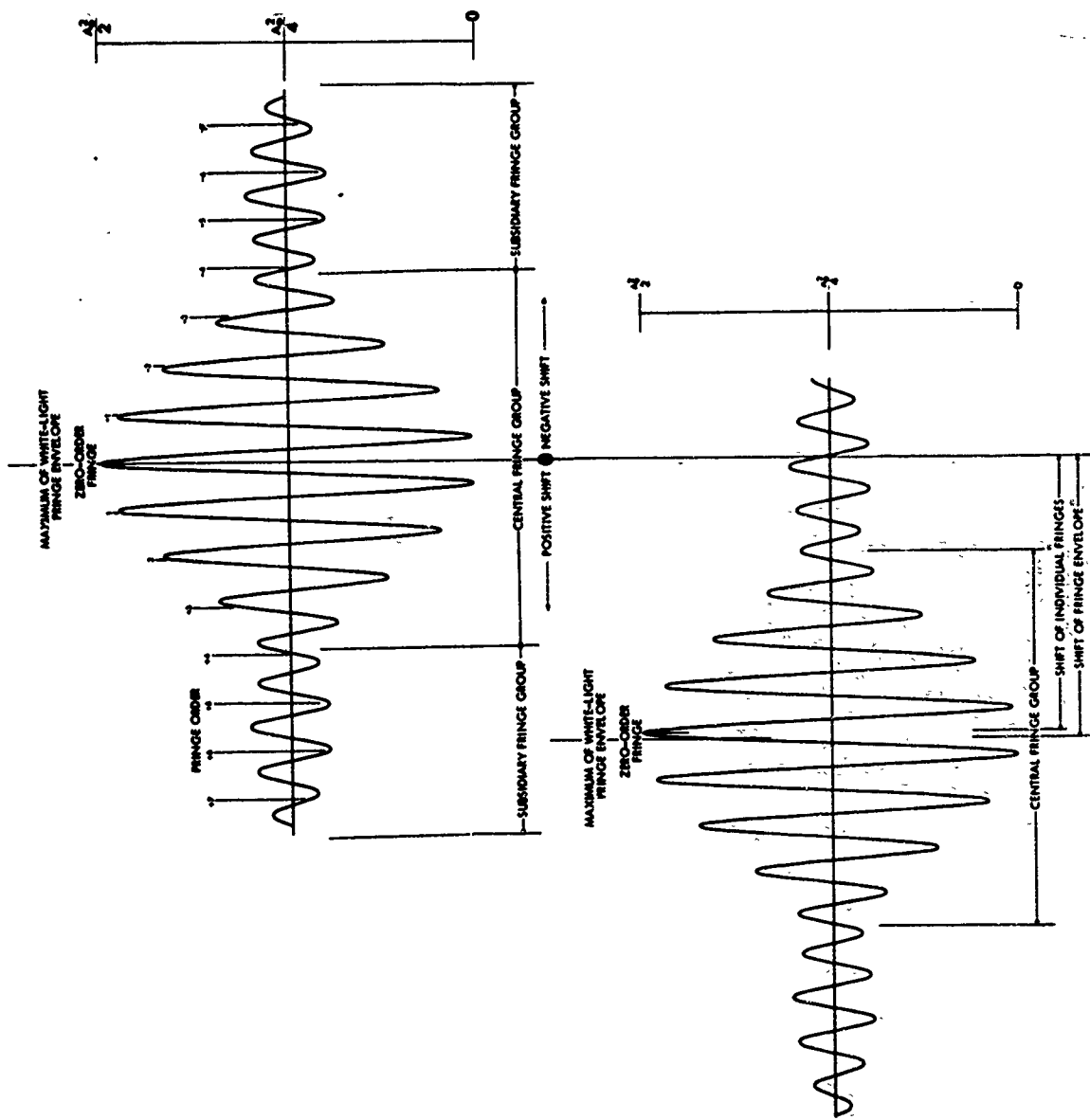


FIG. A7 - DISTRIBUTION OF INTENSITY IN A WHITE-LIGHT INTERFEROGRAM SHOWING EFFECT OF A DENSITY CHANGE - ASYMMETRIC SPECTRAL INTENSITY DISTRIBUTION

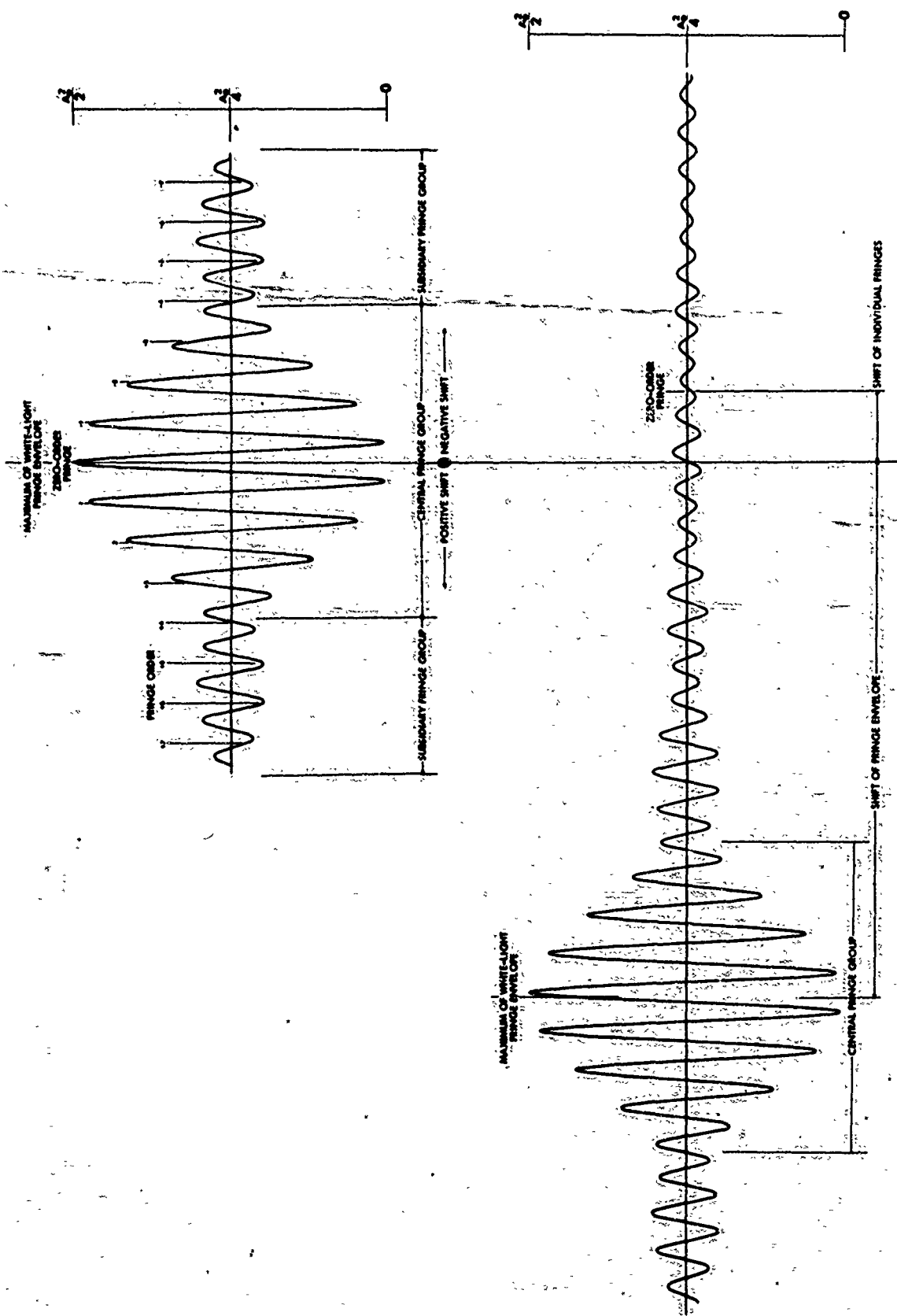


FIG. A8 - DISTRIBUTION OF INTENSITY IN A WHITE-LIGHT INTERFEROGRAM SHOWING EFFECT OF AN ELECTRON POPULATION AND A DENSITY CHANGE APPEARING TOGETHER - ASYMMETRIC SPECTRAL INTENSITY DISTRIBUTION

## APPENDIX B

### A Summary of the Experimental Work Done to Date (March 1966) on the Determination of the Gladstone-Dale Constants for Argon

Some work has been done on the determination of the Gladstone-Dale constants for ionizing argon, but several problems have arisen preventing immediate completion of this work.

The basic procedure for carrying out the determination of the Gladstone-Dale constants for ionizing argon is given in Appendix B of Ref. 1. As with the oxygen work, it was proposed to pass a strong shock wave through the gas and then measure the index of refraction of the resulting hot ionizing gas using the Mach-Zehnder interferometer. From this determination of the index of refraction, the Gladstone-Dale constants for the argon atom and ion can be determined, using an analysis similar to that outlined in Sec. 3.1.

There is, however, one additional complication in the argon work: electrons are present in the hot gas as well as ions and neutral atoms, and the contribution of the electrons to the total refractivity of the gas must be taken into account. It was proposed to do this by making use of simultaneous white-light and monochromatic interferograms. As shown in Sections 2.2.3, 2.2.4, and Appendix A, on a given white-light interferogram the electrons produce a positive shift of the white-light fringe envelope, and a negative shift of individual fringes. These shifts due to the electrons are of equal magnitude, and are in addition to say fringe shifts caused by a change in density.

This can be seen from Eq. A.6. For a given individual fringe on a white-light interferogram, the argument of the cosine in Eq. A.6 has a constant value. In particular, for the zero-order fringe, we have:

$$2 [X_1(\rho_1 - \rho_2)\Delta_0 - X_2\gamma(1 + \Delta'_0) - X_3] \bar{\nu} = 0 \quad (\text{B.1})$$

Since, as shown in Appendix A,  $\Delta_0$  is the Gladstone-Dale constant corresponding to the phase index of refraction, we substitute:

$$K_p = \Delta_0$$

Similarly  $(1 + \Delta'_0)$  was shown to be the phase index of refraction of air; hence:

$$n_{p_a} = 1 + \Delta'_0$$

Thus, incorporating these changes, and substituting for  $X_1$ ,  $X_2$  and  $X_3$ , Eq. B.1 becomes:

$$\frac{2\pi L \bar{\nu}}{c} (\rho_2 - \rho_1) K_p - \frac{4\pi \epsilon \gamma \bar{\nu} n_{p_a}}{c} - \frac{2L \bar{\nu} (\omega_p)_2^2}{8\pi c \bar{\nu}^2} = 0 \quad (\text{B.2})$$

If one now removes the assumption of only one species present in the test section (imposed for simplicity in Sec. 2.2.4), and substitutes:

$$4\pi\bar{v}^2 = \bar{\omega}^2; \quad \frac{\bar{v}}{c} = \frac{1}{\bar{\lambda}_0}$$

Equation B.2 becomes

$$\frac{L}{\bar{\lambda}_0} \sum_i [(\rho_2 - \rho_1)_i K_{pi}] - \frac{2\epsilon n_{pi}}{\bar{\lambda}_0} y - \frac{L}{\bar{\lambda}_0} \frac{(\omega_p)_2^2}{2\omega^2} = 0$$

From Sec. 2.2.3, the spacing between individual fringes on an interferogram is given by:

$$d = \frac{\bar{\lambda}_0}{2\epsilon n_{pa}}$$

Hence:

$$\frac{y}{d} = S_{12m} = \frac{L}{\bar{\lambda}_0} \left\{ \rho_2 [K_{patom}(1-x) + K_{pion} x] - \rho_1 K_{patom} - \frac{(\omega_p)_2^2}{2\omega^2} \right\} \quad (B.3)$$

where substitution has also been made for the Gladstone-Dale constants; in front of the shock, only atoms are present, behind the shock, atoms, ions and electrons are present.

Similarly, the shift of the fringe envelope is given by the argument of the sine in Eq. A.6, viz:

$$[X_1(\rho_2 - \rho_1)(\Delta_0 + \Delta_1) - X_2 y(1 + \Delta'_0 + \Delta'_1) + X_3] (\nu_2 - \nu_1) = 0 \quad (B.4)$$

Proceeding, as before, we substitute (see Appendix A):

$$K_g = \Delta_0 + \Delta_1$$

$$n_{ga} = 1 + \Delta'_0 + \Delta'_1$$

whence:

$$d = \frac{\bar{\lambda}_0}{2\epsilon n_{ga}} \approx \frac{\bar{\lambda}_0}{2\epsilon n_{pa}}$$

The approximation made here in setting  $n_{pa}$  equal to  $n_{ga}$  is in line with the note in Appendix A, where it was pointed out that  $\Delta'_0$  and  $\Delta'_1$  are numbers of order  $10^{-4}$ , and, since these indices of refraction enter only through the fringe spacing, one is justified in setting  $n_{pa}$  equal to  $n_{ga}$ .

Thus proceeding as before, Eq. B.4 becomes:

$$\frac{y}{d} = S_{12w} = \frac{L}{\bar{\lambda}_0} \left\{ K_{gatom} (1-x) + K_{gion} x - \rho_1 K_{gatom} - \frac{(\omega_p)_2^2}{2\omega^2} \right\} \quad (B.5)$$

An expression similar to Eq. B.3 could be written for the case of a monochromatic interferogram also. For example, the argument of  $\cos^2$  in Eq. 4.3

becomes:

$$S_{12m} = \frac{L}{\lambda_0} \left\{ \rho_2 \left[ K_{patom} (1-x) + K_{pion} x \right] - \rho_1 K_{patom} - \frac{(\omega_p)^2}{2\omega^2} \right\} \quad (B.6)$$

where  $\lambda_0$  in this case is any arbitrary wavelength, which may or may not be equal to  $\bar{\lambda}_0$  in Eqs. B.3 and B.5.

Thus if Eqs. B.3 and B.5 were added (or B.5 and B.6, provided  $\lambda_0$  was equal to  $\bar{\lambda}_0$ , i.e.,  $\omega = \bar{\omega}$ ), the terms  $(\omega_p)^2/2\omega^2$  will cancel out, viz:

$$S_{12m} + S_{12w} = \frac{L}{\lambda_0} \left\{ \rho_2 \left[ (K_{gatom} + K_{patom})(1-x) + (K_{gion} + K_{pion})x \right] - \rho_1 (K_{gatom} + K_{patom}) \right\} \quad (B.7)$$

(Usually,  $S_{12m}$  will not be visible on the white-light interferogram, since the zero order fringe is too far from the maximum of the fringe envelope. Thus  $S_{12m}$  must be obtained from a monochromatic interferogram, and if  $\lambda_0$  for the monochromatic interferogram is not equal to  $\bar{\lambda}_0$  of the white-light interferogram, an error arises, because the terms  $(\omega_p)^2/2\omega^2$  will not cancel exactly, when Eqs. B.5 and B.6 are added.)

At this stage, one must introduce an approximation, and set  $K_p$  equal to  $K_g$ . The difference between these two quantities is what causes rollover, and, on the basis of rollover measurements, the difference between  $K_p$  and  $K_g$  is about 5%. This reduces the number of unknowns from four to two, and makes possible the use of the analysis given in Sec. 3.1.

The preceding paragraphs give the basis of the method proposed for determining the Gladstone-Dale constants for ionizing argon. However the practical problem of determining the fringe shifts  $S_{12w}$  and  $S_{12m}$  remains.

Once ionization begins behind a shock wave in argon, the white light fringes can no longer be used to identify particular fringes, as was done for the oxygen work, since, when ionization begins  $\omega_p^2/2\omega^2$  is no longer zero and the shift of the fringe envelope on a white-light interferogram and the shift of individual fringes on a monochromatic interferogram are no longer related as they were for the oxygen work. Hence, if the white-light fringes are to be used to trace particular individual fringes through the shock front, this must be done where there is no ionization, i.e., immediately behind the shock wave. Once the individual fringes are traced through the shock front, they can be followed visually to the equilibrium region, and  $S_{12m}$  determined.

Thus, it is seen that, if the region immediately behind the shock wave is obscured for some reason, individual fringes behind the shock wave cannot be correlated with those in front of the shock wave, and  $S_{12m}$  cannot be determined. This was the first problem encountered, and is illustrated by the interferograms shown in Fig. B.1. These interferograms were taken with a magnesium spark source in the interferometer, and the blurring of the frozen (no ionization) region behind the shock wave is due to the poor time resolution (2  $\mu$ sec.) available with this source. In addition, the white-light interferograms were badly fogged by the radiation of the hot gas in the test section. (Fogging of the monochromatic interferograms was prevented because of an inter-

ference filter between the photographic plate and the test section which filtered out most of the radiation).

The expected fringe shifts are shown in Table B1, along with the measured fringe shifts. For the interferograms shown in Fig. B.1, the frozen fringe shift and the monochromatic fringe shift could not be determined for the reasons given above, but the shift of the white-light fringe envelope appears to be approximately correct: approximately correct inasmuch as it is impossible on these interferograms to determine exactly where the maximum of the white-light fringe envelope falls. However, there appears to be a reasonable relaxation time behind the shock wave, amounting to 3-4 microseconds. Thus, while no accurate measurements could be made, the rough measurement of  $S_{12_w}$  indicated that conditions behind the shock wave were fairly close to those predicted by theory. At this point, development of the exploding wire light source was put in hand so that a Kerr Cell could be used to improve the time resolution from two microseconds to 200 nanoseconds, allowing accurate quantitative information to be obtained.

Some time later, after development of the exploding wire light source was completed, a return was made to the argon work, and the interferograms from one of the first runs are shown in Fig. B.2. It is seen that the required time resolution was achieved. Approximate fringe shifts were determined and are compared with the predicted fringe shifts in Table B.1. The frozen fringe shift was determined by putting a piece of paper over the flow side of the interferogram leaving only the frozen region behind the shock wave exposed to view. The white-light fringe pattern in the exposed frozen region could then be correlated with the white-light fringe pattern in front of the shock wave, and particular fringes could then be traced through the shock front, as was done for the oxygen work. The equilibrium shift of the white-light fringe envelope  $S_{12_w}$  was determined to the nearest fringe only, introducing an error of 0.5 fringes at most.  $S_{12_m}$  was determined by transferring the frozen fringe shift from the white light interferogram to the monochromatic interferogram, as was done in the oxygen work; the individual fringe could then be traced to the equilibrium region, where  $S_{12_m}$  was determined.

These measurements showed that the frozen fringe shift was being achieved roughly as predicted, but that wide discrepancies existed in  $S_{12_m}$  and  $S_{12_w}$ . These discrepancies indicated that full ionization, as predicted by normal shock calculations, was not being achieved. It was also noted that the relaxation zone shown in Fig. B.2 was much shorter than that shown in Fig. B.1.

Some diagnostic runs were then taken in an attempt to clarify the situation. Since the interferograms shown in Fig. B.2 were among the first taken with the exploding wire source and Kerr Cell, this run was duplicated, but using the old magnesium spark source in order to be certain that the Kerr Cell and/or exploding wire source were not causing odd effects. The resulting interferograms are shown in Fig. B.3. The fogging due to the test-section radiation is apparent, as in Fig. B.1. However, although the frozen and monochromatic fringe shifts could not be determined, the equilibrium shift of the white-light fringe envelope was as in Fig. B.2 (see Table B1). In addition Fig. B.3 indicates little or no relaxation zone, compared to Fig. B.1, indicating that the small relaxation zone visible in Fig. B.2 (where the time resolution is better) is real. Thus, the run indicated that the optical arrangements were not causing trouble.

At first glance then, on the basis of Figs. B.2 and B.3, the most likely explanation of the anomalies noted in Fig. B.2 was an impurity in the gas, probably oxygen or nitrogen. The dissociation energy of nitrogen or oxygen is much lower than the ionization energy of argon, so that practically all of the diatomic impurity is dissociated before the argon begins to ionize. However, only 10% ionization was expected, so that, if even only a few percent of impurity were present, most of the energy of the gas would go into dissociating the impurity, and very little into ionizing the argon, thus reducing the ionization level below that predicted.

Thus the run illustrated in Fig. B.2 was duplicated again, but using special high-purity reagent grade argon, and the results of this run are shown in Fig. B.4. Approximate measurements of fringe shift were made as before, and these are compared with theory in Table B.1. It is seen that the results are nearly identical with the run shown in Fig. B.2 as regards fringe shifts, and also as regards relaxation time. The conclusion was then reached that the anomalies were not caused by gas impurity.

TABLE B.1

THEORETICAL & MEASURED FRINGE SHIFTS FOR ARGON RUNS

FIG. B.1       $M_s = 13.95$ ,     $p_1 = 9.0$  mm Hg,  $x = 8.25\%$ ,  $\rho_2/\rho_1 = 6.18$

	Theoretical	Measured
$S_{12f}$	1.78	-
$S_{12w}$	6.47	6.0
$S_{12m}$	- .50	-

FIG. B.2       $M_s = 14.29$ ,     $p_1 = 9.8$  mm Hg,  $x = 8.95\%$ ,     $\rho_2/\rho_1 = 6.32$

	Theoretical	Measured
$S_{12f}$	1.91	3.4
$S_{12w}$	7.54	5.5
$S_{12m}$	- .88	+2.8

FIG. B.3       $M_s = 14.18$ ,     $p_1 = 9.8$  mm Hg,  $x = 8.65\%$ ,     $\rho_2/\rho_1 = 6.26$

	Theoretical	Measured
$S_{12f}$	1.92	-
$S_{12w}$	7.33	5.5
$S_{12m}$	- .74	-

FIG. B.4       $M_s = 14.18$ ,     $p_1 = 9.8$  mm Hg,  $x = 8.65\%$ ,     $\rho_2/\rho_1 = 6.26$

	Theoretical	Measured
$S_{12f}$	1.92	3.6
$S_{12w}$	7.33	5.5
$S_{12m}$	- .74	+3.0



**FIG. B1 - WHITE-LIGHT AND MONOCHROMATIC INTERFEROGRAMS of a shock wave in argon, typical of the early interferograms taken with the magnesium spark light source. Note the blurring of the shock front due to poor time resolution; also fogging of white-light interferogram ( $M_s = 13.95$  ,  $p_1 = 9.0$  mm Hg)**

(Shock moving right to left; height of field of view is approximately 7")

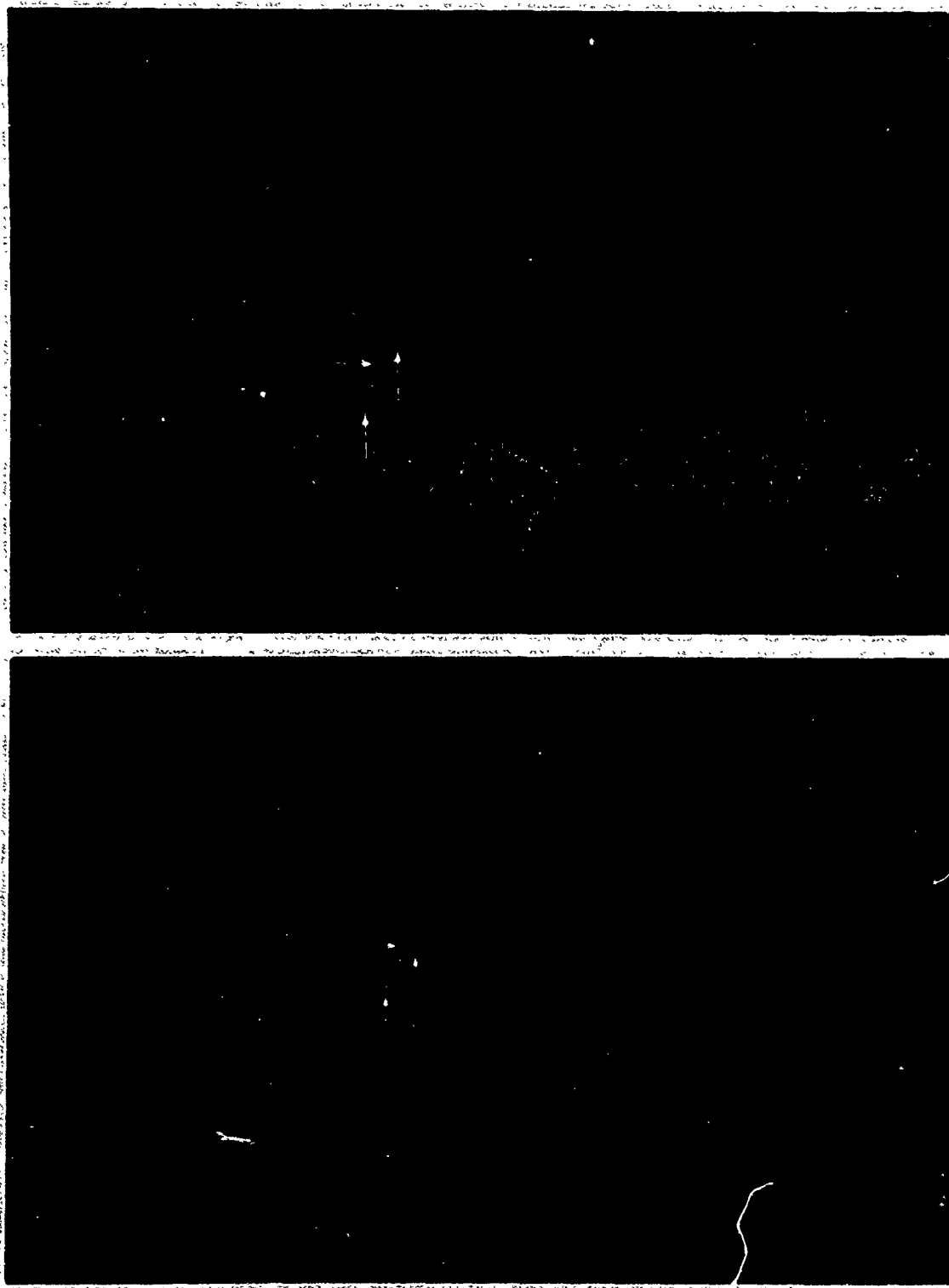


**FIG. B2 - WHITE-LIGHT AND MONOCHROMATIC INTERFEROGRAMS of a shock wave in argon taken with exploding wire light source and Kerr Cell. Note improved time resolution and lack of fogging ( $M_s = 14.29$  ,  $p_1 = 9.8$  mm Hg)**

**(Shock moving right to left; height of field of view is approximately 7")**

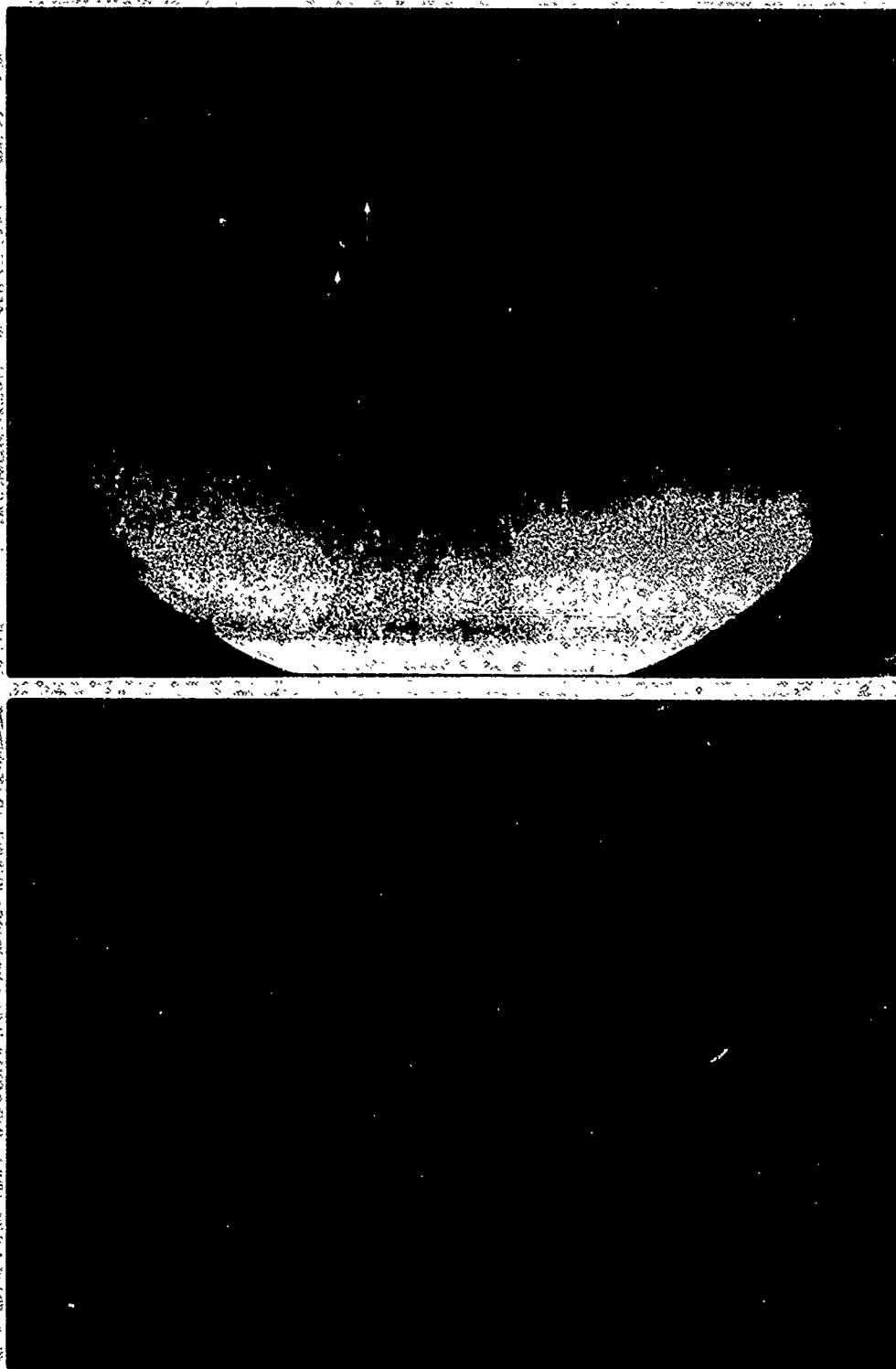


**FIG. B3 - INTERFEROGRAMS** from run duplicating that shown in Fig. B2, but taken with magnesium spark light source ( $M_s = 14.18$  ,  $p_1 = 9.8$  mm Hg)

(Shock moving right to left; height of field of view is approximately 7")

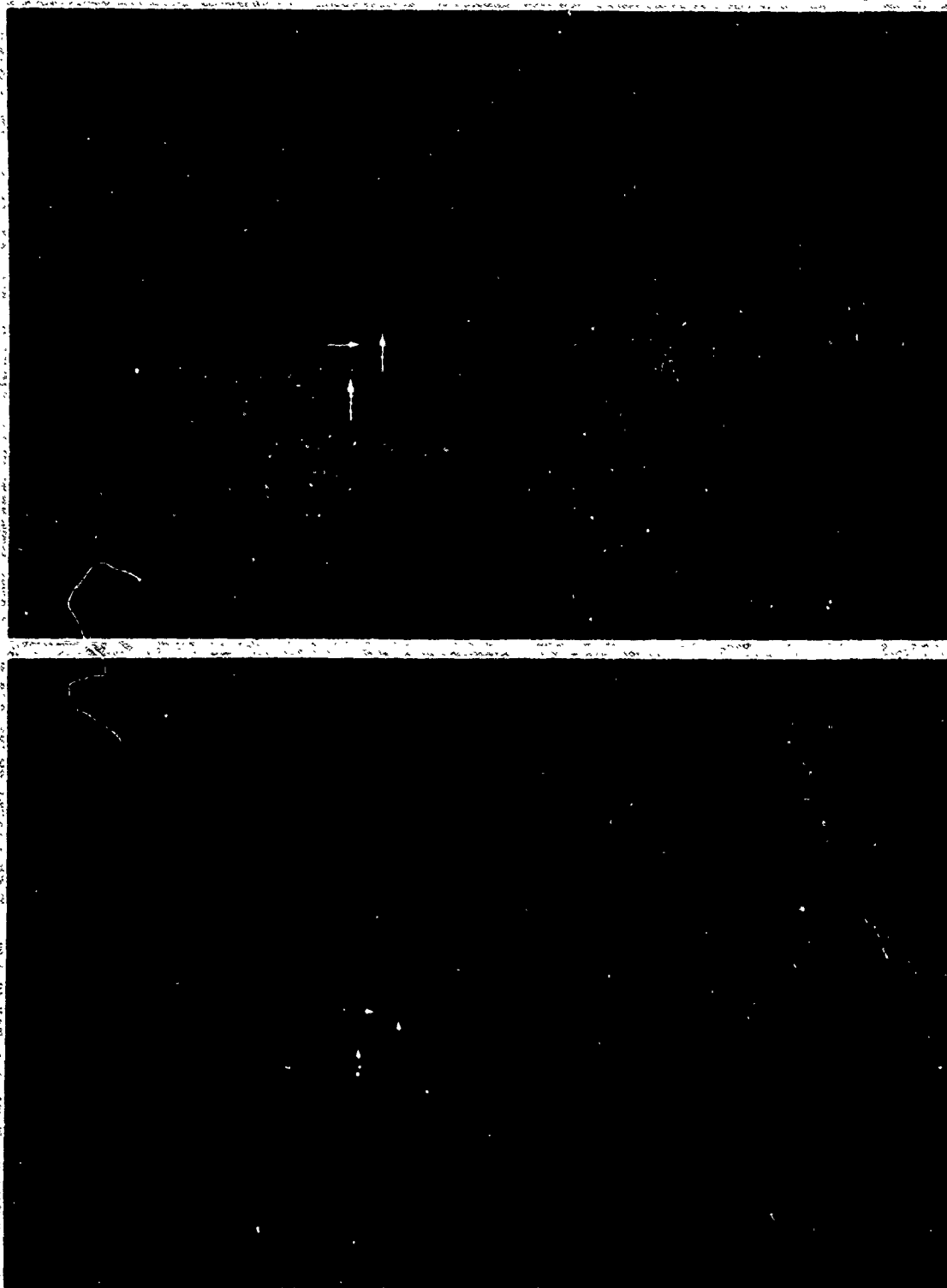


**FIG. B4 - INTERFEROGRAMS from run duplicating that shown in Fig. B2, but taken using high-purity argon ( $M_s = 14.18$ ,  $p_1 = 9.8$  mm Hg)**

**(Shock moving right to left; height of field of view is approximately 7")**

## APPENDIX C

### An Exploding Wire Light Source for the UTIAS 9-in. Mach-Zehnder Interferometer

#### C.1 Requirement

In the course of the experimental work to determine the Gladstone-Dale constants, a need arose for improved time resolution in the interferograms of the shock wave. Previously, the light source used with the interferometer had been a spark using magnesium electrodes, with energy supplied by a 0.2  $\mu$ f capacitor charged to 10 kv. A typical time-resolved intensity trace of the emitted light, taken with an EG & G\* SD-100 photodiode, is shown in Fig. 1: it is seen that the duration of the light output is of the order of two microseconds.

This was sufficiently brief for the trials using oxygen as the test gas, even though the shock wave was blurred considerably, since it was necessary only that the equilibrium regions be clearly defined. For the argon work, however, this was no longer acceptable. Here it was necessary that the Rankine-Hugoniot region immediately behind the shock wave, where there was no ionization, be visible, (see Appendix B) and thus time resolution of better than one microsecond became necessary.

The increased time resolution could be obtained in either of two ways: by decreasing the duration of the light output from the spark, or by installing in the system a very fast shutter, in either case, cutting down the duration of the light output as seen by the camera. Both of these methods were investigated. It was found however that, to shorten the duration of the spark, it was necessary to reduce the energy of the discharge, and no significant decrease in duration occurred until the energy of the discharge was so low that the resultant light output was too weak for photographic recording. Various kinds of capacitors in various configurations were investigated, but without significant improvement.

Thus, only the alternative remained. However, no mechanical shutter could be made fast enough to satisfy the requirements for time resolution and still be capable of precise synchronization with other events. This, then, necessitated the use of an electro-optical shutter, e.g., a Kerr Cell, which has no moving parts and can be synchronized precisely. Unfortunately, a Kerr Cell has; inherently, very low transmission\*\*even when open, and it was found, when one was used in conjunction with the magnesium spark, that the intensity of the light output was too low to overcome the poor transmission. Efforts to increase the intensity of the light from the source by increasing the energy of the discharge produced very little improvement and caused excessively fast erosion of the magnesium electrodes.

---

\* Edgerton, Germeshausen & Grier, Inc.,

\*\* The theoretical maximum transmission of a beam of non-polarized light is only 50%; only the use of expensive crystal polarizers will allow the transmission to approach this figure.

However, with the Kerr Cell, the duration of the light output from the source became of secondary importance and brevity could be sacrificed for increased peak intensity. Thus a different type of light source could be used in place of the spark.

The requirement was for a source of small diameter, since the interferometer required at least a pseudo-point source, combined with high peak brightness, i.e., light output per unit area. For this reason, flash tubes and other types of lamps were rejected; these had plenty of power, but their luminous area was quite large, leading to low brightness. Other light sources involving explosives were rejected because of possible damage to the interferometer situated close by.

This left the possibility of using the light output obtained when a small piece of wire was vaporized by an electric discharge. Our contacts with other laboratories (Ref. 16) had indicated that the exploding wire source was a practical solution, having been used with considerable success.

There remained, at this stage, one further possibility: that of using a laser as the light source. This, however, would have involved considerable expense and delay besides being difficult to adapt to the present installation. Thus the idea of using a laser was rejected, at least for the time being, since the exploding wire source appeared to be much cheaper, easier to construct, and more expedient in terms of the time required to get it into operation.

#### C.2 Factors Controlling Design

In the design of the exploding wire light source, a number of criteria had to be kept in mind.

- 1) The size and composition of the wire to be vaporized. Reference 16 indicated that tungsten wire, .001-in. diameter and approximately 1/4" long, would be suitable. This was taken as a starting point, and the rest of the unit was designed around this information.
- 2) Availability of components. Some kind of switch was required to trigger the discharge at a precise instant, and there was available an EG & G Model GP-12A Triggered Spark Gap which appeared suitable for this purpose: the unit was sufficiently rugged to withstand the massive electrical discharges involved, and was capable of precise triggering. A large capacitor was also required, and, in line with the suggestion of Ref. 16, there was available a BICC\* 8.5µf, 20 kv Energy Storage Capacitor, capable of storing up to 1600 joules. Thus the physical dimensions and characteristics of these two items had to be kept in mind during design.
- 3) Installation requirements. In order to provide reasonable interchangeability between the exploding wire source and the magnesium spark source, as much as possible of the equipment associated with the existing light source installation had to be used. This meant using the existing light source mounting, which put rather severe limitations on the physical layout of the components, and dictated, among other things, that the capacitor had to sit on the

---

\* British Insulated Callender's Cables Limited.

floor outside the light source box, as shown in Fig. C.3, and be connected to it by a flexible cable. This requirement also demanded the use of the existing high-voltage power supply, and, as much as possible, the existing trigger spark generator used to fire the triggered spark gap.

4) High voltage insulation. Given the physical dimensions and other characteristics of the components and the installation requirements, due regard had to be given to high voltage insulation. This becomes especially important when one considers the severe and extensive damage that could result to the interferometer and its valuable optics, situated close by, if a breakdown in the insulation occurred with the capacitor fully charged to 1600 joules.

5) Finally, given all the above requirements, it was desirable to keep inductance and resistance in the electrical circuit as low as possible. Low inductance was desirable in order to get a fast risetime for the energy discharge; this would help decrease the duration and increase the peak intensity of the light output. This requirement dictated, for example, the use of coaxial cable to connect the capacitor to the source. Low resistance was desirable in order to keep ohmic losses to a minimum so that as much energy as possible would go into vaporizing the wire. Even a few ohms are significant here, as peak currents are of the order of  $10^4$  amperes.

6) In addition, it was desired that use of the exploding wire source should be as convenient as possible, with low "turn-around" time between successive shots. Given the installation requirements, this demanded that the light source unit proper be easily removable in order to replace the wire.

### C.3 Development

Before proceeding with an actual design of an exploding wire source for use with the interferometer, a preliminary model was built in order to test the concept, and get some idea of the performance that might be expected. This model was quite rudimentary, designed only to deliver the charge of the capacitor through the triggered spark gap to the requisite piece of tungsten wire. Triggering techniques for the spark gap were also developed using this model, with the result that an EG & G Model TR-60 Pulse Transformer was substituted for the existing transformer in the trigger spark generator. Polarity requirements for the trigger spark were also determined.

The light output from this arrangement was monitored, as was the magnesium spark, by an EG&G Model SD-100 Photodiode, which had rise and fall times of the order of five and fifteen nanoseconds respectively, so that the intensity profile was faithfully reproduced without complications caused by the sensor. Intensity measurements with this arrangement indicated that an improvement in peak intensity of at least 3 - 4 times over that of the magnesium spark could be expected. Thus, it was considered that, along with other improvements which could be made in the system as a whole, an exploding wire source plus a Kerr Cell Shutter would be a practical way of obtaining the required time resolution.

Design was then put in hand for a final model to be used with the interferometer, and drawings and photographs are shown in Figs. C.3 - C.6. The basic unit, as shown in Fig. C.4, is built of Plexiglas and is almost totally enclosed for high voltage insulation. This unit sits in a Plexiglas cradle, visible in Fig. 3, which is bolted to the light source box in place of the

original magnesium spark unit, so that the two light sources are interchangeable. As mentioned before, the capacitor had to be placed outside the light source on the floor and connected to it by cable. For this purpose, a short length of RG-17A/U coaxial cable, rated at 11,000 volts at radio frequencies (higher at lower frequencies), was obtained; this cable was reasonably flexible, yet had sufficiently big conductors that resistive losses were minimized. The termination of the cable at the capacitor was built of brass, and its design was dictated by the form of the connections on top of the capacitor. At the other end, in order that the light source unit should be quickly removable, the use of some kind of screw-on connector was considered desirable; however, a connector big enough to withstand the currents involved, and with sufficient stand-off distance to hold off 20,000 volts was not readily available. Eventually, a large Type LC radio-frequency connector was obtained (Plug: UG-154/U; Jack: UG-352/U) rated at only 5000 volts, but sufficiently robust otherwise for this application. A new teflon insert was then made for the jack, and the assembly of the plug was modified slightly, in order to increase the stand-off distance. Details are shown in Fig. C.6.

The electrical circuit is shown in Fig. C.7. It is noted that the high-voltage connection from the power supply is made to the top electrode of the spark gap, that a twenty megohm, forty watt resistor is installed in the charging line (to protect the power supply from the discharge), and that the light source is grounded on the ground side of the capacitor rather than between the spark gap and the tungsten wire. This last was to ensure that all the energy stored in the capacitor went through the tungsten wire and also so that the discharge would not momentarily raise the ground point above true ground potential, affecting all of the instrumentation connected to it. This effect will always occur to a certain extent, but the resistance between the ground point and the capacitor is less in this configuration than if the ground connection had been between spark gap and tungsten wire. The advantage of the latter configuration would be that the energy of the trigger spark would not pass through the wire to be exploded; as it stands, the trigger spark energy does pass through the wire, and this sets a lower limit to the diameter of the wire: if the wire is too fine, the energy of the trigger spark will vaporize it before the main discharge begins.

The control and monitoring circuitry is also shown in Fig. C.7, and photographs of the entire installation and the Kerr Cell installation are shown in Fig. C.8. The entire arrangement is triggered by a +150 volt signal from a pulse generator which is, in turn, fired by a shock detector located in the wall of the shock tube a few feet upstream of the test section. This primary 150 volt trigger is used to fire the first delay generator, a Racal digital delay generator, with the delay set to prevent any further operation until the shock wave or other phenomenon is in a position to be photographed. The first delay generator then puts out a +20 volt signal which fires another pulse generator, which puts out a secondary +150 volt trigger signal. This secondary trigger is then attenuated and used to fire the trigger spark generator which provides the pulse for initiation of the main discharge. The secondary trigger is also used to fire a second delay generator, an Electro-Optical Instruments Model TG-100 Delay Generator, which has a continuously variable time delay extending down to about 100 nanoseconds. This second delay generator is used to delay the trigger pulse to the Kerr Cell until the light output from the exploding wire has reached peak intensity, approximately two micro-seconds after initiation of the discharge. The output from the first delay generator is also used to trigger an oscilloscope which records the signal from an

SD-100 photodiode mounted inside the interferometer (in a position to watch the light output from the exploding wire) and also records a sample of the electrical pulse which operates the Kerr Cell (See Fig. C.11.) These two are recorded simultaneously, and thus the synchronization between the Kerr Cell and the discharge can be checked.

#### C.4 Performance

Figure C.2 shows a typical intensity profile obtained using the SD-100 photodiode. Since the traces shown in Figs. C.2 and C.1 were obtained under identical conditions, it is seen that an improvement in peak intensity of approximately six times over that of the magnesium spark was achieved, assuming that the response of the photodiode was linear with incident intensity, something which was open to doubt: a similar trial using a different SD-100 photodiode showed only 3-1/2 - 4 times improvement over the magnesium spark. In addition it was noted that the total duration of the light had increased to approximately twenty microseconds. Intensity traces were also obtained using three different interference filters as shown in Fig. C.9: it is seen that the profiles tended to vary somewhat with wavelength, something which was not unexpected. Again, the peak intensity appeared to vary, but this was most likely due to the varying response with wavelength of the photodiode, as well as being due to the varying transmission of the filters.

A spectral analysis of the light output was also attempted, but, apart from providing some indication of the combined characteristics of the light source, interferometer optics, Kerr Cell (if included), spectrograph and film, little was accomplished. Sample spectra are shown in Fig. C.10. The main thing that was noted from these was the cutoff of the Kerr Cell, at around 4400Å. It proved impossible to correlate the lines of these spectra with the lines of a tungsten spectrum with any degree of certainty. This was not too surprising as, in addition to tungsten lines, there were undoubtedly lines present from all the brass and plastic parts in the source adjacent to the exploding wire, as well as from the air. The relative intensities of the lines were also distorted, since the dispersion of the spectrograph was not constant with wavelength, and since the spectra were taken almost at the limit of sensitivity of the film, with a very wide slit setting on the spectrograph. In addition, the lines were very likely broadened and possibly shifted from their correct positions by the intense electric and magnetic fields present in the region of the wire.

One positive result of this analysis was to emphasize that, while it was now possible to use photographic film for interferometry using the exploding wire source plus the Kerr Cell, the performance was still marginal. Therefore, some experiments were carried out to find the combination of photographic plate plus developer that would produce the best results. After trying several combinations, it was judged that Ilford HPS plates developed for 20-30 minutes in May and Baker "Promicrol" developer produced the best results\*: as good contrast as possible, combined with low fog level and reasonably fine grain. Even then, a considerable reduction in the size of the image was necessary in order to produce useable interferograms. However, the reduction in size (from approximately 4" x 3-1/4" to 1-3/4" x 1-1/2") did not prove too serious in terms of the accuracy with which measurements of fringe shift could be made on the plates. However, even with the reduction in size,

---

\* Latest trials have indicated that Kodak 2475 emulsion, donated by Eastman Kodak, Rochester, may offer significant improvement.

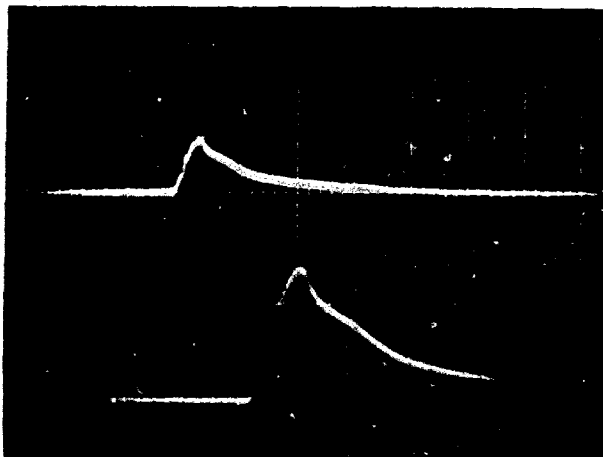
this was a great improvement over the magnesium spark plus Kerr Cell combination, where it proved to be impossible to record on film under any circumstances.

In general, it was found that a number of things had to be watched carefully. One of the main sources of trouble was feedback from the discharge through the trigger spark generator to the oscilloscope, and particularly to the second delay generator. This feedback was of considerable magnitude and would cause the second delay generator, and thus the Kerr Cell, to trigger prematurely. It was this feedback, plus the fact that the second delay generator required a pulse of about 100 volts to trigger consistently, that forced the use of the control system shown in Fig. C.7, where the output of the first delay generator was used to fire a pulse generator which provided a secondary trigger pulse. This secondary trigger had to be attenuated before being used to fire the trigger spark generator, but the same attenuator also cut down any feedback coming from the discharge to the point where it would not affect the remaining instrumentation. Originally, it had been hoped to fire the second delay generator from the discharge itself, an arrangement which would have nullified any jitter in the triggering of the main discharge. As it stands, in the configuration shown in Fig. C.7, there is a small amount of jitter, about 0.3 microseconds, in the triggering of the discharge. However, as seen in Figs. C.2 and C.9, the peak of the intensity curve is broad enough that this amount of jitter can be tolerated. In addition, the synchronization between the Kerr Cell and discharge was monitored with every shot, so that minor drifts in the triggering levels of the various components could be spotted and compensated for.

Figure C.11 shows a typical oscilloscope trace taken to check synchronization. The discharge is monitored (as mentioned earlier) by a photodiode placed inside the interferometer and considerably closer to the source than was the case in Figs. C.2 and C.9. Hence, the electrical pickup from the discharge is much worse. The traces shown in Figs. C.2 and C.9 were taken with the photodiode placed in the position normally occupied by the camera, something which is, of course, not possible when taking interferograms. The upper trace, as shown in Fig. C.11, records a sample of the 35,000 volts pulse which operates the Kerr Cell. This pulse too is much distorted by pickup.

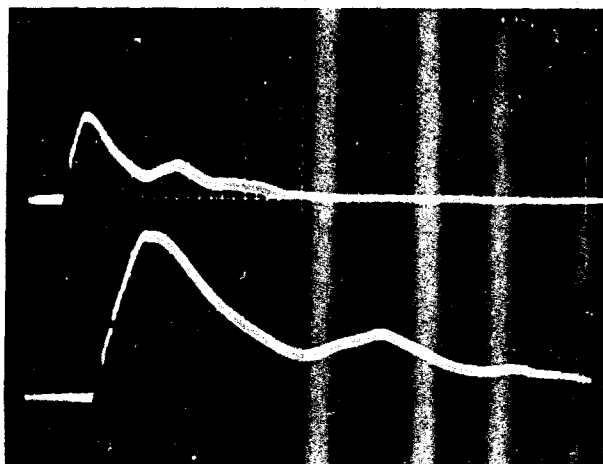
#### C.5 Conclusion

In conclusion, it may be said that the exploding wire light source has been developed into a very useful and reliable piece of equipment. Used in conjunction with a Kerr Cell, the exploding wire source has been the means of substantially improving the time resolution of the interferograms taken with the UTIAS 9" Mach-Zehnder interferometer. Sample interferograms taken with the exploding wire source are shown in Figs. 2 and 3b, and the improved time resolution is apparent when Figs. 2 and 3b are compared with Figs. 1 and 3a.



Upper: 5 volts/div.  
 1  $\mu$ sec./div.  
 Lower: 2 volts/div.  
 0.5 usec./div.

FIG. C1 - INTENSITY PROFILE OF LIGHT FROM MAGNESIUM SPARK  
 LIGHT SOURCE - TAKEN WITH EG&G SD-100 PHOTODIODE



Upper: 20 volts/div.  
 5 usec./div.  
 Lower: 10 volts/div.  
 2 usec./div.

FIG. C2 - INTENSITY PROFILE OF LIGHT FROM EXPLODING WIRE  
 LIGHT SOURCE - TAKEN WITH EG&G SD-100 PHOTODIODE

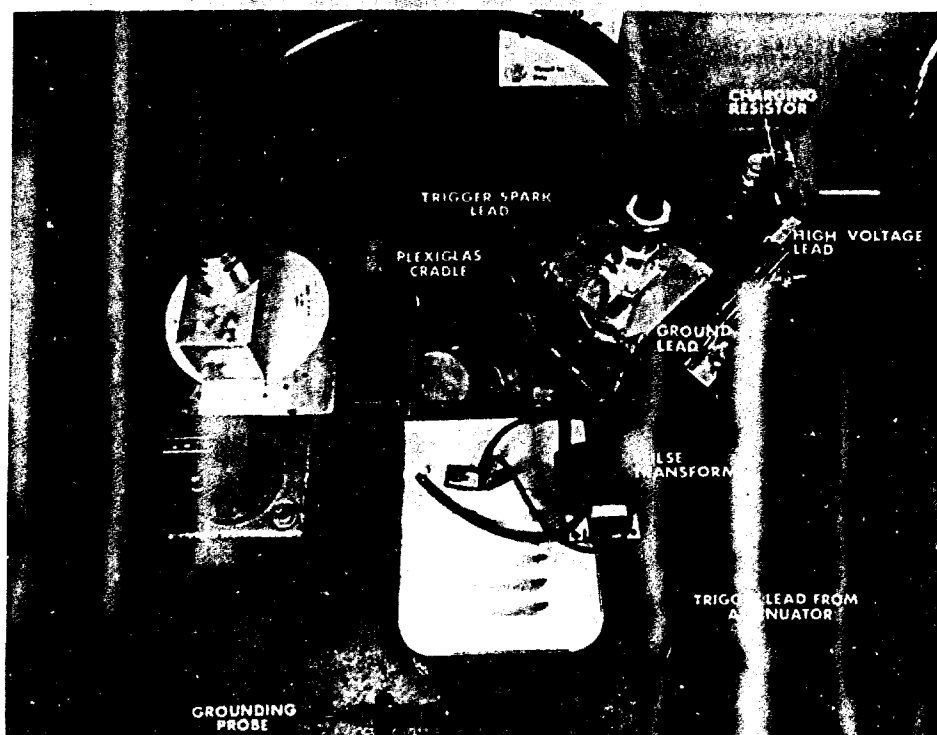
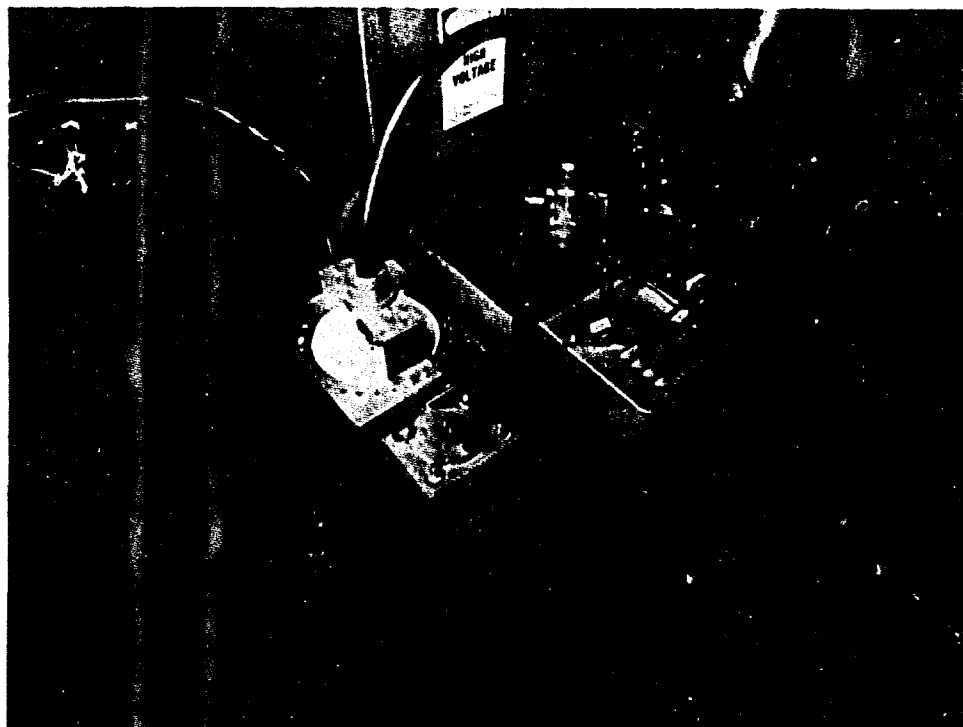


FIG. C3 - VIEWS OF EXPLODING WIRE LIGHT SOURCE INSTALLED IN INTERFEROMETER

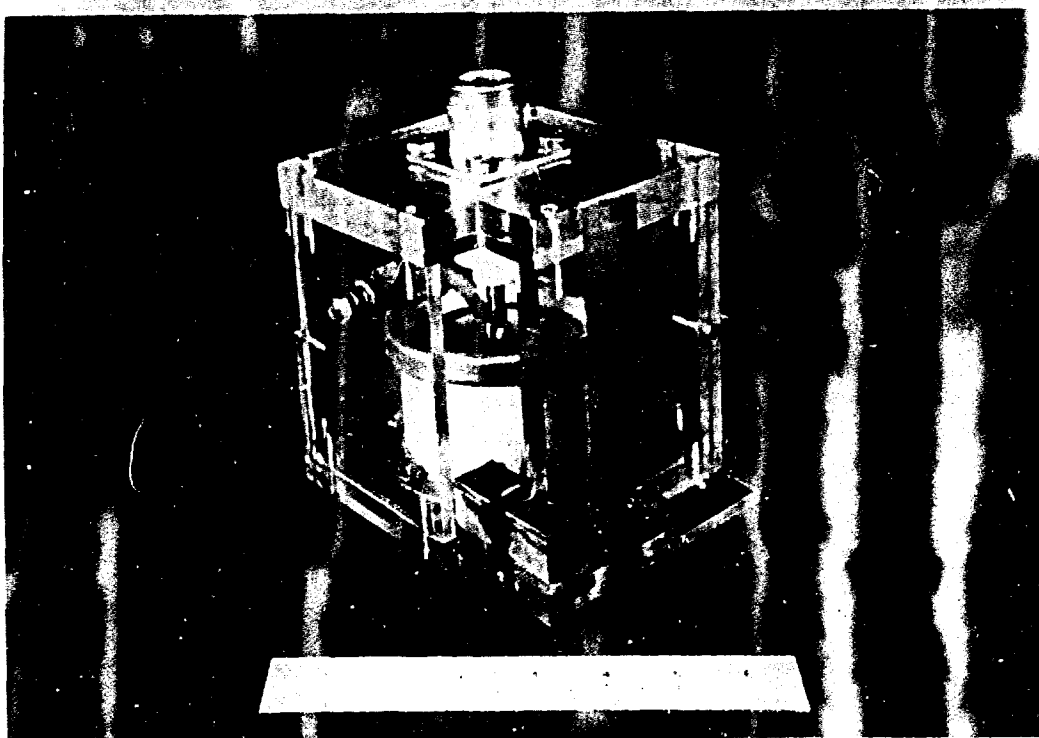
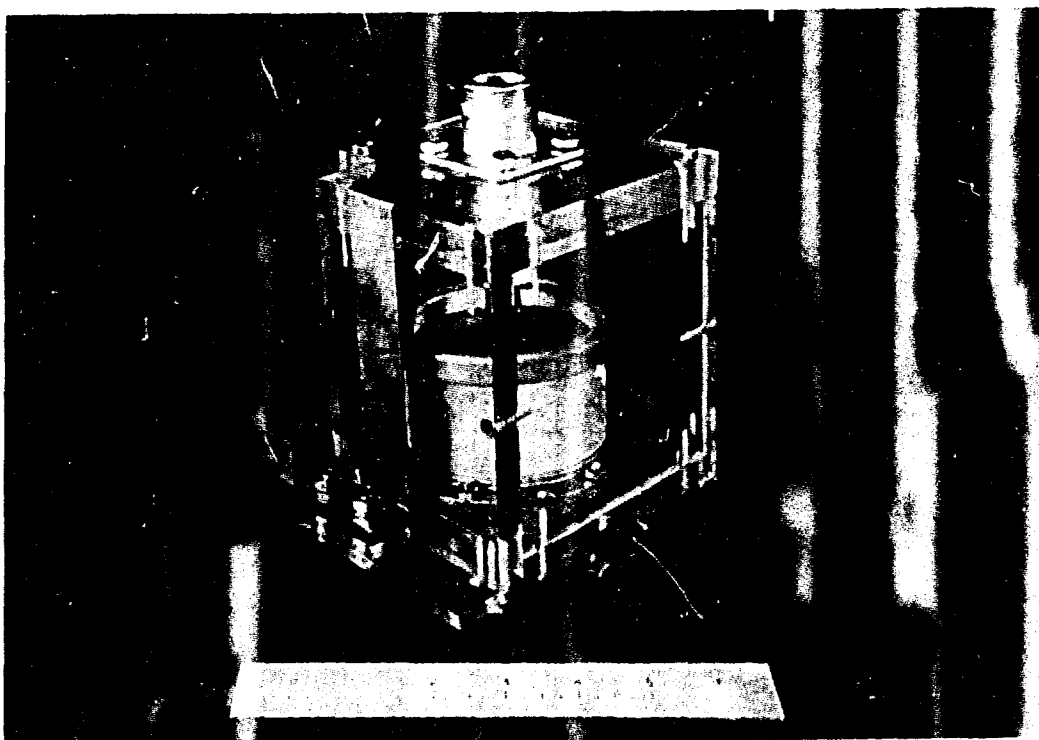


FIG. C4 - CLOSE-UP VIEWS OF LIGHT SOURCE UNIT

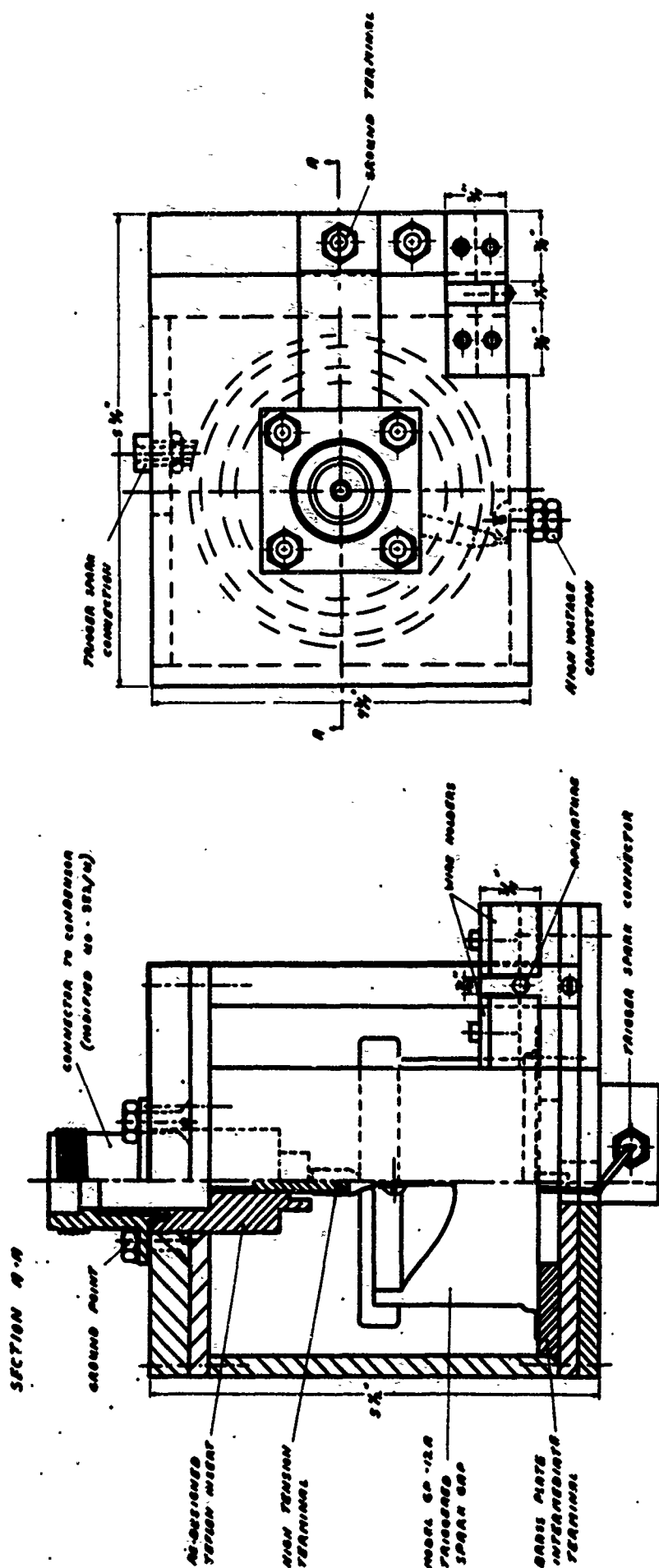
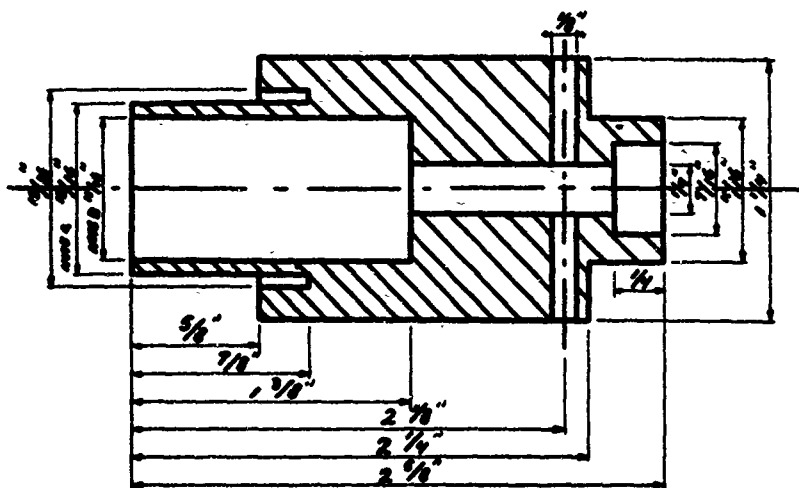


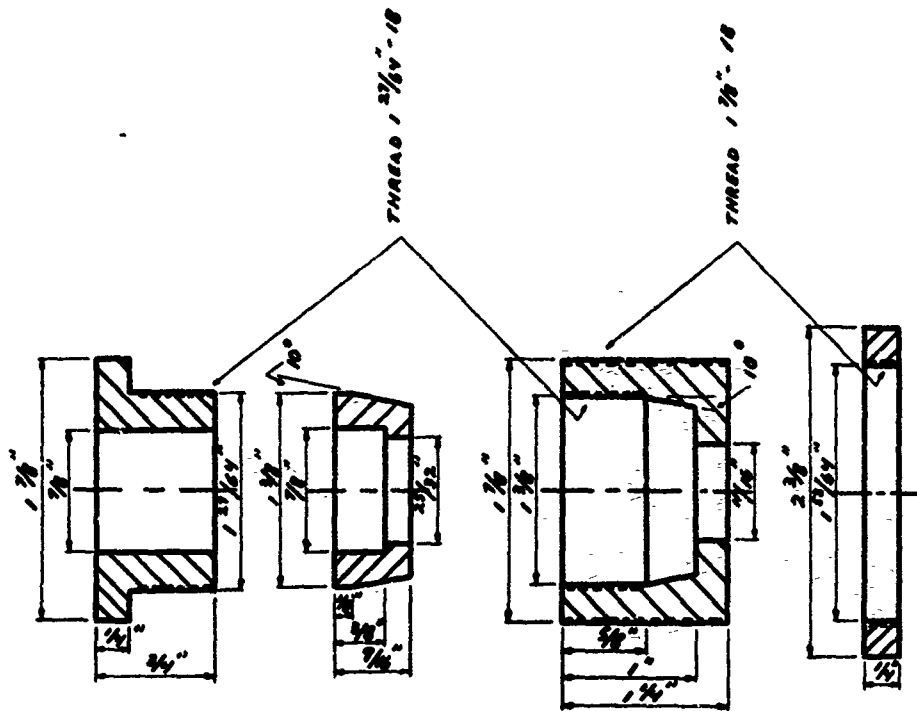
FIG. C3 - CONSTRUCTION DETAILS OF EXPLODING WIRE LIGHT SOURCE UNIT



NOTE: TO BE DRIVEN FIT IN SHELL OF RECEPTACLE  
 NOTES: +0.000", -0.005"

NEW INSERT FOR CONNECTOR FOR LIGHT SOURCE  
 MATERIAL: TEFLON

FIG. C6a - DETAIL OF REDESIGNED INSERT  
 FOR CABLE JACK (UG-352/U)



TERMINATION FOR RG-17A/U CABLE  
 MATERIAL: BRASS.

FIG. C6b - DETAIL OF TERMINATION FOR  
 RG-17A/U CABLE

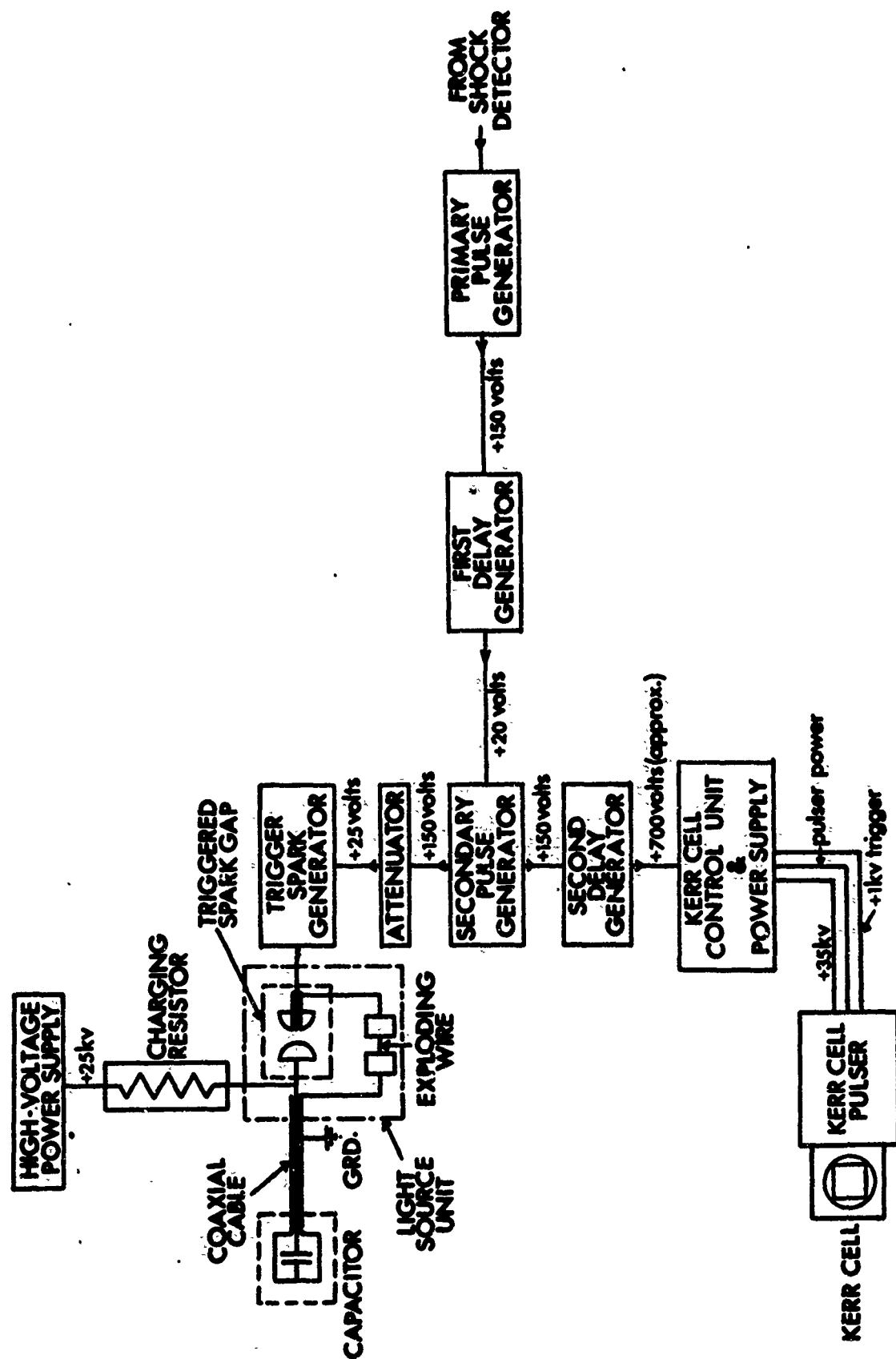


FIG. C7 - ELECTRICAL CIRCUITRY FOR EXPLODING WIRE LIGHT SOURCE AND KERR CELL

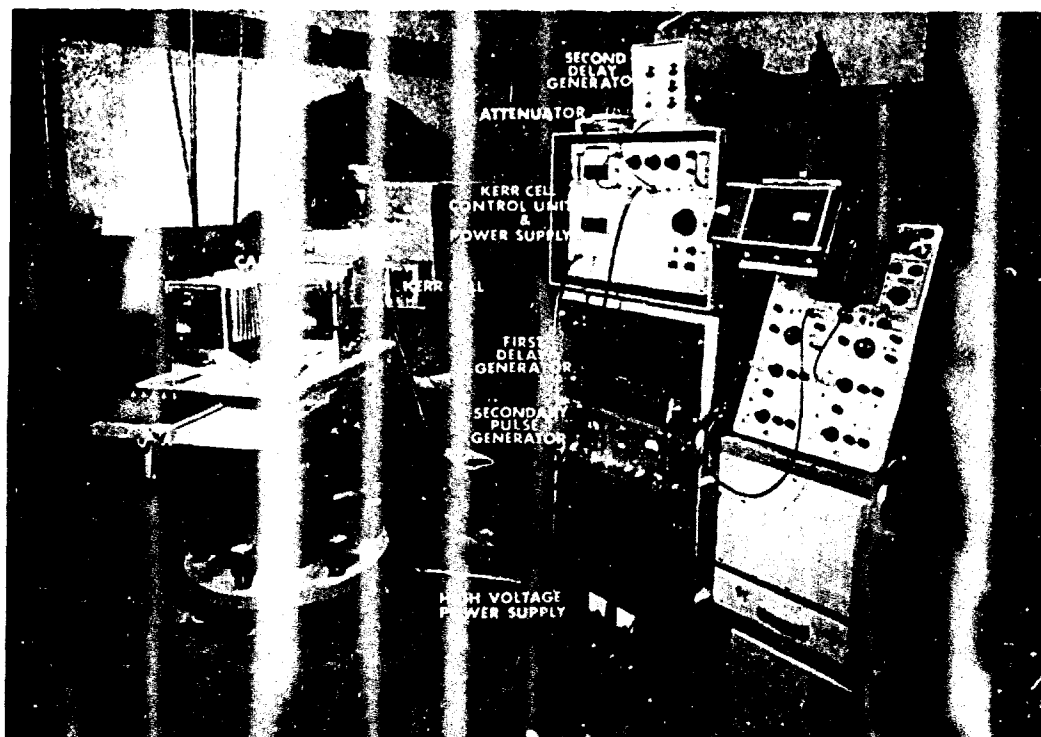


FIG. C8a - CONTROL AND MONITORING INSTRUMENTATION FOR LIGHT SOURCE AND KERR CELL

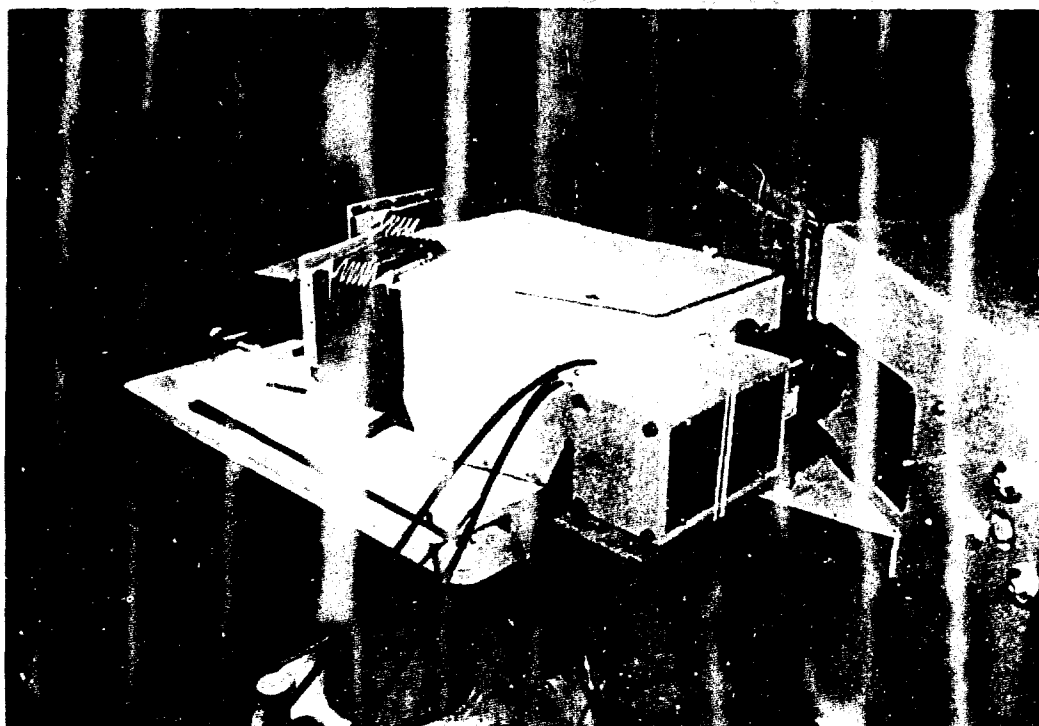
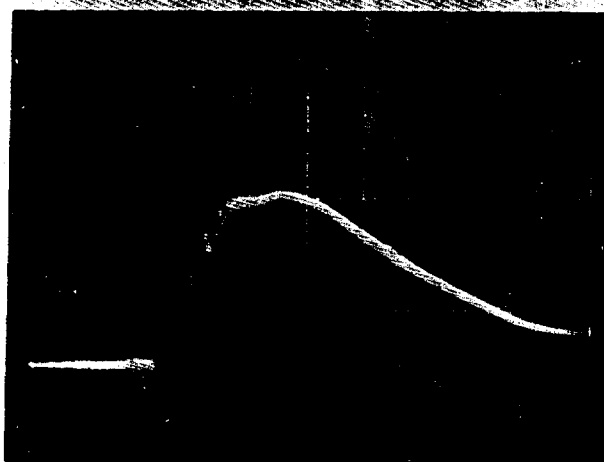


FIG. C8b - CLOSE-UP OF KERR CELL INSTALLATION



a) 4680Å Hor: 1  $\mu$ sec./div.  
Ver: 100 mv/div.

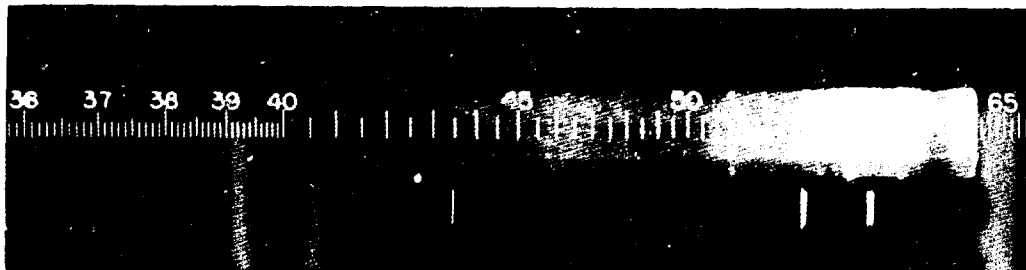


b) 5210Å Hor: 1  $\mu$ sec./div.  
Ver: 100 mv/div.

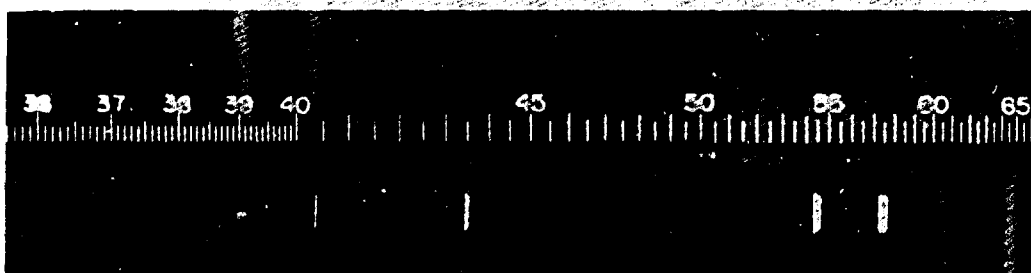


c) 5675Å Hor: 1  $\mu$ sec./div.  
Ver: 500 mv/div.

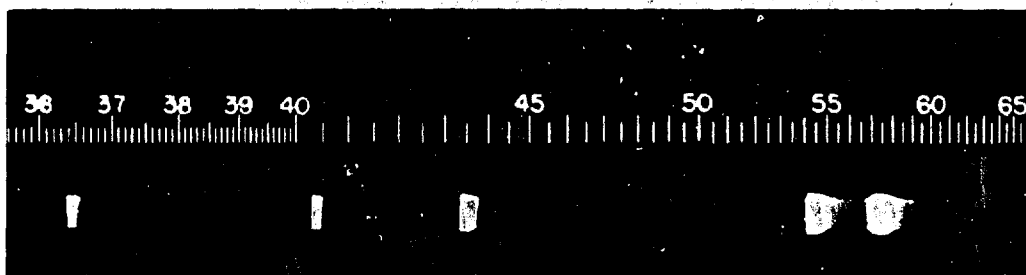
FIG. C9 - MONOCHROMATIC INTENSITY PROFILES OF LIGHT FROM  
EXPLODING WIRE SOURCE, TAKEN AT VARIOUS WAVELENGTHS  
(Differences in output reflect variations in spectral sensitivity of  
the photodiode and in the transmission of the interference filters)



a) Spectrogram of light from exploding wire source viewed directly, with Kerr Cell removed. Variations in intensity in the spectrum reflect variations in spectral sensitivity of the film as well as variations in the spectral content of the light.

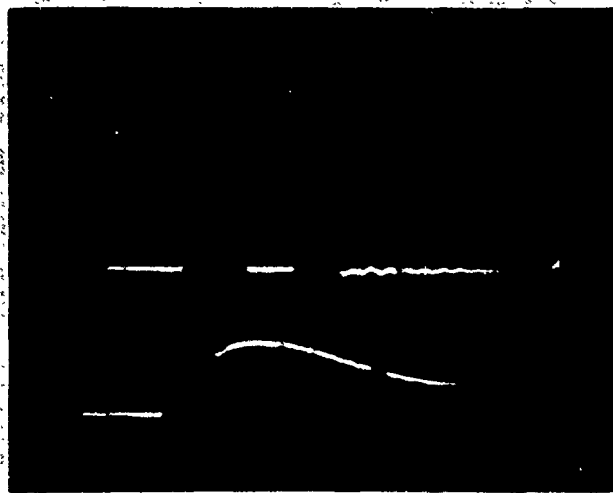


b) Spectrogram of light from exploding wire source viewed through the Kerr Cell with the Kerr Cell cocked open, showing the cutoff due to the Nitrobenzene of the Kerr Cell.



c) Spectrogram of light from exploding wire source viewed through Kerr Cell, with Kerr Cell operating, i.e., open for 200 nanoseconds only.

FIG. C10 - SPECTROGRAMS OF LIGHT FROM EXPLODING WIRE SOURCE UNDER VARIOUS CONDITIONS  
(Taken with a Hilger Medium Quartz Spectrograph using Ilford HPS Film. Calibrating spectrum is Mercury)



Upper: 1  $\mu$ sec./div.  
10 volts/div.  
Lower: 1  $\mu$ sec./div.  
500 mv/div.

**FIG. C11 - TYPICAL OSCILLOSCOPE TRACE USED TO CHECK SYNCHRONIZATION BETWEEN EXPLODING WIRE AND KERR CELL**

Upper trace: Sample ( 30 volts approx. ) of 35kv pulse which operates Kerr Cell -

Lower trace: Output from photodiode placed inside interferometer housing to monitor light output from exploding wire source

**Security Classification**

DOCUMENT CONTROL DATA - R&D		
<small>(Security classification of title, body of abstract and indexing annotation must be entered when the overall report is classified)</small>		
1. ORIGINATING ACTIVITY (Corporate author) Institute for Aerospace Studies University of Toronto, Toronto 5, Ontario		2a. REPORT SECURITY CLASSIFICATION Unclassified
		2b. GROUP
3. REPORT TITLE  An Experimental Determination of the Gladstone-Dale Constants for Dissociating Oxygen.		
4. DESCRIPTIVE NOTES (Type of report and inclusive dates) Scientific Interim		
5. AUTHOR(S) (Last name, first name, initial)  Anderson, J.H.B.		
6. REPORT DATE March, 1967	7a. TOTAL NO. OF PAGES 67	7b. NO. OF REFS 16
8a. CONTRACT OR GRANT NO. AF-AFOSR-365-66	9a. ORIGINATOR'S REPORT NUMBER(S) UTIAS Technical Note No. 105	
A. PROJECT NO. 9783-01		
C. 61445014	9b. OTHER REPORT NO(S) (Any other numbers that may be assigned this report) AFOSR 67-0336	
D. 681307		
10. AVAILABILITY/LIMITATION NOTICES  1. Distribution of this document is unlimited.		
11. SUPPLEMENTARY NOTES  TECH, OTHER	12. SPONSORING MILITARY ACTIVITY (SREM) Air Force Office of Scientific Research 1400 Wilson Boulevard Arlington, Virginia 22209	
13. ABSTRACT An experimental determination of the Gladstone-Dale Constants for dissociating oxygen has been carried out. The result obtained for the specific refractivity of the oxygen molecule was in good agreement with available room-temperature data, indicating that the Gladstone-Dale constants do not appear to change with temperature. The result obtained for the specific refractivity of the oxygen atom was in agreement with the work of Alpher and White (Ref.7) but the present work was considered to be more reliable in view of a much lower experimental error and the removal of the assumption of a value for the Gladstone-Dale constant for the oxygen molecule. A theoretical analysis was also carried out in which expressions for the index of refraction of dissociating and ionizing gases were derived. These results were used in an analysis of the formation of monochromatic and white-light interference patterns in a Mach-Zehnder interferometer. An appendix is included giving a brief summary of as yet uncompleted experimental work to determine the Gladstone-Dale constants for ionizing argon. Another appendix gives details of an exploding wire light source, which was developed to allow the use of a Kerr cell unit to improve the time resolution of the interferograms.		

DD FORM 1 JAN 64 1473

Security Classification

Unclassified

Security Classification

14 KEY WORDS	LINK A		LINK B		LINK C	
	ROLE	WT	ROLE	WT	ROLE	WT
1. Gladstone-Dale constants at high temperature 2. Dissociated and Ionized Gas Flows 3. Shock Waves 4. Shock Tube Flows 5. Interferometry						

#### INSTRUCTIONS

1. **ORIGINATING ACTIVITY:** Enter the name and address of the contractor, subcontractor, grantee, Department of Defense activity or other organization (*corporate author*) issuing the report.

2a. **REPORT SECURITY CLASSIFICATION:** Enter the overall security classification of the report. Indicate whether "Restricted Data" is included. Marking is to be in accordance with appropriate security regulations.

2b. **GROUP:** Automatic downgrading is specified in DoD Directive 5200.10 and Armed Forces Industrial Manual. Enter the group number. Also, when applicable, show that optional markings have been used for Group 3 and Group 4 as authorized.

3. **REPORT TITLE:** Enter the complete report title in all capital letters. Titles in all cases should be unclassified. If a meaningful title cannot be selected without classification, show title classification in all capitals in parenthesis immediately following the title.

4. **DESCRIPTIVE NOTES:** If appropriate, enter the type of report, e.g., interim, progress, summary, annual, or final. Give the inclusive dates when a specific reporting period is covered.

5. **AUTHOR(S):** Enter the name(s) of author(s) as shown on or in the report. Enter last name, first name, middle initial. If military, show rank and branch of service. The name of the principal author is an absolute minimum requirement.

6. **REPORT DATE:** Enter the date of the report as day, month, year; or month, year. If more than one date appears on the report, use date of publication.

7a. **TOTAL NUMBER OF PAGES:** The total page count should follow normal pagination procedures, i.e., enter the number of pages containing information.

7b. **NUMBER OF REFERENCES:** Enter the total number of references cited in the report.

8a. **CONTRACT OR GRANT NUMBER:** If appropriate, enter the applicable number of the contract or grant under which the report was written.

8b, 8c, & 8d. **PROJECT NUMBER:** Enter the appropriate military department identification, such as project number, subproject number, system numbers, task number, etc.

9a. **ORIGINATOR'S REPORT NUMBER(S):** Enter the official report number by which the document will be identified and controlled by the originating activity. This number must be unique to this report.

9b. **OTHER REPORT NUMBER(S):** If the report has been assigned any other report numbers (*either by the originator or by the sponsor*), also enter this number(s).

10. **AVAILABILITY/LIMITATION NOTICES:** Enter any limitations on further dissemination of the report, other than those

imposed by security classification, using standard statements such as:

- (1) "Qualified requesters may obtain copies of this report from DDC."
- (2) "Foreign announcement and dissemination of this report by DDC is not authorized."
- (3) "U. S. Government agencies may obtain copies of this report directly from DDC. Other qualified DDC users shall request through \_\_\_\_\_."
- (4) "U. S. military agencies may obtain copies of this report directly from DDC. Other qualified users shall request through \_\_\_\_\_."
- (5) "All distribution of this report is controlled. Qualified DDC users shall request through \_\_\_\_\_."

If the report has been furnished to the Office of Technical Services, Department of Commerce, for sale to the public, indicate this fact and enter the price, if known.

11. **SUPPLEMENTARY NOTES:** Use for additional explanatory notes.

12. **SPONSORING MILITARY ACTIVITY:** Enter the name of the departmental project office or laboratory sponsoring (*paying for*) the research and development. Include address.

13. **ABSTRACT:** Enter an abstract giving a brief and factual summary of the document indicative of the report, even though it may also appear elsewhere in the body of the technical report. If additional space is required, a continuation sheet shall be attached.

It is highly desirable that the abstract of classified reports be unclassified. Each paragraph of the abstract shall end with an indication of the military security classification of the information in the paragraph, represented as (TS), (S), (C), or (U).

There is no limitation on the length of the abstract. However, the suggested length is from 150 to 225 words.

14. **KEY WORDS:** Key words are technically meaningful terms or short phrases that characterize a report and may be used as index entries for cataloging the report. Key words must be selected so that no security classification is required. Identifiers, such as equipment model designation, trade name, military project code name, geographic location, may be used as key words but will be followed by an indication of technical context. The assignment of links, rules, and weights is optional.

Security Classification